

The Impact of Solar – Terrestrial Plasma and Magnetic Field on the Detection of Space-borne Gravitational Wave Detections

Wei Su^{1,2*}

^{1*}School of Physics and Astronomy, MOE Key Laboratory of TianQin Mission, TianQin Research Center for Gravitational Physics, Frontiers Science Center for TianQin, Gravitational Wave Research Center of CNSA, Sun Yat-sen University (Zhuhai Campus), Zhuhai, 519082, Guangdong, China .

Corresponding author(s). E-mail(s): suwei25@mail.sysu.edu.cn;

Abstract

Space-borne gravitational wave detections raise new questions for heliophysics: how the Sun-Terrestrial space environment affect gravitational wave detection, and to what extent? Space-borne gravitational wave detectors use laser interferometry to measure displacement variations between two free test masses caused by gravitational waves. Space-borne gravitational wave detectors require extremely high measurement accuracy, making it necessary to take into account the effects of space plasma and magnetic field. On one hand, laser propagation through space plasma can induce optical path difference noise, affecting distance measurement accuracy. On the other hand, interactions between space magnetic field and the test masses can generate acceleration noise. This review introduces studies on laser propagation noise and space magnetic acceleration noise in space gravitational wave detection. And this review presents a method, time-delay interferometry, to suppress laser propagation noise.

Keywords: Space Plasma, Space magnetic field, Gravitational Wave Detections

1 Introduction

In early 2016, the discovery of gravitational waves (GWs) was officially announced by the LIGO collaboration [1], and since then, modern astronomy has entered the multi-messenger era. According to the GW signature we can get some parameters that are

difficult to obtain from electromagnetic (EM) wave observation, such as the mass and spin of black holes and neutron stars. Until the beginning of 2025, more than 100 GW events and candidate events have been detected [2–6], all of which were discovered by ground-borne GW detectors in the frequency band of about 10–1000 Hz. In order to expand the frequency band of GW detection, it is proposed to expand the laser interferometer for GW detection from the ground to the space, so that the interferometric arm can be $\sim 10^5$ to $\sim 10^6$ kilometers, and the corresponding sensitivity frequency expands to the low-frequency band from 10^{-4} Hz to 1 Hz. At present, the proposed space GW detection plans are Laser Interferometer Space Antenna (LISA) led by European Space Agency (ESA) [7], DECIGO of Japan [8], Taiji (TJ) [9] and TianQin (TQ) [10] of China, etc.

Deploying GW detectors in space can avoid the effects of ground vibrations, the Earth gravity gradient force, atmosphere and human activities. However, space is not a vacuum, for space-borne GW detection, it is necessary to fully consider the effects of the space environment, such as space magnetic field, plasma, high-energy particles, which will directly affect the success or failure of space-borne GW detection. Now the space-borne GW detection route is to use the laser interferometry to measure the displacement change of the free test mass (TM) caused by GW, and its core measurement indices are: 1. displacement ranging accuracy, the laser interferometry ranging accuracy of the space-borne GW detection is required to be of the order of 10^{-12} m Hz $^{-1/2}$ [11–13]; 2. acceleration noise, which is a parameter to evaluate whether the TM is ‘free’ or not, and the accuracy of acceleration measurements for space-borne GW detection is required to be of the order of 10^{-15} m s 2 Hz $^{-1/2}$ [11–13]. This review focuses on these two core indices to analyse the laser ranging noise and acceleration noise caused by the space plasma and magnetic field.

From the perspective of GW detection, firstly, space plasma can lead to laser propagation effect [14–17]. There are dispersion and Faraday rotation effects when the laser propagates in space plasma, which will lead to time delay, optical path difference (OPD), wavefront distortion polarization angle change, and so on, affecting the laser ranging accuracy. Secondly, the space magnetic field will lead to acceleration noise [18–20]. Since the TM in the inertial sensor of GW detector has weak remanent magnet moment and residual charge, the interaction of remanent magnet moment and residual charge with the space magnetic field can generate magnetic moment force and Lorentz force, resulting in acceleration noise [20, 21].

From the perspective of the space environment, solar-terrestrial physical processes on various time and space scales affect the detection of GW in space, the schematic is show in Figure 1. On the time scale, the sensitive frequency band for space-borne GW detection is from 0.1 mHz to 1 Hz, which corresponds to a time resolution of up to 1 s. On the other hand, The Sun is the source of the space plasma and magnetic field, and the solar activity has a periodicity of about 11 years [22]. Therefore, the time scale to be considered for the space-borne GW detection is from the order of 1 s to 10^8 s (11 years $\approx 3 \times 10^8$ s), covering 8 orders of magnitude. On the space scale, the arm length of the GW detectors reach the order of $\sim 10^5$ to $\sim 10^6$ km, and the velocity of GW detectors will travel about 2 km (TQ) or about 30 km (LISA and TJ) in 1 s. Thus, the smallest space scale we need to consider reaches the order of ~ 1 km. From ~ 1 to $\sim 10^6$ km

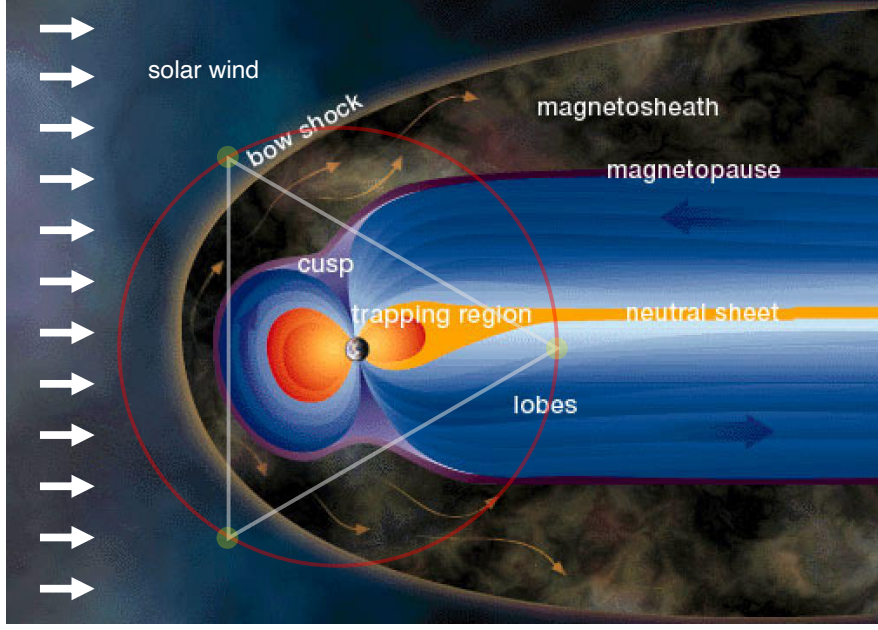


Fig. 1 The schematic of GW detectors in space environment [20].

spans 6 orders of magnitude in space scale. Due to the 8 orders interval in time scale and 6 orders interval in space scale, we need to consider multiple scales of heliophysics processes, e.g., plasma dynamics, magnetohydrodynamics (MHD), and global scales [23–26]. For the scale of plasma dynamics, e.g., magnetic reconnection [27–29], plasma waves [30–32], and turbulence [33, 34] need to be considered. For the MHD scale, structures such as shocks [35, 36], magnetic clouds [37, 38], and MHD instabilities [39] need to be considered. For the global scale, the evolution of the global structure of the Earth’s magnetosphere and the heliosphere [40, 41], and the corotating interaction regions (CIRs) [42–44] should to be considered. In addition, dramatic changes of space plasma and magnetic field caused by eruption phenomena of the Sun and Earth (e.g., flares [45–47], coronal mass ejections (CME) [48, 49], magnetic storms [50–52], etc.) should to be considered. All these heliophysics processes will have impacts on GW detection and need to be evaluated.

This review presents the theory of space environment effects on space-borne GW detection, along with the heliophysics methods, models, and data used in the research, which are detailed in Section 2. Section 3 is the results of laser propagation noise (LPN) in space plasma on GW detections, and the methods and results of suppressing LPN. Section 4 gives the results of the effect of acceleration noise due to space magnetic fields on GW detection. Finally, there are discussion and conclusion.

2 Theories, models, and data of space plasma and magnetic field effects on GW detection

2.1 EM waves propagation in the space plasma

The propagation of EM waves in plasma can be described by the Appleton–Hartree (A–H) Equation. By employing dynamic equations of plasma and Maxwell’s Equations, the propagation characteristics of EM waves in magnetized plasma are derived, culminating in the expression for the refractive index, the A–H Equation [53, 54].

Here, the coordinate is taken as follows: The magnetic field \mathbf{B}_0 is aligned with the z -axis, the wavevector \mathbf{k} forms an angle θ with the magnetic field, and the x -axis is perpendicular to both \mathbf{B}_0 and \mathbf{k} .

The motion equation of an electron in the collision plasma is as follow,

$$m \frac{d\mathbf{u}}{dt} = -e(\mathbf{E} + \mathbf{u} \times \mathbf{B}_0) - m\nu\mathbf{u} \quad (1)$$

where, m is electron mass, e is electron charge, \mathbf{u} is the velocity of the electron, \mathbf{E} is the electric field, \mathbf{B}_0 is the background magnetic field, ν is the collision frequency.

For a harmonic monochromatic EM wave with angular frequency ω , the electric field \mathbf{E} can be written as,

$$\mathbf{E}(\mathbf{r}, t) = \mathbf{E}_0 e^{i(\mathbf{k} \cdot \mathbf{r} - \omega t)} \quad (2)$$

Thus, for harmonic wave, there are,

$$\frac{\partial}{\partial t} = -i\omega, \quad \frac{\partial^2}{\partial t^2} = -\omega^2, \quad \nabla = i\mathbf{k} \quad (3)$$

Substitute Equation (3) into Equation (1), the motion equation becomes,

$$\left(1 + i\frac{\nu}{\omega}\right) \mathbf{u} + \frac{ie}{\omega m} (\mathbf{u} \times \mathbf{B}_0) = \frac{i}{\omega m} e\mathbf{E} \quad (4)$$

Since the magnetic field is along z -axis, in the Lorentz force term ($\mathbf{u} \times \mathbf{B}_0$) of motion Equation (1),

$$\mathbf{u} \times \mathbf{B}_0 = B_0 u_y \mathbf{e}_x - B_0 u_x \mathbf{e}_y$$

where, \mathbf{e}_x and \mathbf{e}_y are the unit vector in x - and y -axes, respectively. Labelling the electron cyclotron frequency $\omega_B = eB_0/m$, and the plasma oscillation frequency $\omega_p^2 = \frac{e^2 n_e}{m\varepsilon}$, where n_e is the electron number density, and ε is the electric permittivity. And introducing the notation,

$$\begin{aligned} X &= \frac{\omega_p^2}{\omega^2}, & Y &= \frac{\omega_B}{\omega}, & Z &= \frac{\nu}{\omega} \\ U &= 1 + iZ \end{aligned} \quad (5)$$

With the denotation of Equation (5), the motion Equation (1) can be written in following form,

$$\begin{pmatrix} U & iY & 0 \\ -iY & U & 0 \\ 0 & 0 & U \end{pmatrix} \begin{pmatrix} u_x \\ u_y \\ u_z \end{pmatrix} = -\frac{ie}{m\omega} \begin{pmatrix} E_x \\ E_y \\ E_z \end{pmatrix} \quad (6)$$

Inverting the matrix in the above Equation (6), then the velocity \mathbf{u} can be expressed by electric field \mathbf{E} in the following form,

$$\begin{pmatrix} u_x \\ u_y \\ u_z \end{pmatrix} = -\frac{ie}{m\omega U (U^2 - Y^2)} \begin{pmatrix} U^2 & -iUY & 0 \\ iUY & U^2 & 0 \\ 0 & 0 & (U^2 - Y^2) \end{pmatrix} \begin{pmatrix} E_x \\ E_y \\ E_z \end{pmatrix} \quad (7)$$

The Maxwell Equations in general form is as follow,

$$\begin{aligned} \nabla \times \mathbf{E} &= -\frac{\partial \mathbf{B}}{\partial t} \\ \nabla \times \mathbf{B} &= \mu \mathbf{j} + \mu \varepsilon \frac{\partial \mathbf{E}}{\partial t} \end{aligned} \quad (8)$$

here, μ is magnetic permeability. According to Maxwell Equations, we can get the electromagnetic wave equation as follow,

$$\nabla \times (\nabla \times \mathbf{E}) + \omega^2 \mu \varepsilon \mathbf{E} + i\omega \mu \mathbf{j} = 0 \quad (9)$$

There is Ohm's law,

$$\mathbf{j} = \sigma \mathbf{E} \quad (10)$$

where, \mathbf{j} is current density, σ is conductivity tensor.

In coordinate system that we have chosen in the beginning of Section 2.1, $\mathbf{k} = \sin \theta k \mathbf{e}_y + \cos \theta k \mathbf{e}_z$. And considering that $\nabla \times (\nabla \times \mathbf{E}) = \nabla(\nabla \cdot \mathbf{E}) - \nabla^2 \mathbf{E}$, and $\nabla = i\mathbf{k}$ (Equation (3)), and combining Ohm's law (Equation (10)), the wave Equation (9) can be written as follow,

$$(k^2 k_{ij} + \omega^2 \varepsilon \mu \epsilon_{ij}) \mathbf{E} = 0 \quad (11)$$

where, k is as follow,

$$k = \omega \sqrt{\varepsilon \mu} = \omega \frac{N}{c} \quad (12)$$

here, c is the light speed, N is the phase refraction index. And k_{ij} in Equation (11),

$$k_{ij} = \begin{pmatrix} -1 & 0 & 0 \\ 0 & \sin^2 \theta - 1 & \sin \theta \cos \theta \\ 0 & \sin \theta \cos \theta & \cos^2 \theta - 1 \end{pmatrix} \quad (13)$$

and ϵ_{ij} is dielectric tensor,

$$\epsilon_{ij} = \mathbf{I} + \frac{i}{\omega \varepsilon} \sigma \quad (14)$$

In order to ensure that Equation (11) is 0 in general, there is,

$$\omega^2 \varepsilon \mu (k_{ij} + \epsilon_{ij}) = 0 \quad (15)$$

At this stage, the relation between k and ω , i.e., the dispersion relation, is obtained.

The current density \mathbf{j} is caused by the movement of charged particles, and it is defined as,

$$\mathbf{j} = -n_e e \mathbf{u} \quad (16)$$

where, n_e is the number density of electron. Take the definition of current density \mathbf{j} into motion Equation (7)

$$\mathbf{j} = \frac{i n_e e^2}{m \omega U (U^2 - Y^2)} \begin{pmatrix} U^2 & -iUY & 0 \\ iUY & U^2 & 0 \\ 0 & 0 & (U^2 - Y^2) \end{pmatrix} \begin{pmatrix} E_x \\ E_y \\ E_z \end{pmatrix} \quad (17)$$

Considering Ohm's law, we can obtain the conductivity tensor σ_{ij} ,

$$\sigma_{ij} = \frac{i n_e e^2}{m \omega U (U^2 - Y^2)} \begin{pmatrix} U^2 & -iUY & 0 \\ iUY & U^2 & 0 \\ 0 & 0 & (U^2 - Y^2) \end{pmatrix} \quad (18)$$

And considering the relationship between dielectric tensor ϵ_{ij} and conductivity tensor σ_{ij} in Equation (14), ϵ_{ij} can be got as follow,

$$\epsilon_{ij} = \begin{pmatrix} 1 - \frac{XU}{U^2 - Y^2} & i \frac{XY}{U^2 - Y^2} & 0 \\ -i \frac{XY}{U^2 - Y^2} & 1 - \frac{XU}{U^2 - Y^2} & 0 \\ 0 & 0 & 1 - \frac{X}{U} \end{pmatrix} \quad (19)$$

Take the relation between N and k (Equation (12)) into dispersion relation (Equation (11)), we can obtain the following determinant,

$$\begin{vmatrix} -N^2 + 1 - \frac{XU}{U^2 - Y^2} & i \frac{XY}{U^2 - Y^2} & 0 \\ -i \frac{XY}{U^2 - Y^2} & -\cos^2 \theta N^2 + 1 - \frac{X}{U^2 - Y^2} & \sin \theta \cos \theta N^2 \\ 0 & \sin \theta \cos \theta N^2 & -\sin^2 \theta N^2 + 1 - \frac{X}{U} \end{vmatrix} = 0 \quad (20)$$

With following denotation,

$$\begin{aligned} S &= 1 - \frac{XU}{U^2 - Y^2}, & D &= -\frac{XY}{U^2 - Y^2}, & P &= 1 - \frac{X}{U} \\ R &= S + D, & L &= S - D \end{aligned} \quad (21)$$

we can expand the determinant Equation (20) as follow,

$$(S \sin^2 \theta + P \cos^2 \theta) N^4 - [RL \sin^2 \theta + SP (1 + \cos^2 \theta)] N^2 + PRL = 0 \quad (22)$$

Ultimately, we can obtain the solution of N^2 as follow [53],

$$N^2 = 1 - \frac{X}{U - \frac{1}{2(U-X)}Y^2 \sin^2 \theta \pm \sqrt{\frac{1}{4(U-X)^2}Y^4 \sin^4 \theta + Y^2 \cos^2 \theta}} \quad (23)$$

It is A-H Equation.

For collisionless plasma with $\nu = 0$, the collision term in the motion Equation (1) can be ignored. Thus Z is neglected, and $U = 1$. In this case, the A-H equation of collisionless plasma as follow [54],

$$N^2 = 1 - \frac{X(1-X)}{1 - X - \frac{1}{2}Y^2 \sin^2 \theta \pm \left[\left(\frac{1}{2}Y^2 \sin^2 \theta \right)^2 + (1-X)^2 Y^2 \cos^2 \theta \right]^{1/2}} \quad (24)$$

A-H equation describes the refractive index for EM waves in magnetized plasma. The \pm sign in A-H equation is associated with Y , which is related to the magnetic cyclotron frequency ω_B , and further to magnetic field \mathbf{B} . The \pm sign shows that the magnetic field makes the plasma an anisotropic medium. The anisotropy implies that the wave's propagation speed and attenuation depend not only on the frequency of EM waves but also on its direction of propagation relative to the magnetic field.

For space plasma is collisionless, the typical number density n_e is on the order of 1 cm^{-3} , the typical number temperature is on the order of 10^4 K , and the typical magnetic field B is on the order of 10 nT . Under the above conditions, $\omega_p \sim 10^5 \text{ Hz}$, $\omega_B \sim 10^3 \text{ Hz}$, and $\nu \sim 10^{-8} \text{ Hz}$, thus, $X \gg Y^2 \gg Z$. Thus, the space plasma can be assumed to be collisionless and un-magnetized plasma. And A-H Equation (24) further degenerates as follow,

$$N^2 = 1 - X \quad (25)$$

Comparing Equation (24) and Equation (25), it reveals that without the magnetic field, the plasma changes from anisotropic medium to isotropic one, the propagation of EM waves in the isotropic plasma becomes simplified.

The group refractive index N_g can be derived as follow,

$$N_g = \frac{\partial(N\omega)}{\partial\omega} = \frac{\partial \left[\omega \left(1 - \frac{\omega_p^2}{\omega^2} \right) \right]}{\partial\omega} \approx 1 + \frac{X}{2} = 1 + \frac{Kn_e}{2f^2} \quad (26)$$

Here, f is the EM wave frequency, $K = e^2/(4\pi m_e \epsilon_0) = 80.6 \text{ m}^3 \text{s}^{-2}$.

The time (τ) of EM waves propagating a distance L in space plasma is,

$$\tau = \int_L \frac{ds}{v_g} = \int_L \frac{ds}{c/N_g} \quad (27)$$

where c is the speed of light in vacuum, The time delay ($\Delta\tau$) of the EM waves propagation in space plasma relative to the vacuum case is,

$$\Delta\tau = \frac{1}{c} \int_L (1 + \frac{Kn_e}{2f^2}) ds - \frac{L}{c} = \frac{K}{2cf^2} \int_L n_e ds \quad (28)$$

$\int_L n_e ds$ is the integrated electron number density along the laser link. According to Equation (28), the OPD can be calculated as following,

$$\Delta l = c\Delta\tau = \frac{K}{2f^2} \int_L n_e ds \quad (29)$$

According to Equation (29), we can obtain the OPD noise Δl due to laser propagation in space plasma.

2.2 The model of acceleration noise due to space magnetic field

An object with a magnetic moment in the magnetic field will be subjected to a magnetic moment force \mathbf{F}_M , which can be expressed as follows,

$$\mathbf{F}_M = \nabla(\mathbf{M} \cdot \mathbf{B}) \quad (30)$$

where, \mathbf{B} is the background magnetic field, and \mathbf{M} is the magnetic moment of the TM. Here, \mathbf{B} is composed of the spacecraft magnetic field \mathbf{B}_{sc} and the space magnetic field \mathbf{B}_{sp} , $\mathbf{B} = \mathbf{B}_{sp} + \mathbf{B}_{sc}$; And the \mathbf{M} including the remanent magnetic moment \mathbf{M}_r and the inductive magnetic moment \mathbf{M}_i , $\mathbf{M}_{tm} = \mathbf{M}_r + \mathbf{M}_i$. And both \mathbf{B}_{sp} and \mathbf{B}_{sc} can induce \mathbf{M}_i ,

$$\mathbf{M}_i = \mathbf{M}_{isc} + \mathbf{M}_{isp} = \frac{\chi_m V \mathbf{B}_{sp}}{\mu_0} + \frac{\chi_m V \mathbf{B}_{sc}}{\mu_0} \quad (31)$$

here, χ_m is magnetic susceptibility, V is the volume of the TM, and μ_0 is the vacuum magnetic permeability.

Take magnetic field \mathbf{B} , magnetic moment \mathbf{M} and Equation (31) into Equation (30), the acceleration noise due to the magnetic moment force can be obtained as,

$$\begin{aligned} a &= \frac{1}{m} \nabla [(\mathbf{M}_r + \mathbf{M}_{isp} + \mathbf{M}_{isc}) \cdot (\mathbf{B}_{sp} + \mathbf{B}_{sc})] \\ &= \frac{1}{m} \nabla \left(\mathbf{M}_r \cdot \mathbf{B}_{sp} + \mathbf{M}_r \cdot \mathbf{B}_{sc} + \frac{2\chi_m V}{\mu_0} \mathbf{B}_{sp} \cdot \mathbf{B}_{sc} + \frac{\chi_m V}{\mu_0} B_{sp}^2 + \frac{\chi_m V}{\mu_0} B_{sc}^2 \right) \end{aligned} \quad (32)$$

where, m is the mass of the TM.

In this work, we focus only on the acceleration noise due to the space magnetic field, and neglect the terms without space magnetic field (second and fifth terms in Equation (32)). Thus, Equation (32) can be simplified as follow,

$$a_M = \frac{1}{m} \nabla \left(\mathbf{M}_r \cdot \mathbf{B}_{sp} + \frac{2\chi_m V}{\mu_0} \mathbf{B}_{sp} \cdot \mathbf{B}_{sc} + \frac{\chi_m V}{\mu_0} B_{sp}^2 \right) \quad (33)$$

According to the vector operation rules $\nabla(\mathbf{f} \cdot \mathbf{g}) = (\mathbf{f} \cdot \nabla)\mathbf{g} + (\mathbf{g} \cdot \nabla)\mathbf{f} + \mathbf{f} \times (\nabla \times \mathbf{g}) + \mathbf{g} \times (\nabla \times \mathbf{f})$, where \mathbf{f} and \mathbf{g} are vectors in this formula, the first term of Equation (33) can be expanded as follow,

$$\nabla(\mathbf{M}_r \cdot \mathbf{B}_{sp}) = (\mathbf{M}_r \cdot \nabla)\mathbf{B}_{sp} + (\mathbf{B}_{sp} \cdot \nabla)\mathbf{M}_r + \mathbf{M}_r \times (\nabla \times \mathbf{B}_{sp}) + \mathbf{B}_{sp} \times (\nabla \times \mathbf{M}_r) \quad (34)$$

According to the Ampere-Maxwell law, $\nabla \times \mathbf{B} = \mu_0 \mathbf{j} + \varepsilon_0 \mu_0 \partial \mathbf{E} / \partial t$, which contains conduction current and displacement current. Since the TM is drag-free and floating in the satellite, has no direct contact with the satellite, and it is wrapped by layers of the satellite, there should be no conduction current. Thus, Equation (35) can be written as,

$$\nabla(\mathbf{M}_r \cdot \mathbf{B}_{sp}) = (\mathbf{M}_r \cdot \nabla)\mathbf{B}_{sp} + (\mathbf{B}_{sp} \cdot \nabla)\mathbf{M}_r + \mathbf{M}_r \times \left(\frac{\varepsilon_0 \mu_0 \partial \mathbf{E}_{sp}}{\partial t} \right) + \mathbf{B}_{sp} \times (\nabla \times \mathbf{M}_r) \quad (35)$$

Similarly, the second term in Equation (33) can be written as,

$$\nabla(\mathbf{B}_{sp} \cdot \mathbf{B}_{sc}) = (\mathbf{B}_{sp} \cdot \nabla)\mathbf{B}_{sc} + (\mathbf{B}_{sc} \cdot \nabla)\mathbf{B}_{sp} + \mathbf{B}_{sp} \times \left(\frac{\varepsilon_0 \mu_0 \partial \mathbf{E}_{sc}}{\partial t} \right) + \mathbf{B}_{sc} \times \left(\frac{\varepsilon_0 \mu_0 \partial \mathbf{E}_{sp}}{\partial t} \right) \quad (36)$$

According to the vector operation rule $\nabla(uv) = u\nabla v + v\nabla u$, where u and v are scalars in this formula, the third term of Equation (33) can be written as,

$$\nabla(B_{sp}^2) = 2B_{sp} \nabla B_{sp} \quad (37)$$

Take Equations (35), (36), and (37) into Equation (33), the magnetic moment force \mathbf{F}_M is as follow,

$$\begin{aligned} \mathbf{F}_M = & 2(\mathbf{M}_{isp} \cdot \nabla)\mathbf{B}_{sc} + [(\mathbf{M}_r + 2\mathbf{M}_{isc}) \cdot \nabla]\mathbf{B}_{sp} \\ & + \mathbf{M}_{isp} \times \frac{\varepsilon_0 \mu_0 \partial \mathbf{E}_{sc}}{\partial t} + \mathbf{M}_{isc} \times \frac{\varepsilon_0 \mu_0 \partial \mathbf{E}_{sp}}{\partial t} + 2B_{sp} \nabla B_{sp} \end{aligned} \quad (38)$$

Reorganize the Equation (38), and the acceleration noise can be written as the following 5 terms,

$$\begin{cases} \mathbf{a}_{M1} = \frac{2}{m}(\mathbf{M}_{isp} \cdot \nabla)\mathbf{B}_{sc} \\ \mathbf{a}_{M2} = \frac{1}{m}[(\mathbf{M}_r + 2\mathbf{M}_{isc}) \cdot \nabla]\mathbf{B}_{sp} \\ \mathbf{a}_{M3} = \frac{1}{m}(\mathbf{M}_r + 2\mathbf{M}_{isc}) \times \frac{\varepsilon_0 \mu_0 \partial \mathbf{E}_{sp}}{\partial t} \\ \mathbf{a}_{M4} = \frac{2}{m}(\mathbf{M}_{isp}) \times \frac{\varepsilon_0 \mu_0 \partial \mathbf{E}_{sc}}{\partial t} \\ \mathbf{a}_{M5} = \frac{2}{m}M_{isp} \nabla B_{sp} \end{cases} \quad (39)$$

In order to further reduce the acceleration noise caused by magnetic field, magnetic shielding has been proposed, which is commonly represented by the magnetic

shielding factor ξ_m . The acceleration noise after considering the magnetic shielding is represented as a_M/ξ_m .

The TM with residual charge in the magnetic field is subject to the Lorentz force. In space, there are also energetic particles, e.g., galactic cosmic ray (GCR) [55, 56] and solar energetic particle (SEP) [57, 58]. The energetic particles can penetrate the protection of the TM, bombard the TM, and cause it to become charged [18, 59]. The Lorentz force of charged TM in the space magnetic field is as following,

$$a_L = \frac{1}{m} q \mathbf{v} \times \mathbf{B}_{sp} \quad (40)$$

where, q is the charge of the TM, \mathbf{v} is the velocity of the TM.

2.3 Space environment data and models

2.3.1 In-situ observation of space plasma and magnetic field

The heliocentric space-borne GW detectors (LISA and TJ) rotate around the Sun at a distance of about 1 AU from the Sun, and they consist of three satellites forming an equilateral triangular laser interferometric link with arms of millions of kilometers in length. Of these, LISA is planned to be deployed about 50 million kilometers behind the Earth, with an interferometric arm length of about 2.5 million kilometers; And TJ about 50 million kilometers in front of the Earth, with an arm length of about 3 million kilometers. The orbits of both LISA and TJ are completely dipped in the solar wind plasma [7, 60, 61]. Although there is no in-situ observation of space plasma and magnetic field near the orbits of LISA and TJ at present, since the symmetry of the solar wind parameters in the ecliptic plane, the observation at the 1st Sun-Earth Lagrange (L1) point, can be used to analyse the space environment problems for LISA.

There are in-situ satellites to get the space plasma and magnetic field at L1 point, e.g. Wind [62], ACE [63], and so on. They can detect the space plasma number density n_i and n_e , velocity v , temperature T , space magnetic field B_x, B_y, B_z , and other parameters at L1 point. Based on the in-situ observations in the past decades, the solar wind dataset OMNI has been established [64], and the in-situ observation data can be used to study the effects of space environment on the space-borne GW detections. In particular, since acceleration noise due to space magnetic field is localised, the in-situ observation data can be used directly to calculate space magnetic acceleration noise [20] (Figure 2).

The geocentric GW detector, TQ, is at an altitude of about 100000 km from the center of the Earth, also forms an equilateral triangular laser interferometric links to the detect the GWs, with the arm length of about 170000 km [65–67]. The Earth’s magnetosphere is the result of the interaction of the solar wind with its intrinsic magnetic field, and the solar wind blowing onto the Earth’s magnetosphere causes the magnetopause to be compressed, and the magnetotail to be stretched [41]. The magnetopause and bow shock are often considered to be the boundary between the solar wind and the Earth’s magnetosphere [68, 69]. The subsolar point of the magnetosphere is often at a distance of about 10 R_E from the Earth, which can be compressed to $< 7 R_E$ when the solar wind dynamic pressure P_{dyn} is strong, and it can be $> 7 R_E$

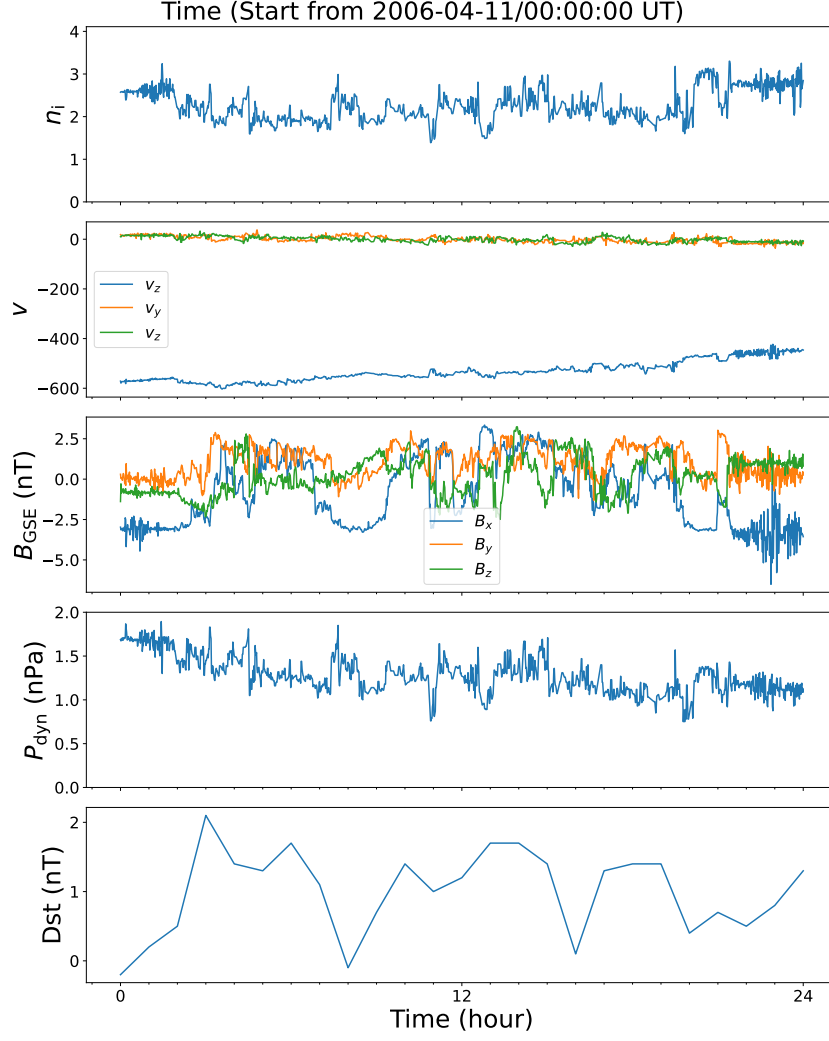


Fig. 2 Space plasma and magnetic field data from OMNI. n_i , v , B in GSE coordinate, P_{dyn} , and Dst index in 2006-04-11.

when P_{dyn} is weak [70]; the bow shock nose region is often at a distance of about 12 R_E from the Earth, and the bow shock nose region can be compressed to $< 9 R_E$ when P_{dyn} is strong, and it can be $> 15 R_E$ when P_{dyn} is weak [71]. The orbit of TQ is at a distance of about 15.6 R_E from the Earth's center, and the TQ orbit is exactly in the region where the solar wind interacts with the Earth's magnetosphere. Besides the magnetopause and bow shock, the structures such as cusp regions, magnetotail, and lobe regions are formed during the interaction between the solar wind and the Earth's magnetosphere. As solar wind conditions change, the geometry and parameters of these structures also change, solar wind observations can be used as inputs, for

modelling the interaction between the Earth’s magnetosphere and the solar wind by using MHD.

Around the orbit of geocentric GW detectors, there are in-situ observation of space plasma and magnetic fields by the satellites e.g., Clusters [72, 73], THEMIS [74], and MMS [75]. Although the orbits of these satellites are different from TQ, these satellites are similar to TQ in that they all pass through the signature regions of bow shock, magnetosheath, magnetopause, cusp region, magnetotail, lobe region, and so on. The observation of these satellites can roughly reflect the approximate space magnetic field and plasma around the TQ orbit. Therefore, the in-situ observations of Earth’s magnetosphere can be used as approximate alternative data to study the space magnetic field effect of TQ.

2.3.2 Space magnetic field model – Tsyganenko Model

Tsyganenko space magnetic field model is a widely used empirical model that describes Earth’s magnetospheric magnetic field [76]. Developed by Tsyganenko and his collaborators over several decades [77–82], the model is based on a large dataset of spacecraft observations and provides a parameterized representation of the geomagnetic field under varying solar wind and geomagnetic conditions. It is a cornerstone in the field of magnetospheric physics, aiding in the study of space weather and Earth’s magnetic environment.

The Tsyganenko model fits the measured magnetic field data using parameterized mathematical functions that represent different current systems contributing to the magnetosphere magnetic field [79, 82]. These current systems include, Ring Current, encircling Earth and intensifying during geomagnetic storms; Tail Current, extending into the magnetotail, shaped by solar wind pressure; Magnetopause Current, currents on the boundary between the magnetosphere and solar wind; Field-Aligned Currents, connecting the magnetosphere to the ionosphere [83, 84].

The Tsyganenko model adjusts the magnetic field based on real-time or average geophysical and solar wind conditions, using input parameters such as solar wind dynamic pressure (P_{dyn}), which is the dominant term in the magnetic pressure balance of the Earth’s magnetosphere, governs the compression of the magnetosphere [85, 86]; Dst Index, indicates the strength of the ring current and geomagnetic activity [87]; interplanetary magnetic field (IMF), which impacts the exchange of energy and plasma between the solar wind and Earth’s magnetosphere by reconnection processes at the magnetopause, and the asymmetry of the magnetosphere [88]; Position in geocentric solar magnetic (GSM) coordinates, the model calculates the magnetic field at specific locations within the magnetosphere [78, 79, 82].

Based on the inputs, the Tsyganenko model uses a set of analytical functions to represent the contribution of each current system (including the ring current, magnetopause current, tail current, and field-aligned currents) to the overall magnetic field [79, 82]. And combining with the Earth’s dipole magnetic field, the Tsyganenko model calculates the magnetic field vector \mathbf{B} with temporal and spatial variation. The output \mathbf{B} reflects the combined influence of all major magnetospheric current systems under the specified conditions (Figure 3).

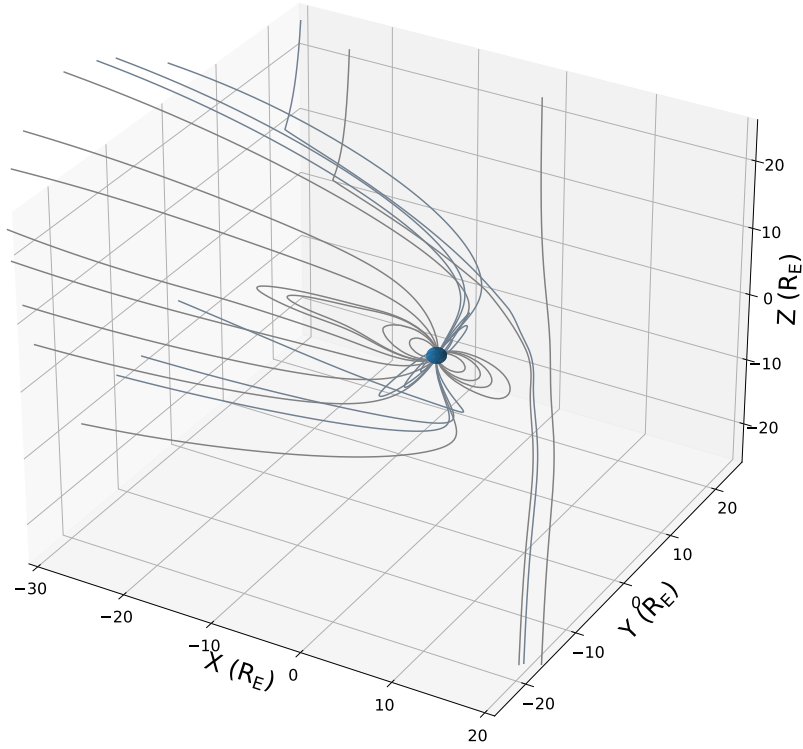


Fig. 3 The magnetic field around the geocentric GW detector that calculated by the Tsyganenko model [89].

There are a wide applications for the Tsyganenko model in magnetosphere studies. It provides insights into the structure and dynamics of the Earth's magnetosphere under different conditions, and helps to understand physical processes such as magnetic reconnection, particle trapping, and current systems. The Tsyganenko model is also widely used in space weather research. It is used to study the effects of geomagnetic storms and substorms on the magnetosphere, and supports the modeling of radiation belts and plasma dynamics. For satellite missions, the Tsyganenko model helps predict magnetic field conditions for spacecraft in Earth's orbit, and supports the design and operation of space missions by estimating radiation and magnetic field exposures.

Here, the Tsyganenko model is suitable for the study of space magnetic acceleration noise for geocentric GW detector, e.g. TQ.

2.3.3 Space environment MHD simulation model: SWMF

MHD simulation is used widely in the study of astrophysical [90, 91], laboratory [92], solar [93, 94] and space [95] plasmas. Space Weather Modeling Framework (SWMF)

[95] is a well-known MHD simulation model in heliophysics, it has been widely used and validated [96, 97]. The SWMF is a comprehensive computational framework designed to simulate and predict space weather phenomena. Developed and maintained by the University of Michigan’s Center for Space Environment Modeling (CSEM), it integrates multiple physics-based models to simulate various regions of the space environment, from the Sun to Earth and beyond.

SWMF connects different physics models as modules, allowing users to customize and couple models based on their research needs. Examples of models include those for the solar corona, heliosphere, Earth’s magnetosphere, ionosphere, thermosphere, and inner magnetosphere. The SWMF integrates a suite of physics-based models representing different regions of the space environment, from the Sun to Earth and beyond. Each model specializes in a specific domain: Solar Corona model (SC) and Inner Heliosphere model (IH) simulate the Sun’s outer atmosphere and the propagation of the solar wind. Global Magnetosphere model (GM) and Inner Magnetosphere model (IM) capture the dynamics of Earth’s magnetic field and energetic particles. Ionosphere Electrodynamics model (IE) and Thermosphere-Ionosphere model (TI) represent the upper atmosphere’s electrodynamics and thermodynamics, and additional models, such as the SEP and Plasmasphere (PS) models, address specialized phenomena like particle acceleration and cold plasma behavior [95]. The SWMF’s modular design allows researchers to run these models independently or as coupled systems, facilitating comprehensive simulations of multi-region interactions.

At the core, the SWMF is built upon the principles of physics that govern the behavior of plasma and magnetic fields across different regions of space. It employs MHD to describe the macroscopic behavior of plasmas in domains such as the solar corona and Earth’s magnetosphere [95]. Kinetic and particle-based approaches are used in regions where particle dynamics dominate, such as the inner magnetosphere and radiation belts. Additionally, the SWMF integrates electrodynamics to model ionospheric currents and thermodynamics to describe the upper atmosphere’s behavior. Each model within the SWMF represents a specific region of the space environment, and the framework facilitates their coupling to capture the complex interactions between these regions [95]. The plasma and magnetic field around the orbital plane of GW detectors that obtained by the SWMF is shown in Figure 4.

The SWMF has diverse applications in both scientific and practical contexts [98]. It is a valuable tool for researchers studying the fundamental physics of the Sun-Earth system, enabling simulations of solar flares, CME, solar wind-magnetosphere coupling, geomagnetic storms, and ionospheric disturbances, and so on. The framework also supports space weather forecasting efforts, providing real-time predictions for agencies such as NASA and NOAA. These forecasts are crucial for protecting satellites, safeguarding astronauts during space missions, and mitigating the risks posed by space weather to critical infrastructure on Earth.

Beyond Earth, the SWMF is used to model the space environments of other planetary systems, such as Mars and Jupiter, aiding planetary science and exploration. Its adaptability and scalability also make it an essential tool for planning for future missions in an increasingly space-dependent world.

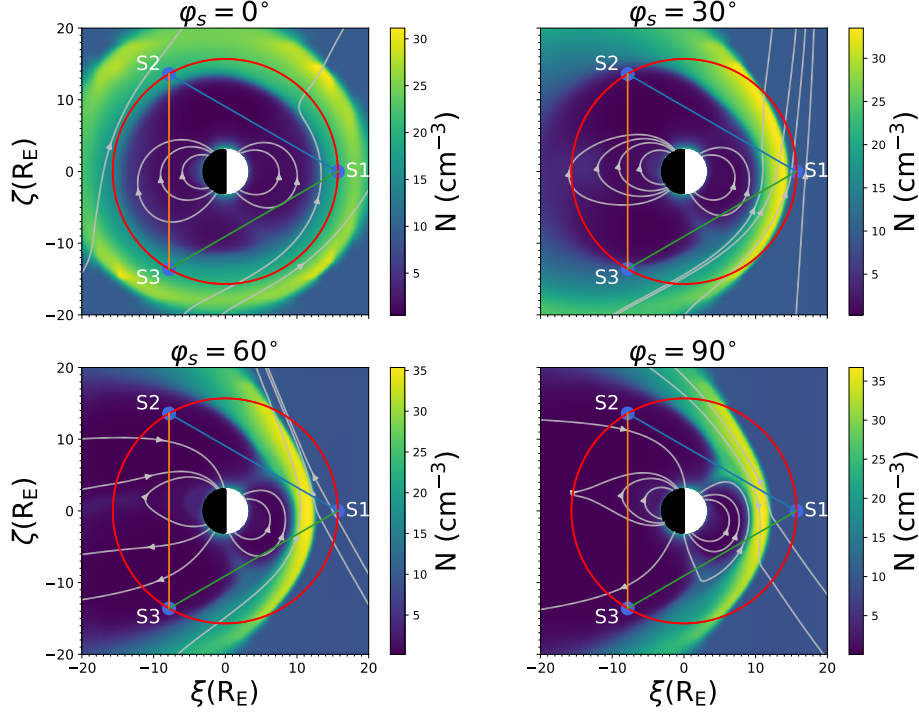


Fig. 4 The simulation results of the plasma and magnetic field around the orbital plane of GW detectors by the SWMF [20].

MHD simulation can get the spatial and temporal evolution of the plasma [99–101]. Thus, MHD simulations are suitable for the study of LPN in the detection of space-borne GW [16, 20]. It should be noted that plasma is quasi-neutral, so that the electrons and ions number densities are approximately equal. In the MHD simulation, the electrons and protons number densities are set to be equal, and the deviation from quasi-neutrality in the plasma along the laser link and in time is ignored. The proton number density is easier to obtain in the observation, and the deviation from quasi-neutrality in the plasma observation is also ignored, so that the observation of proton number density is set to be equal to electron number density in the study of LPN.

3 Laser propagation effect in space plasma for space GW detection

3.1 Cases study of laser propagation noise

The dispersion effect of laser propagation in space plasma leads to time delay, and generates OPD noise, which affects the space-borne GW detection. As shown in Equation (29), the LPN is proportional to the integral of n_e along the laser link. At present,

all the observations of space plasma are in-situ, and the in-situ observations can only obtain the space plasma data at one point along the laser link. Since the plasma parameters of the solar wind are variable rather than stable, the plasma distribution along the laser link is also variable. The MHD simulation can obtain the plasma distribution and evolution along the laser link, making it suitable for studying the LPN of space-borne GW detections.

An MHD simulation model, SWMF [95], with the temporal resolution of 60 s and the finest spatial resolution of about $1/8 R_E$, is used to investigate the LPN for space-borne GW detection [15, 16]. Taking the solar wind parameters (e.g., plasma number density n_e , bulk flow velocity of space plasma v , magnetic field B , etc.) as inputs, the SWMF simulation can yield the evolutionary characteristics of the plasma parameters in the vicinity of the orbital plane of the geocentric GW detectors, and the results of plasma parameters around TQ's orbit planes are shown in Figure 5. The results of the SWMF simulation show the typical structures of the Earth's magnetosphere, such as the bow shock, the magnetopause, the magnetosheath, the cusp region, and so on. As shown in the Figure 5, the plasma number density n_e of the solar wind is higher than that in the magnetosphere. Since the bow shock, magnetosheath and magnetopause are formed by the compression of the Earth's magnetosphere by the solar wind blowing to the Earth, the magnetosheath, which is the downstream of the bow shock, is a compressed region, and its density is significantly higher than that of the other regions. The three satellites of TQ are deployed in geocentric orbit with an orbital altitude of about 100000 km, the three satellites form an equilateral triangular, and they are connected by the laser interferometric links. The normal of TQ's orbital plane is aligned with a white dwarf binary systems, J0806, and the angle between the orbital plane normal to the ecliptic plane is 4.7 degrees, it means that the orbital plane is almost perpendicular to the ecliptic plane [67, 102]. The angle between the normal of TQ orbital plane and the direction of the Sun-Earth line is defined as φ_s , which has a periodicity of 1 year. As shown in Figure 5, the laser links of TQ pass through various regions of the Earth's magnetosphere and solar wind, where n_e along the laser link increases as it passes through the magnetosheath.

The SWMF simulation is used to obtain plasma parameters evolution with a time length of 6 hours, and based on simulation results, the LPN of the TQ is calculated [15], and the time series of the LPN is shown in Figure 6. Note that the result is shown in phase deviation, the corresponding LPN needs to be multiplied by the laser wavelength λ , and the LPN is on the order of 1 pm. Based on the simulation result, the LPN of single links are calculated, and it showed that the LPN at 6 mHz is about 20% of the TQ's displacement requirement [15]. Changing the orbital altitude of TQ satellites from 10^5 to 0.7×10^5 and 1.5×10^5 km, so that the arm length of the laser links are $0.7\sqrt{3} \times 10^5$ and $1.5\sqrt{3} \times 10^5$ km. The LPN in the cases of arm lengths $0.7\sqrt{3} \times 10^5$ and $1.5\sqrt{3} \times 10^5$ km are also investigated. It is found that the LPN are about 14% and 41% of the TQ's displacement requirement for the arm lengths of $0.7\sqrt{3} \times 10^5$ and $1.5\sqrt{3} \times 10^5$, respectively [15]. This is because when the arm length increases, the proportion of the laser link in the solar wind and magnetosheath is higher than when the laser link is short. And considering that n_e in the solar wind and magnetosheath are about several times and tens times higher than in the magnetosphere, it leads to

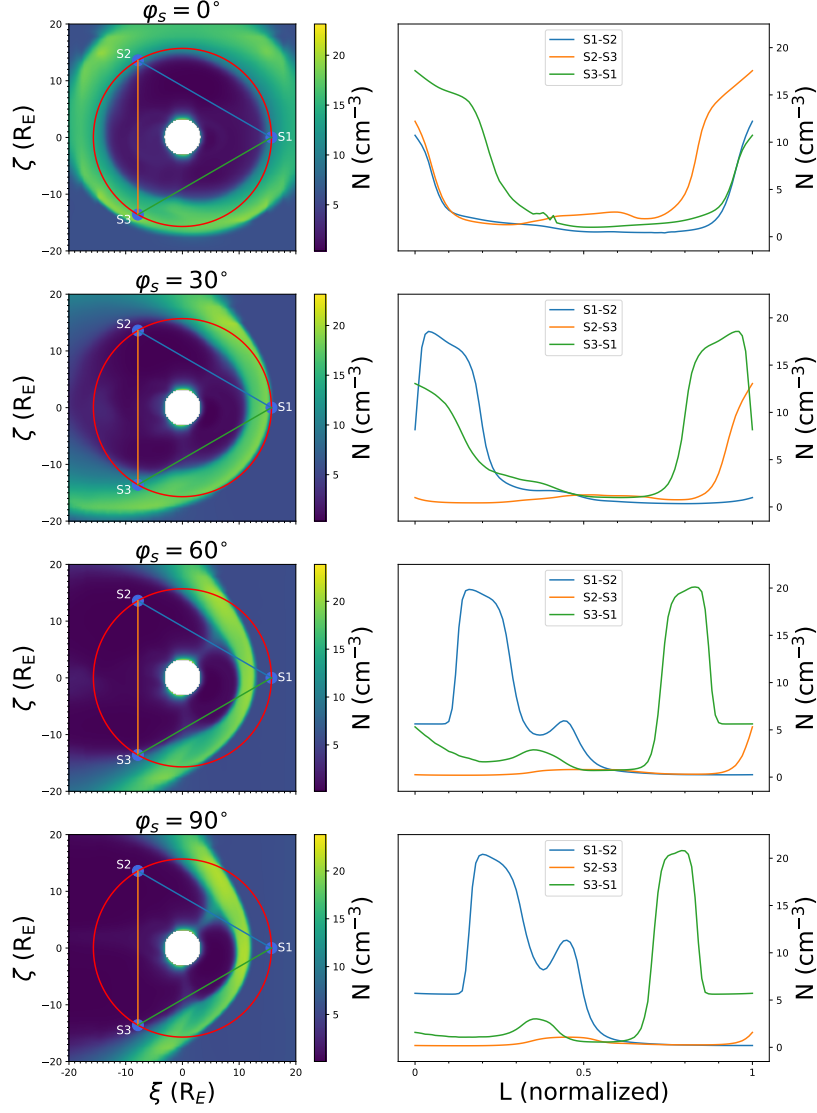


Fig. 5 The left panels are the number density distribution of electron on the orbital plane of the geocentric GW detector, the red circle is the TQ's orbit, the blue, orange, and green lines are the laser links; The right panels are the electron number density along the laser links [16].

an increase in the ratio of LPN to TQ's displacement noise requirement as the arm length increases.

In order to study the LPN over an entire TQ's cycle (3.65 days), the spatial and temporal distribution of the plasma during more than a cycle of TQ is obtained by using SWMF simulations. Based on the MHD simulation results, the LPN is investigated for $\varphi_s = 0^\circ, 30^\circ, 60^\circ$, and 90° cases, where the acute angle of ϕ_s is taken as

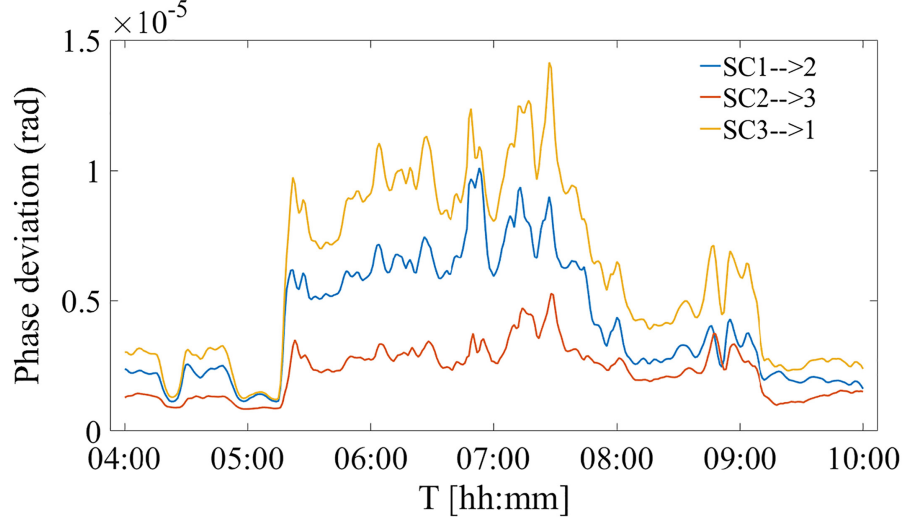


Fig. 6 The LPN time series of the single links for geocentric GW detector TQ [15].

φ_s [16]. Although the LPN noise of single links are important for analysing the laser propagation effect, the laser interferometric method is used in practical space-borne GW detection. Michelson interferometric combination is a typical laser interferometric combination. The LPN in time domain for the single-link and Michelson combination cases in a TQ orbital cycle are shown in Figure 7 [16]. It shows that the LPN is more consistent in the time domain at $\varphi_s = 30^\circ$, 60° , and 90° , whereas the LPN of $\varphi_s = 0^\circ$ is smaller than those of $\varphi_s = 30^\circ$, 60° , and 90° . As shown in Figure 7, the LPN is about 1 pm in the time domain for a single link and about ± 3 pm for the Michelson combination. These results show that the LPN is on the order of magnitude of TQ's displacement requirement in the time domain, and suggest that the LPN is a noise source that deserves to be taken seriously. In addition, the ASD of the LPN for Michelson combination case is calculated and displayed in Figure 8 [16]. It shows that the LPN of Michelson combination is below the requirement of TQ's displacement noise over the full frequency band, and the ratio of the LPN to the requirement of TQ's displacement noise is largest at about 10 mHz with the value of about 30%. It suggests that although LPN does not exceed the TQ's requirement in frequency domain, it is still a noise source that deserves attention.

In addition, wavefront distortion can be generated during laser propagation in space plasma. Based on the SWMF, the wavefront distortion is studied for TQ, and the result show that the wavefront distortion is on the order of 10^{-9} rad, which is 3 orders of magnitude lower than the budget (10^{-6} rad) of TQ [103]. It indicates that the wavefront distortion during laser propagation is neglected.

Various solar activities can cause variations of the plasma number density n_e . For example, on long timescales, n_e of the solar wind has a periodicity of about 11 years [104], and on short timescales, when there is a solar eruption encounter the GW detectors, it can lead to dramatic changes of n_e along the laser link. The value of n_e can differ by hundreds of times in different solar wind scenarios, leading to large

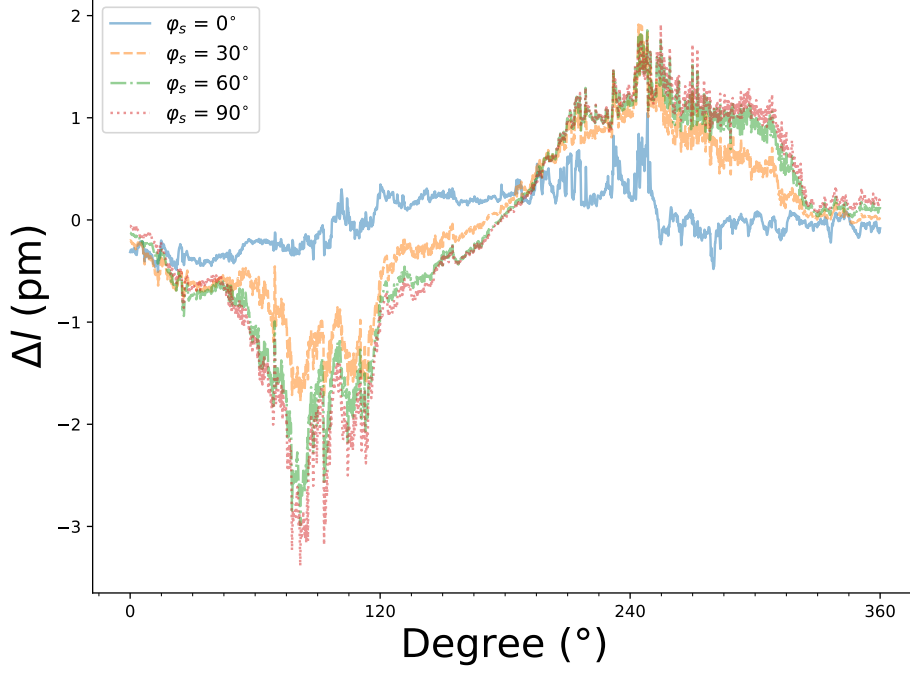


Fig. 7 The LPN time series of the Michelson combination for geocentric GW detector TQ [16].

differences in the LPN. Thus, it is therefore necessary to evaluate the LPN in different solar wind scenarios. Kp index is an significant index that reflects geomagnetic activity, the MHD simulation is used to study the LPN of TQ when Kp index is large, and find that when the Kp index is large, the LPN also increases [105].

For heliocentric GW detectors, such as LISA, [14] studied the LPN of LISA for 20 different solar wind conditions during 1997-1998. The time series data of n_e is got from the observations by the WIND/SWE instrument at the L1 point, and the duration of n_e for the 20 cases are at least 24 hours. Since the observations of Wind/SWE is in-situ, the distribution of n_e along the laser link of LISA cannot be obtained. Due to the lack of the spatial distribution of n_e , [14] assumed that n_e along the LISA laser link arm is uniform with only temporal variations. The minimum value n_e for the 20 events they is on the order of 0.1 cm^{-3} , and the maximum value reaches the order of 10 cm^{-3} ; 6 of the total 20 events are eruptions events such as CMEs and magnetic storms. In addition, the ASDs of the LPN is calculated, and compare the ASDs with the displacement measurement requirement of LISA, it shows that the LPN of LISA is about several times higher than the displacement noise measurement of LISA [14].

For geocentric GW detectors, such as TQ, [106] investigates the LPN based on SWMF for solar wind dynamic pressure are small ($\bar{P}_{\text{dyn}} \approx 0.79 \text{ nPa}$) and large ($\bar{P}_{\text{dyn}} \approx 5.05 \text{ nPa}$). The MHD simulation results are shown in the left panels of Figure 9, which illustrate the cases of large P_{dyn} (rows 1 and 3) and small P_{dyn} (rows 2 and 4) for $\varphi_s = 0^\circ$ (upper panels) and $\varphi_s = 90^\circ$ (lower panels), respectively. For strong P_{dyn} , on

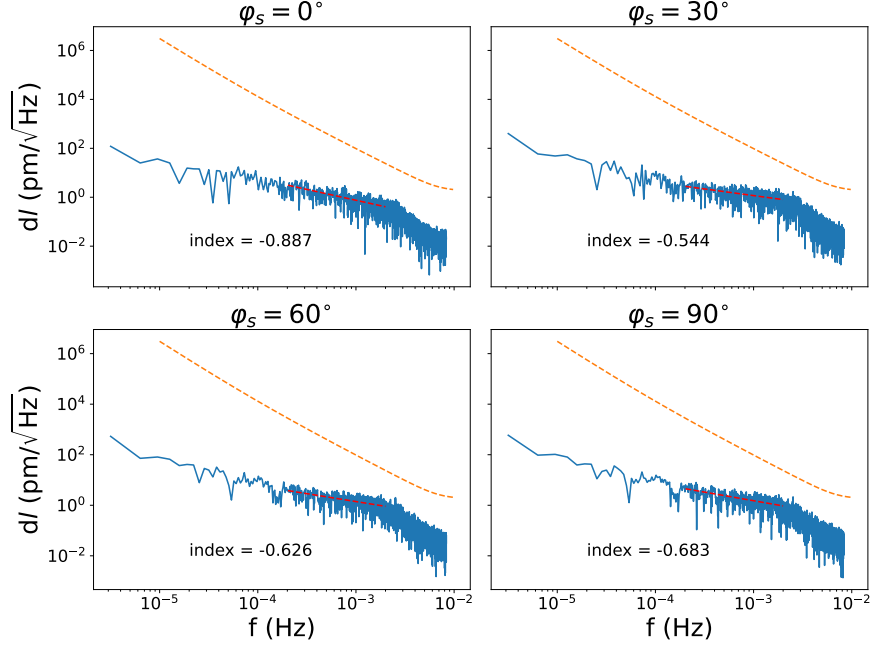


Fig. 8 The LPN's ASDs of the Michelson combination for geocentric GW detector TQ [16].

$\varphi_s = 0^\circ$ orbital plane, the Earth's magnetosphere is compressed to within about 16 R_E , and TQ's orbit is almost outside the bow shock; on the $\varphi_s = 90^\circ$ orbital plane, the subsolar point is compressed to within about 10 R_E . For weak P_{dyn} , on $\varphi_s = 0^\circ$ orbital plane, the bow shock and magnetopause are expanded beyond about 16 and 20 R_E , respectively, and TQ's orbit is almost inside magnetopause; on the $\varphi_s = 90^\circ$ orbital plane, the subsolar point is expanded beyond about 16 R_E , and TQ's orbit is almost inside the bow shock. For strong P_{dyn} , n_e along the laser link increases and the value can exceed 100 cm^{-3} ; for P_{dyn} , n_e along the laser link decreases to the order of 1 cm^{-3} . The difference between the maximum of n_e for the large P_{dyn} and for the small P_{dyn} is more than an order of magnitude.

Combining the simulation result of n_e and Equation (29), the time series of LPN for strong and weak P_{dyn} can be obtained. The LPN can reach 10 pm when P_{dyn} is strong, while the LPN is about 1 pm when P_{dyn} is weak. The LPN under strong P_{dyn} is about 10 times that under weak P_{dyn} . In addition, the ASDs of LPN can be obtained. For P_{dyn} is weak, the ratio of the LPN to requirement of TQ's displacement noise is largest at about 10 mHz with the value of about 10%. Whereas, for P_{dyn} is strong, the ratio of the LPN to requirement of TQ's displacement noise is largest at about 10 mHz with the value of nearly 100%. The strong P_{dyn} event corresponds to a strong solar eruption event, the well known Halloween event, and in general, P_{dyn} is strong when the solar eruption is strong, which indicates that the effect of the LPN noise is crucial when a strong TQ encounters a strong solar eruption.

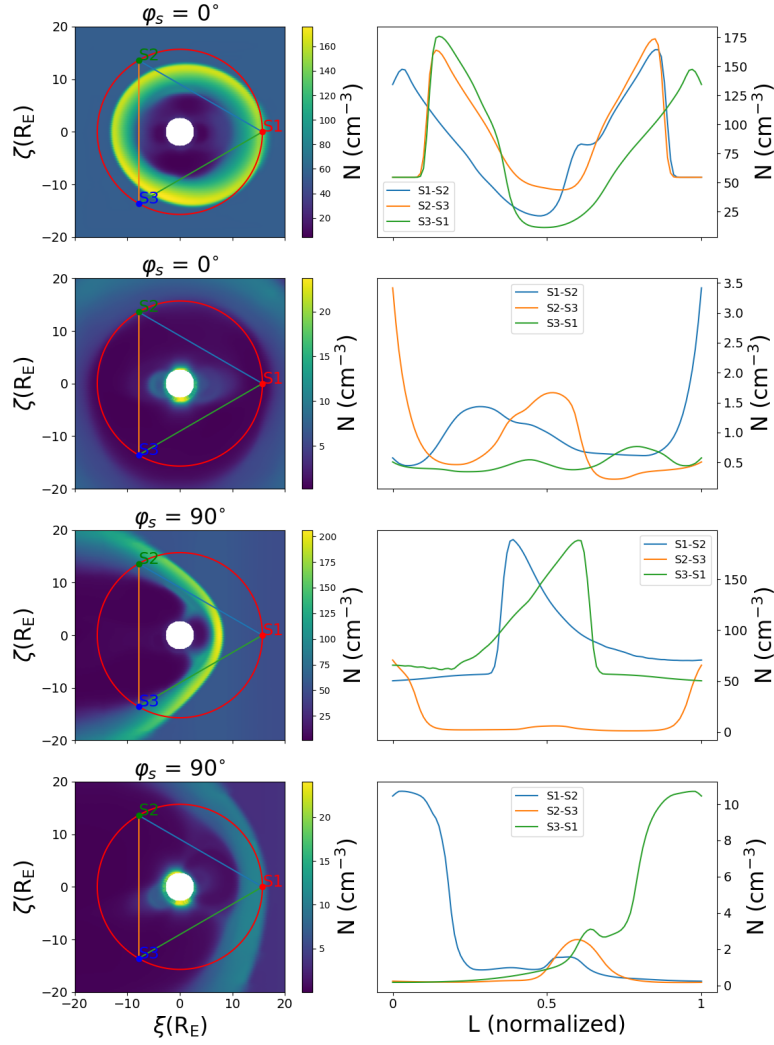


Fig. 9 Similar to Figure 5. The first and third rows are the number density distribution on the orbital plane and along the laser links for \bar{P}_{dyn} is large, The second and forth rows are the number density distribution on the orbital plane and along the laser links for \bar{P}_{dyn} is small [106].

3.2 Statistical study of laser propagation noise

The planned run time of the space-borne GW detection is more than 4 years and, if everything goes well, the overall run time can be up to more than 10 years [7], which is about 1 solar cycle. Statistical studies of the LPN of space-borne GW detections are needed to assess the LPN noise for various solar activity scenarios over a long time scale.

For heliocentric GW detector, LISA, based on the data of n_e for more than 600 days that obtained by Wind/SWE, the evaluation of the LPN noise is studied [17]. By assuming that the spectrum index of n_e in the solar wind is consistent with the spectra indices of the space magnetic field and plasma velocity, both of which roughly obey the Kolmogorov spectrum, and under the conditions of the Taylor hypothesis [107], the relationship between the spectrum of the local plasma number density ($S_{Ne}(f)$) and the spectrum of the plasma number density on the laser link ($S_L(f)$) was derived [17],

$$S_L(f) \approx (L\chi)^2 \left(\frac{25}{9}\right) \beta^{5/3} \left(\frac{V}{2\pi Lf}\right) S_{Ne}(f) \quad (41)$$

where, L is the arm length of heliocentric GW detector, V is the bulk flow velocity of space plasma, β is geometrical factor, f is frequency, $\chi = \frac{\lambda^2 e^2}{2\pi m_e c^2}$. Here, λ is laser wavelength, c is the light speed, m_e is the mass of electron.

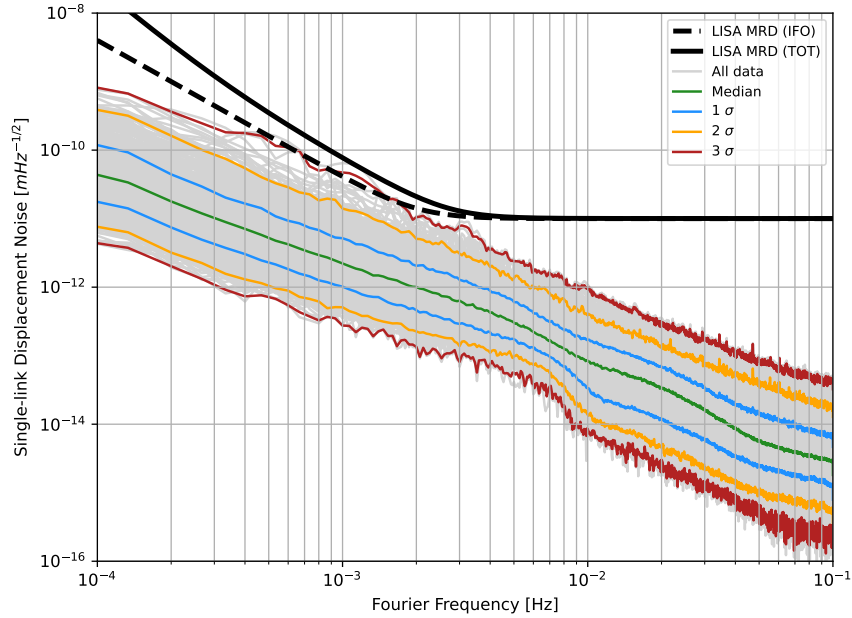


Fig. 10 The LPN's ASDs of single link for LISA based on the in-situ observation of Wind [17]. The gray curves are the daily ASDs of the LPN. The black curves are the single link sensitivity requirements of LISA [17].

Based on Equation (41) and the observations of Wind/SWE, about 600 daily ASDs of LPN for the single link between 1997 and 1998 is obtained [17]. The statistical results of LPN for LISA are shown in Figure 10, the median ASD of LPN is about 1 order lower than the displacement noise requirement of LISA [17]. However, beyond

the 3-sigma interval, the LPN noise is close to the displacement noise requirement of LISA, which indicates that the LPN noise has a serious impact on LISA under some special solar wind conditions, although the incidence of such events is not high.

Based on Lomb–Scargle spectral analysis method, and 6.5-year data of n_e , the LPN of TJ is studied, and the ASDs of the LPN is shown in Figure 11 [108]. Due to solar wind conditions of TJ is similar to LISA, the LPN of TJ [108] is similar to that of LISA [17].

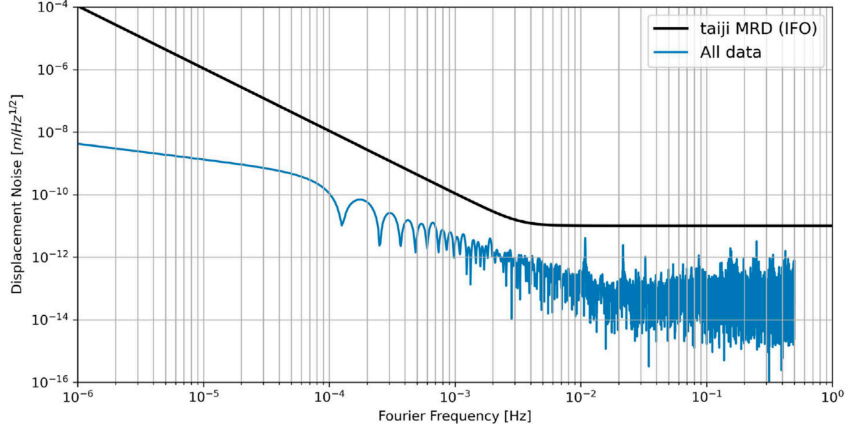


Fig. 11 The LPN’s ASDs of single link over the entire period for TJ based on the in-situ observation of Wind is represented as blue curves. The black curve is the single link sensitivity requirements of TJ. [108]

For geocentric GW detector TQ, due to the multiple structures of the Earth’s magnetosphere, which are more complex than the solar wind, it is not possible to use Equation (41) for analytical calculations, but instead requires MHD simulations. In order to assess the LPN of TQ throughout a solar cycle, the SWMF is used to simulate the plasma parameters in the vicinity of TQ’s orbit for 12 different scenarios of solar wind conditions [106]. The space weather parameters (P_{dyn} , Kp, AE, Sym-H, B_y , B_z) are different for each of these 12 events. Figure 12 shows the mean solar wind dynamic pressure \bar{P}_{dyn} over 23 years (from 1999 to 2021), \bar{P}_{dyn} of the 12 events are marked with a plus sign in Figure 12, which cover almost the entire distribution of \bar{P}_{dyn} in more than two solar cycles.

In addition, the ASD of the Michelson combination of LPN for these events is calculated, and fits the ASDs of these events by using $\text{ASD} = af^b$ to obtain the amplitude a and spectral index b [106]. The correlation coefficients of a and b of these events with solar wind parameters (P_{dyn} , Kp, AE, Sym-H, B_y , B_z) are calculated. The linear correlation coefficient between b and all solar wind parameters is found to be less than 0.4, and none of the correlations are apparent. The linear correlation coefficients of B_y and B_z with a are also less than 0.4. While the linear correlation coefficient of other parameters (P_{dyn} , Kp, AE, Sym-H) with a are $\gtrsim 0.7$, among which, the linear correlation of P_{dyn} with a is the highest, reaching about 0.9. Due to the maximum

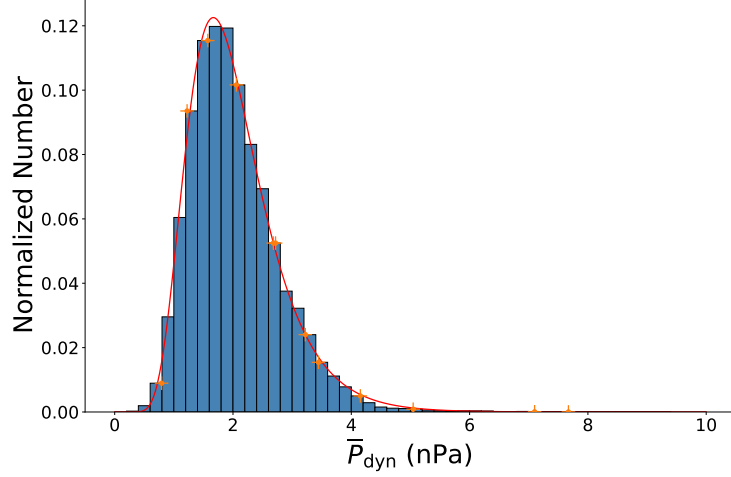


Fig. 12 Histogram of the solar wind \bar{P}_{dyn} from 1999 to 2021 [106]. The cases studied in [106] are marked as 12 orange pluses.

of the ratio of LPN to the requirement of TQ's displacement noise in the frequency domain is around 10 mHz, the ratio of LPN to requirement of TQ's displacement noise at 10 mHz is marked as R_{O10mHz} . As shown in Figure 13, the relationship between P_{dyn} and R_{O10mHz} is illustrated. Based on the linear correlation between P_{dyn} and R_{O10mHz} and the distribution of P_{dyn} over more than 2 solar cycles, the impact of LPN on TQ throughout the entire solar cycle is evaluated [106]. The occurrence rates of R_{O10mHz} exceeding 20% and 30% are approximately 40% and 15%, respectively. Overall, the impact of LPN of Michelson combination on TQ is roughly within acceptable limits, but still requires attention.

3.3 Suppression of laser propagation noise

As shown in Equation (28), the dispersion effect of EM waves propagating in space plasma can cause time delay $\Delta\tau$, which is proportional to the integration of n_e along the laser link ($\int_L n_e ds$). To deduct LPN noise, the integral of n_e along the laser link needs to be obtained.

Multiple measurements of the time τ or phase ϕ signals of multiple frequencies EM waves can obtain $\int_L n_e ds$. From Equation (28), the time moments (t_1, t_2) required for EM waves with frequencies (f_1, f_2 , and $f_1 \neq f_2$) to propagate in the same plasma background are as follows,

$$\begin{cases} \tau_1 = \frac{L}{c} + \frac{K}{2cf_1^2} N_T \\ \tau_2 = \frac{L}{c} + \frac{K}{2cf_2^2} N_T \end{cases} \quad (42)$$

here, $N_T = \int_L n_e ds$, is the total electron content (TEC). τ_1 and τ_2 can be measured, thus the difference between τ_1 and τ_2 can be derived. Therefore, N_T can also be

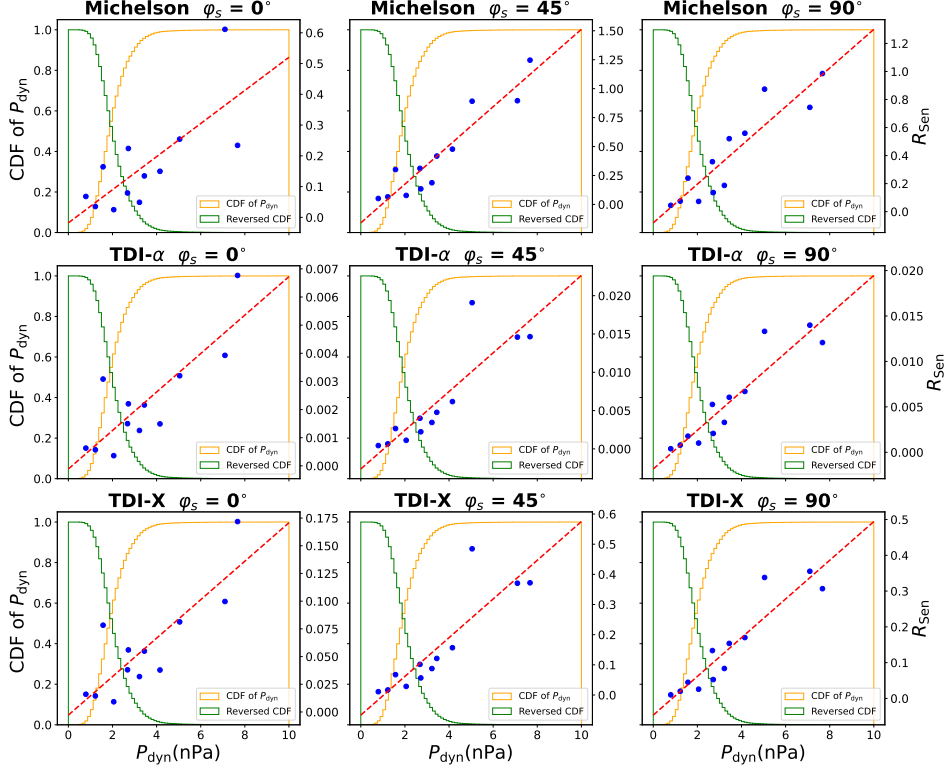


Fig. 13 The CDF and reversed CDF of \bar{P}_{dyn} , and the relationship between the amplitude of LPN's ASDs and \bar{P}_{dyn} [106].

obtained as follow,

$$N_T = \frac{2c}{K} \frac{f_1^2 f_2^2}{f_2^2 - f_1^2} (\tau_1 - \tau_2) \quad (43)$$

Thus, we can deduct the dispersion effect by differential group delay (DGD).

We can also obtain TEC from the perspective of phase. The phase variations ϕ of EM waves with frequency f after propagating a distance L is,

$$\phi = \frac{2\pi f L}{c/N} = \frac{2\pi f L}{c} \int N dl \quad (44)$$

Considering Equation (25), the phase variations ϕ_1 and ϕ_2 of EM waves with frequencies f_1 and f_2 after propagating a distance L in the same plasma background are as follows,

$$\begin{cases} \phi_1 = \frac{2\pi f_1 L}{c} + \frac{\pi K}{c f_1} N_T \\ \phi_2 = \frac{2\pi f_2 L}{c} + \frac{\pi K}{c f_2} N_T \end{cases} \quad (45)$$

Ignoring the integer ambiguity issue, N_T is as follows,

$$N_T = \frac{c}{\pi K} \frac{f_1^2 f_2^2}{f_1^2 - f_2^2} \left(\frac{\phi_1}{f_1} - \frac{\phi_2}{f_2} \right) \quad (46)$$

Since we can measure ϕ_1 and ϕ_2 , thus, we can get N_T along the laser link, and deduct the dispersion effect by differential carrier phase (DCP).

DGD can measure the absolute value of TEC, and DCP is suitable for measuring the relative variation of TEC. The methods of multiple measurements of the time (DGD) or phase (DCP) signals of EM waves of different frequencies to get N_T along the laser link are dual-frequency scheme of the dissipation for dispersion. The dual-frequency scheme and similar methods are used in fields such as ionosphere, global navigation satellite system (GNSS) and radio astronomy [109–112].

In the space-borne GW detectors, the laser frequency $f \approx 2.82 \times 10^{14}$ Hz (wavelength $\lambda \approx 1064$ nm). The difference between the sidebands of the laser and the carrier frequency are in the GHz range, thus, $\Delta f/f \sim 10^{-5}$. Taking the typical $n_e \sim 10$ cm $^{-3}$, the typical arm length $L \sim 10^5$ and 10^6 km for TQ and LISA, respectively. Thus, $N_T \sim 10^{15}$ to 10^{16} m $^{-2}$.

Taking the carrier frequency as f_1 , and sidebands frequency as f_2 . Thus, $\Delta f/f = (f_1 - f_2)/f \sim 10^{-5}$, and $f_1 \approx f_2$. According to Equation (43), the time measurement accuracy requirement for eliminating TEC by using DGD method can be estimated as follow,

$$N_T \approx \frac{c}{K} \frac{f}{\Delta f} f^2 \Delta t \quad (47)$$

here, $\Delta t = \tau_1 - \tau_2$. According to Equation (47) and the parameters above, Δt can be estimated with the value of about 10^{-28} to 10^{-27} s. Similarly, according to Equation (46), the phase measurement accuracy requirements for eliminating TEC by using DCP method can be estimated as follow,

$$N_T \approx \frac{c}{\pi K} \frac{f}{\Delta f} f \Delta \phi \quad (48)$$

here, $\Delta \phi = \phi_1 - \phi_2$. According to Equation (48) and the parameters above, $\Delta \phi$ can be estimated with the value of about 10^{-11} to 10^{-10} rad.

With current human technology, time measurement accuracy ability is far from reaching $\Delta t \approx 10^{-28}$ to 10^{-27} s, and phase measurement accuracy is far from reaching $\Delta \phi \approx 1.6 \times 10^{-10}$ to 1.6×10^{-11} rad. It indicates that using laser carrier and sideband frequencies for the DGD and DCP methods cannot eliminate the LPN noise in space-borne GW detection.

Besides dual-frequency scheme, [16] have revealed that time-delay interferometry (TDI) can suppress the OPD noise caused by laser propagation in space plasma. TDI was proposed to address the challenges of space-based gravitational wave detection, specifically the overwhelming laser frequency noise in missions like LISA [113–115]. By constructing delayed interferometric combinations of signals, TDI can effectively cancel laser frequency noise and compensating for arm length variations [116, 117]. TDI can also help mitigate other noise sources, such as clock noise, in GW detections

[118, 119]. The schematic diagrams of interferometry combination, Michelson, TDI- α , and TDI- X are shown in Figure 14 [16].

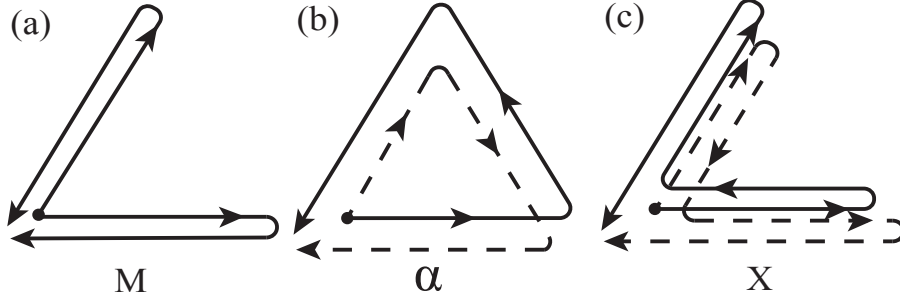


Fig. 14 The schematic of Michelson, TDI- α , and TDI- X combinations [16].

Here, denoting the phase noise cause by the laser propagation in the space plasma as,

$$s_{ij}(t) = \frac{2\pi\Delta l_{ij}(t)}{\lambda} \quad (49)$$

where, footnotes i and j denote satellites i and j , $\Delta l_{ij}(t)$ is the LPN for a single link between satellites i and j .

The distance between satellites i and j is set as L_{ij} , and set the light speed $c = 1$. For TQ, $L_{ij} = L \approx 0.6$ s, and the temporal resolution of the MHD simulation $\Delta t = 60$ s [16], $\Delta t \gg L$. It suggest that MHD simulations are unable to resolve space plasma disturbances during laser propagation here, so reasonable to approximate $\int_j^i n_e ds = \int_i^j n_e ds$. After which, for TDI- α combination, s_α is as follow [16],

$$s_\alpha = s_{12}(t - 2L) + s_{31}(t) - s_{12}(t) - s_{31}(t - 2L) \quad (50)$$

And for TDI- α combination, s_X is as follow [16],

$$s_X = s_{12}(t - 3L) + s_{12}(t - 2L) + s_{31}(t - L) + s_{31}(t) - s_{12}(t - L) - s_{12}(t) - s_{31}(t - 3L) - s_{31}(t - 2L). \quad (51)$$

Since $\Delta t \gg L \approx 0.6$ s, the time delay of s_{ij} is got by linear interpolation, $s_{ij}(t - \delta t) = s_{ij}(t) + (s_{ij}(t - \Delta t) - s_{ij}(t))(\delta t / \Delta t)$. Thus, s_α and s_X is reduced as,

$$s_\alpha = (s_{12}(t - \Delta t) - s_{12}(t))\frac{2L}{\Delta t} - (s_{31}(t - \Delta t) - s_{31}(t))\frac{2L}{\Delta t}, \quad (52)$$

$$s_X = 2s_\alpha \quad (53)$$

According to Equations (52) and (53), the LPN of TDI- α and - X combinations can be calculated. Figure 15 shows the time series results of the LPN noise for the

TDI combinations of TQ. The left and right columns are for the TDI- α and TDI- X combinations, respectively. And rows 1, 2, 3, and 4 show the results of $\varphi_s=0^\circ$, 30° , 60° , and 90° , respectively. Comparing Figures 7 and 15, it can be seen that the LPN of the TDI combinations are about 0.001 to 0.01 pm, which is 2 to 3 orders of magnitude lower than that of the Michelson combination, suggesting that TDI can significantly suppress the LPN in the time domain.

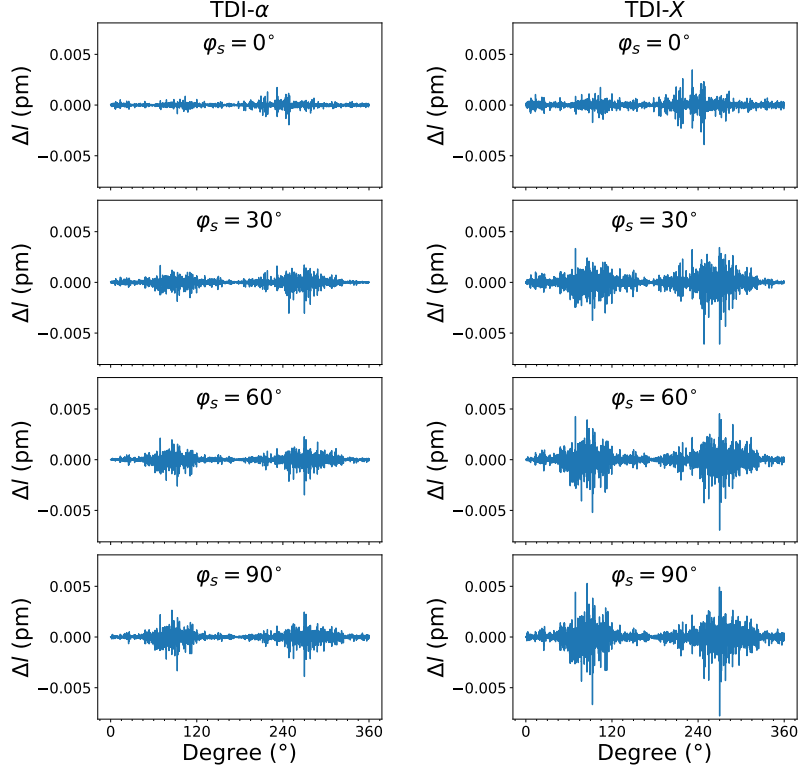


Fig. 15 The LPN's time series of TDI- α (left panels) and TDI- X (right panels) combinations for geocentric GW detectors TQ [16].

In addition, the ASD of LPN under TDI combination was calculated. Figure 16 represents the ASDs of LPN noise of the TDI combinations α and X for TQ; the left and right columns of Figure 16 are the ASDs of TDI- α and TDI- X combinations, respectively; and rows 1, 2, 3, and 4 of Figure 16 are the ASDs of $\varphi_s=0^\circ$, 30° , 60° , and 90° , respectively. Comparing the ASD of LPN for Michelson combination (Figure 8) and TDI combinations (Figure 16), it can be found that the ASDs of the TDI combinations are significantly lower than those of the Michelson combination in the low-frequency band ($\lesssim 2$ mHz); unlike the LPN of the Michelson combination, which is a colored noise with spectra indices of the ASDs about -1 to -0.5 , the ASDs

of LPN for the TDI combinations are presented as approximate white noises in the low-frequency band ($\lesssim 2$ mHz) with spectra indices ≈ 0 .

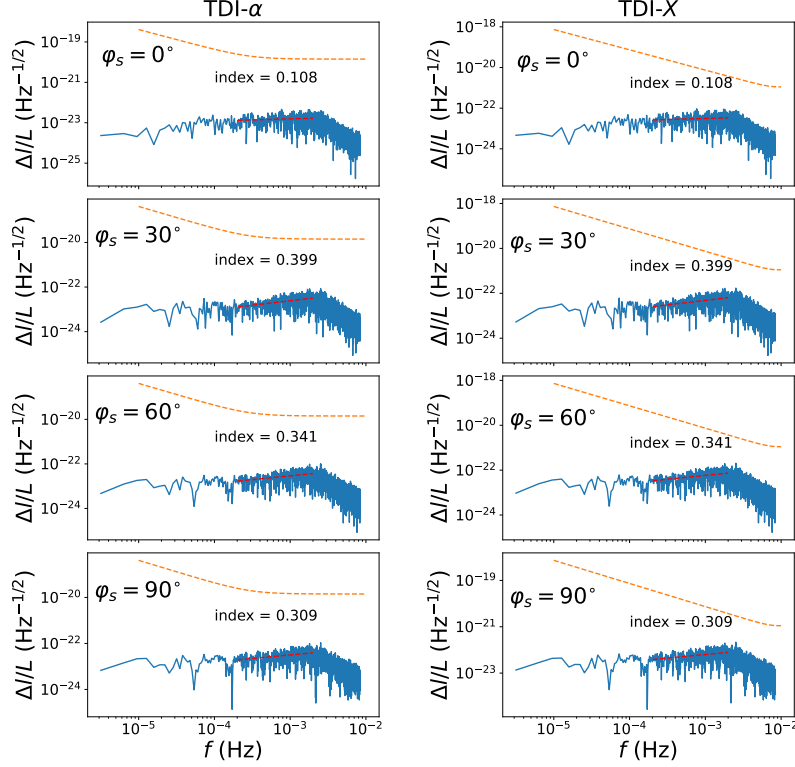


Fig. 16 The LPN's ASDs of TDI- α (left panels) and TDI- X (right panels) combinations for geocentric GW detectors TQ are represented as blue curves, and the displacement requirement of TQ is represented as orange curve [16].

For Michelson combination, the ASD of the equivalent strain noise ($\sqrt{S_n^M}$) for TQ is written as [120],

$$S_n^M = S_n^x + S_n^a \left(1 + \frac{10^4 \text{ Hz}}{f}\right) \quad (54)$$

here, f is frequency, S_n^x is the equivalent strain noise of the displacement measurement, S_n^a is the equivalent strain noise caused by acceleration noise. The ASD of equivalent strain noises for TDI- α ($\sqrt{S_n^\alpha}$) combinations is as follow [113, 114],

$$S_n^\alpha = [4\sin^2(3\pi fL/c) + 24\sin^2(\pi fL/c)]S_n^a + 6S_n^x \quad (55)$$

And for TDI- X , the ASD of equivalent strain noises is as follow [113, 114],

$$S_n^X = [4\sin^2(4\pi fL/c) + 32\sin^2(2\pi fL/c)]S_n^a + 16\sin^2(2\pi fL/c)S_n^x \quad (56)$$

In order to evaluate the LPN for Michelson, TDI- α , and TDI- X combinations, the best-fit spectra of the LPN are used to get the ratio between the equivalent strains of LPN $(\Delta l/L)$ and $\sqrt{S_n^M}$, $\sqrt{S_n^\alpha}$, $\sqrt{S_n^X}$ [16]. As shown in Figure 17, both $(\Delta l/L)/\sqrt{S_n^\alpha}$ and $(\Delta l/L)/\sqrt{S_n^X}$ are lower than $(\Delta l/L)/\sqrt{S_n^M}$, it suggests that TDI- α and - X combinations can suppress the LPN noise. The maximum of $(\Delta l/L)/\sqrt{S_n^M}$ and $(\Delta l/L)/\sqrt{S_n^X}$ are at around 10 mHz with the value of about 0.1 and 0.3, respectively [16].

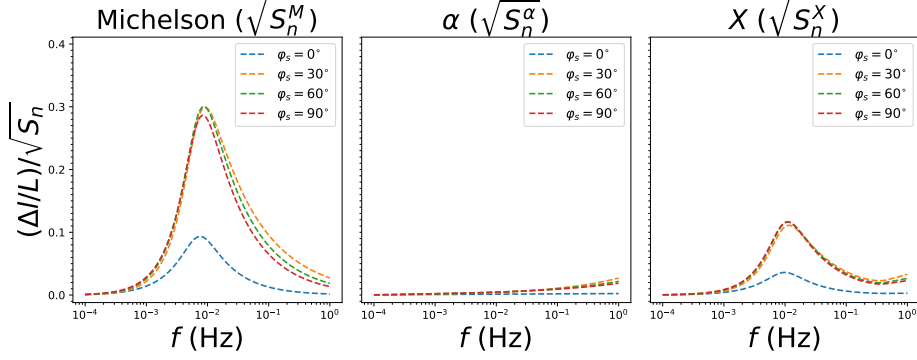


Fig. 17 The ratios of the normalization of LPN to the equivalent strain of TQ $((\Delta l/L)/\sqrt{S_n})$, the left, middle, and right panels are $(\Delta l/L)/\sqrt{S_n}$ of Michelson, TDI- α and TDI- X combinations, respectively [16].

Since TDI is revealed that can suppress the LPN, this result has been repeatedly confirmed [105, 108, 121]. Based on the high temporal and spatial resolution MHD simulations, and combining with the assumption that the perturbations of n_e follow Kolmogorov spectra, the TDI is confirmed that can suppress LPN [105]. Geometric method is applied to search TDI combinations, and 45 second-generation TDI is identified [121]; Based on the assumption of Kolmogorov spectrum, the LPN of 45 TDI combinations is evaluated by an analytical model, and find that after using TDI, if the LPN noise of LISA is required to be lower than the noise requirement, n_e needs to be $\leq 100 \text{ cm}^{-3}$ at 10 mHz [121]. The TDI combinations is also find that can suppress the LPN for TJ [108].

The LPNs of TDI combinations throughout more than a solar cycle is also studied [106]. [106] calculate the ASDs of the LPN of the TDI- α and - X combinations for 12 cases with different \bar{P}_{dyn} . Based on the fitting results of the ASDs, the values of $(\Delta l/L)/\sqrt{S_n^\alpha}$ and $(\Delta l/L)/\sqrt{S_n^X}$ at 10 mHz can be obtained, and the results are shown in the middle and bottom panels of Figure 13. The result shown that for events with $\bar{P}_{\text{dyn}} > 5 \text{ nPa}$, $(\Delta l/L)/\sqrt{S_n^X}$ can reach > 0.3 . Fortunately, according to CDF of \bar{P}_{dyn} during more than 2 solar cycles, the occurrence probability of $(\Delta l/L)/\sqrt{S_n^X} > 0.3$ is less than 1% [106]. It further demonstrates the practicality of TDI throughout the solar cycles.

From the perspective of plasma turbulence theory, TDI's ability to suppress LPN can be explained as follows. For a single arm, the distance over which plasma turbulence can propagate is the laser arm length L . The Michelson interferometric combination has two arms, and the plasma distributions along the two arms are different and can be considered uncorrelated. Thus, the typical length (S_M) that plasma disturbance can propagate for Michelson interferometric combination is L , i.e., $S_M \sim L$. The LPN distributions of single link and Michelson combination are both of the order of 1 pm, it verifies that $S_M \sim L$. According to the cascade theory of plasma turbulence, the plasma turbulence propagation velocity is the Alfvén speed v_A . Thus, the typical timescale τ_M of plasma turbulence propagate along the laser link is L/v_A . Taking the typical Alfvén velocity of the space plasma as about 300 km/s, τ_M is about 10^3 s for TQ and about 10^4 s for LISA and TJ.

TDI combinations involve two laser beams passing through the same optical path in different orders to produce interference. Thus, the two laser beams of TDI are symmetric or identical in spatial, but asymmetry or differences in temporal. The temporal asymmetry can be manifested by the time delay factor L/c in Equations (50) and (51). It indicates that the TDI combination still retains plasma turbulence on the timescale $\tau_T \approx L/c$. It means that TDI cannot suppress the LPN noise on the timescale less than L/c . For space-borne GW detections, τ_T is about 1 s for TQ, and about 10 s for LISA and TJ.

The turbulence of space plasma follows the Kolmogorov theory, with the PSD spectrum index of $-5/3$, i.e., the ASD spectrum index of $-5/6$. Thus, the ratio of the plasma turbulence magnitudes at the timescales τ_M and τ_T is as follow,

$$\frac{\delta n(\tau_M)}{\delta n(\tau_T)} = \left(\frac{1/\tau_M}{1/\tau_T} \right)^{-5/6} \approx 1000^{5/6} \quad (57)$$

Comparing LPN of Michelson and TDI combinations, the results are consistent with those in Equation (57).

Overall, the dual-frequency scheme can accurately solve the TEC along the laser link, deduct the LPN; however, the dual-frequency scheme needs to add a new frequency laser, which will increase the complexity of the system and cost of the whole space-borne GW detection. The TDI scheme can suppress the LPN without additional hardware, and is especially effective in suppressing the LPN in the low-frequency band. Considering the effectiveness of the TDI scheme throughout the solar cycles, TDI is a feasible solution.

4 Space magnetic effect for space GW detection

4.1 Space magnetic acceleration noise based on observations and MHD simulation

The effects of acceleration noise due to magnetic fields on the space-borne GW detection have been studied more than 2 decades [18, 21]. In this process, amount results on the magnetic field effects of GW detection have been accumulated, such as the measurement and manufacturing of the magnetic field properties of the TM [122–124], the

magnetic field measurement system of the GW satellite [125], and the overall magnetic effects of various instruments on the GW detectors [126]. However, these results mainly discuss the magnetic field generated by the instruments onboard the satellite [127].

For heliocentric GW detector, LISA, the acceleration noise due to space magnetic field has been measured by LISA PathFinder (LPF) [128]. LPF is a European Space Agency (ESA) mission designed to test key technologies required for the future space-based GW observatory, LISA [129]. Since magnetic forces can influence the motion of the TM, LPF carries a magnetic diagnostics subsystem with the measurement sensitivity of $10 \text{ nT Hz}^{-1/2}$ [128] to measure the magnetic field around the TMs. The magnetic field diagnostics system consists of four tri-axial fluxgate magnetometers and two coils which deployed around the TMs. The magnetic diagnostics have measured magnetic field around the TMs for hundreds of days, and the magnitude of the magnetic is on the order of 1000 nT [128]. The ASD of the magnetic field is calculated based on the time series measurements. Note that the magnetic field measured by LPF could not distinguish between the space magnetic field and the satellite magnetic field. Both ACE and LPF are located around Sun–Earth L1 point, the magnetic field observed by the ACE is pure space magnetic field, thus, the comparison of the magnetic field observation data of the ACE and LPF satellites can separate the data of the LPF satellite into the space magnetic field and the satellite magnetic field [128]. As shown in Figure 18, the results show that the magnetic field in the low-frequency band is consistent with the interplanetary magnetic field measurements of ACE. It suggests that for LPF, the magnetic field in low frequency bands ($\lesssim 1 \text{ mHz}$) is mainly caused by the interplanetary magnetic field, which is roughly presented as Kolmogorov spectrum. In the high-frequency band ($\gtrsim 1 \text{ mHz}$), the magnetic field appears as white noise with spectrum index ≈ 0 for LPF, while the magnetic field observed by ACE still appears as Kolmogorov spectrum, it indicates that the magnetic noise onboard electronic systems are white noise [128]. In addition, [128] reveal that solar wind velocity plays a significant role in driving magnetic fluctuations, during high-speed solar wind events ($\sim 500 \text{ km s}^{-1}$), the amplitude of magnetic fluctuations increases significantly compared to low-speed events ($\sim 300 \text{ km s}^{-1}$). This work is crucial for improving the design of magnetically quiet for space-based GW detectors. Recently, based on the magnetic measurements onboard the LPF, the interplanetary and spacecraft magnetic-induced acceleration noise is found to be about 0.25 and $1 \text{ fm s}^{-2} \text{ Hz}^{-1/2}$ at 1 and 0.1 mHz , respectively [130, 131].

For geocentric GW detector, TQ, there are no corresponding in-situ measurements of the space magnetic field at the altitude of TQ’s orbit, the acceleration noise due to space magnetic field is estimated based on MHD simulations [20] and semi-empirical models [89], e.g., Tsyganenko model [79].

According to Equations (39) and (40), the acceleration noise due to space magnetic field is related to the values of some TM’s physical parameters, such as the mass of TM m , the side length of the TM r , magnetic susceptibility χ_m , magnetic shielding factor ξ_m , remanent magnetic moment \mathbf{M}_r , and residual charge q . In the past decades, technology has been advancing, the values of some of these parameters have been

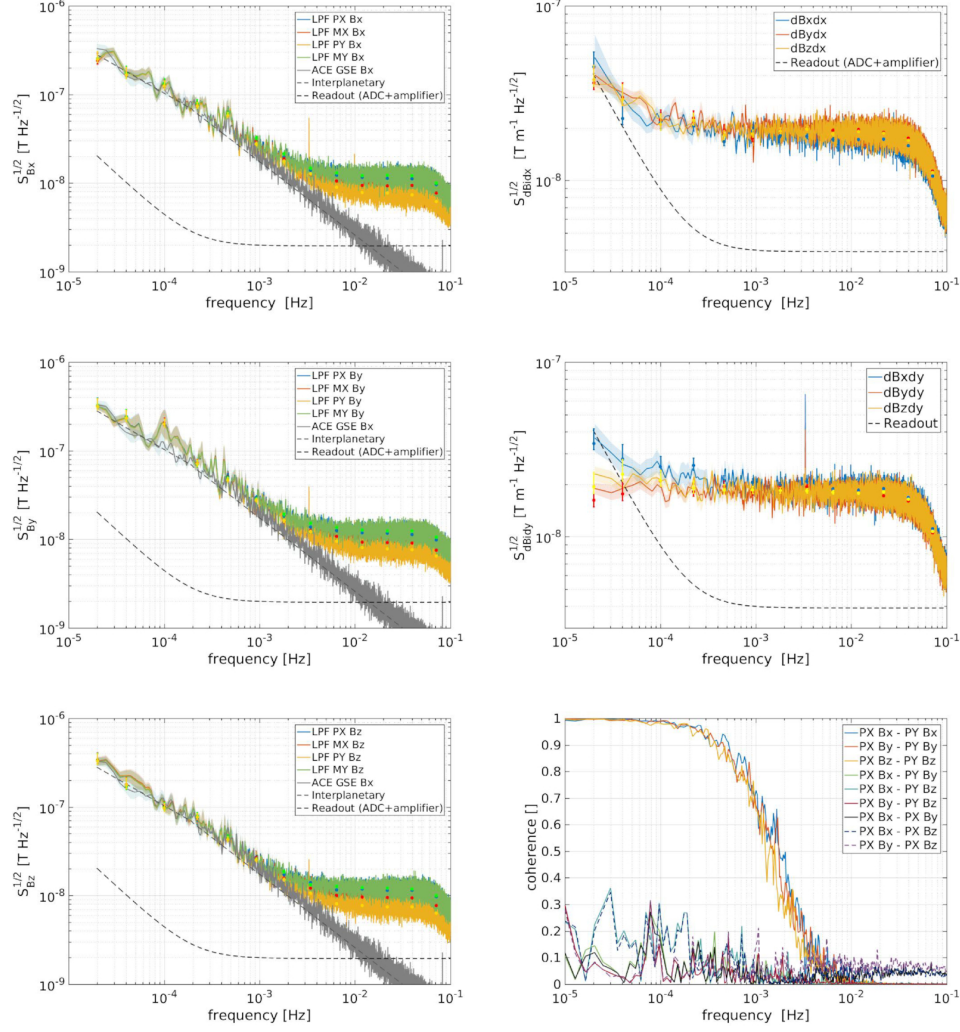


Fig. 18 The ASDs of magnetic field measured LFP and from the ACE magnetometer. The ASDs measured by 4 LFP magnetometers are represented as colored curves, and the ASDs measured by ACE is represented as grey curve [128].

iteratively updated [132–134], and the design, testing, and manufacturing of the TM has been rapidly improving in the last few years [135, 136].

In this review, the values of the physical parameters for heliocentric and geocentric GW detectors are listed in Table 4.1. The TM is made of Au–Pt alloy, the TM mass and side length are 1.96 kg and 4.6 cm for LISA [126], and 2.45 kg and 5 cm for TQ [10], respectively. The experiments show that χ_m can be less than 10^{-5} [124], and the theoretical calculations show that Au–Pt alloy with Fe or Bi impurity can even make χ_m be less than 10^{-6} [134]. Conservatively, χ_m of LISA and TQ are taken as 2.5×10^{-5} and 1×10^{-5} in this review, respectively. In the case of magnetic shielding, a_m becomes

Table 1 The list of parameters for heliocentric (LISA) and geocentric (TQ) GW detectors that used in this paper, including the mass of TM m , the side-length of TM cube r , the magnetic susceptibility χ_m , the magnetic shielding factor ξ_m , remanent magnetic moment M_r , the spacecraft magnetic field B_{sc} , and the residual charge of TM q .

	LISA	TQ
m (kg)	1.96	2.45
r (cm)	4.6	5
χ_m	2.5×10^{-5}	1×10^{-5}
ξ_m	10	10
M_r (Am ²)	2×10^{-8}	2×10^{-8}
B_{sc} (T)	1×10^{-6}	1.6×10^{-6}
q (C)	1.6×10^{-12}	1.6×10^{-12}

\mathbf{a}_m/ξ_m , which suggests that $\xi_m > 1$ can further suppress the acceleration noise due to magnetic field. ξ_m can be taken as 1 to 100 [126, 137], and in this review ξ_m of LISA and TQ are both taken as 10. For LISA, the satellite magnetic field around the TM is taken as 1.0×10^{-6} T [126]; For TQ, take equivalent magnetic moment requirement of TQ satellite as 1 A m², and the equivalent distance from the TM as 0.5 m, the satellite magnetic field around the TM is about 1.6×10^{-6} T [10, 138].

Based on the GCR observation of LPF [139–143], and modelling of GCR [144–146] for heliocentric and geocentric GW detectors, the simulation of charging of TM can be carried out, and the results show that the charging effects are comparable for heliocentric and geocentric GW detectors [147–150]. Besides GCR, occasional SEP is another important reason for the charging of the TM [151–154]. The charging of TM due to GCR and SEP makes the charge management important [155–157]. In this review the residual charge of LISA and TQ are taken to be equal with the value of 1.6×10^{-12} C. When the charged TM passes through the space magnetic field, the Lorentz force can be partially compensated by the electric field force induced by the Hall effect [59]. Here, introduce the effective shielding coefficient η , the Lorentz force \mathbf{a}_L becomes $\eta\mathbf{a}_L$. In this review, η is taken as 0.03 [59].

In addition to the density around the orbit of GW detectors, solving the MHD Equations can also yield magnetic field \mathbf{B} , bulk flow speed \mathbf{v} , electric current j , etc. So the MHD simulation can be used not only for the study of the LPN, but also for the study of the acceleration noise due to the space magnetic field. The white curves in Figure 4 are the magnetic lines of the Earth magnetosphere obtained from the MHD simulation, and the time series of the magnetic field along the TQ’s orbit during a TQ cycle is shown in Figure 19. The magnetic field around TQ’s orbit is on the order of 10 nT, in the case of a solar eruption affecting the magnetosphere or magnetic storm, the magnetic field can be larger than 100 nT [158]. The maximum of the magnetic field corresponds to the magnetosheath region, because the magnetosheath is downstream of the bow shock, and downstream of MHD shocks can enhance the magnetic field. The magnetic field in most region of the magnetosphere is larger than that of the

solar wind, and in the current sheet of the magnetotail, the magnetic field tends to approach 0 nT.

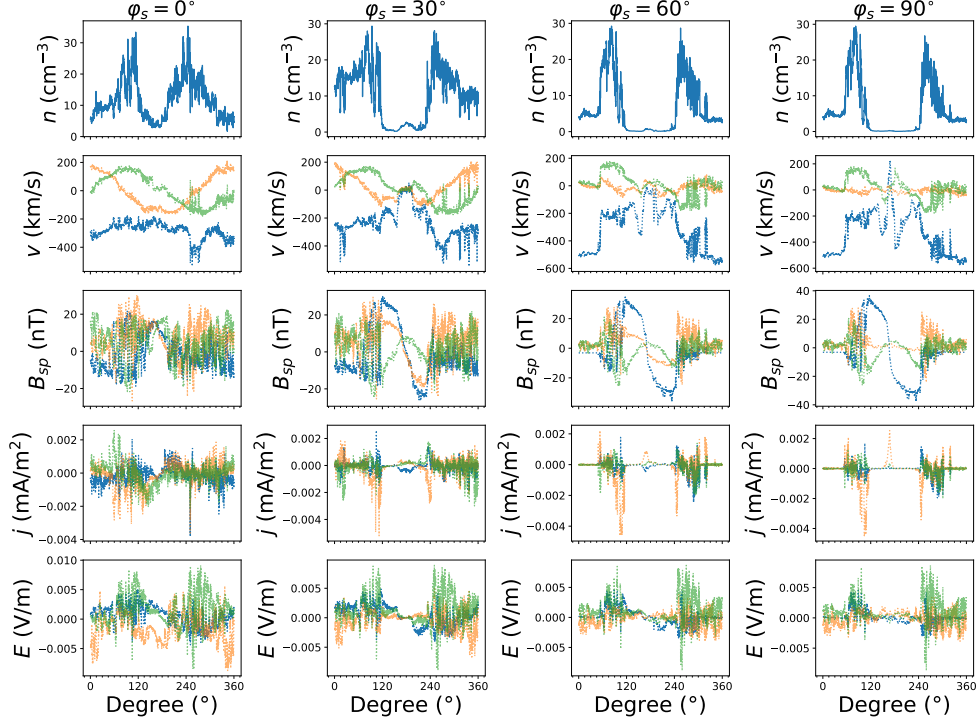


Fig. 19 The time series of physical quantities on the orbit of TQ that obtained by the MHD simulation. The first row is ion number density n_i , the second row is bulk flow \mathbf{v} , the third row is space magnetic field \mathbf{B}_{sp} , the forth row is current density \mathbf{j} , and the fifth row is the electric field \mathbf{E} [20].

Based on Equations (39) and (40), the parameters in Table 4.1, and the magnetic field on the TQ orbit obtained from the MHD simulation, the acceleration noise can be calculated. \mathbf{a}_{M1} , \mathbf{a}_{M2} , \mathbf{a}_{M3} , \mathbf{a}_{M4} , and \mathbf{a}_{M5} , are on the orders of $10^{-16} \text{ m s}^{-2}$, $10^{-20} \text{ m s}^{-2}$, $10^{-30} \text{ m s}^{-2}$, $10^{-32} \text{ m s}^{-2}$, and $10^{-23} \text{ m s}^{-2}$ [20], \mathbf{a}_{M1} is the dominant term. In addition, \mathbf{a}_L is on the order of $10^{-17} \text{ m s}^{-2}$ [20].

Since MHD simulations require extensive computational resources, using MHD to calculate the acceleration noise caused by space magnetic fields throughout an entire solar cycle would take more than hundreds of years. To quickly assess the acceleration noise caused by space magnetic fields, a faster method is needed.

4.2 Statistics result of space magnetic acceleration noise

The Tsyganenko model is a data-driven empirical model that can yield the space magnetic field in and around the Earth's magnetosphere. Figure 20 shows a schematic

diagram of space magnetic field on the TQ orbital plane that calculated by the TS model, where the grey curves are the magnetic lines calculated by Tsyganenko model, and the red circle is the orbit of TQ. Compared to the MHD simulation, it can calculate the space magnetic field much faster, and it is suitable for statistical analysis of acceleration noise due to space magnetic field for geocentric GW detectors.

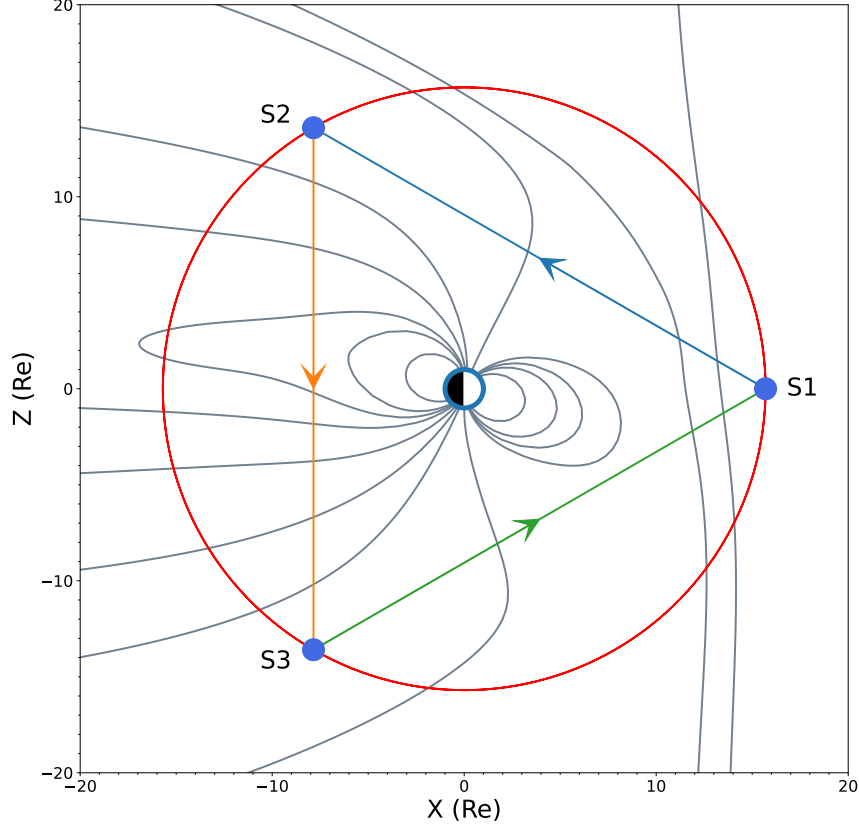


Fig. 20 The space magnetic field around the orbit of TQ that obtained by Tsyganenko model [89].

Using 23 years (more than 2 solar cycles) of OMNI solar wind data from 1998-01-01 to 2020-12-31 as input, the Tsyganenko model was applied to calculate the space magnetic field of 2300 TQ orbital cycles over 23 years [89]. Based on the Tsyganenko model, and Equations (39) and (40), the space magnetic acceleration noise of a total of TQ orbital cycles is obtained [89]. As \mathbf{a}_{M1} is the dominant term, \mathbf{a}_{M1} is denoted by \mathbf{a}_M in the following, and the total space magnetic field acceleration is denoted as $\mathbf{A} = \sqrt{\mathbf{a}_M^2 + \mathbf{a}_L^2}$. In this review, the ASDs of \mathbf{a}_M and \mathbf{a}_L within the 2500 TQ orbital cycles (from 1998-01-01 to 2022-12-31) are updated [159], and the results are shown in Figure 21 [89, 159]. The left, middle, and right panels of Figure 21 are the ASDs of \mathbf{a}_M , \mathbf{a}_L , and \mathbf{A} for TQ, respectively. The median of the 2500 ASDs is represented as

dotted blue curves. The orange, purple, and brown shadows represent 1- σ , 2- σ , and 3- σ intervals of ASDs, respectively. And the requirement of acceleration noise for TQ, $\sqrt{S_{a-TQ}}$, is the orange dashed line, which is updated as follow [160],

$$\sqrt{S_{a-TQ}} = 1 \times \sqrt{1 + \left(\frac{f_{c1}}{f}\right)^2} \sqrt{1 + \left(\frac{f}{f_{c2}}\right)^4} \text{ fm}/(\text{s}^2 \cdot \text{Hz}^{1/2}) \quad (58)$$

here, f_{c1} and f_{c2} are transfer frequencies with the value of 0.1 and 14 mHz. The mean value of a_M , a_L , and A at 1 mHz for TQ are $(1.410 \pm 0.621) \times 10^{-17}$, $(6.203 \pm 2.447) \times 10^{-19}$ and $(1.412 \pm 0.621) \times 10^{-17} \text{ m s}^2$, respectively. The spectra indices of the ASDs for a_M , a_L , and A are about -0.5 to -1 , indicating that the acceleration noise due to space magnetic field is color noise, and that the amplitude of the space magnetic noise decreases with increasing frequency.

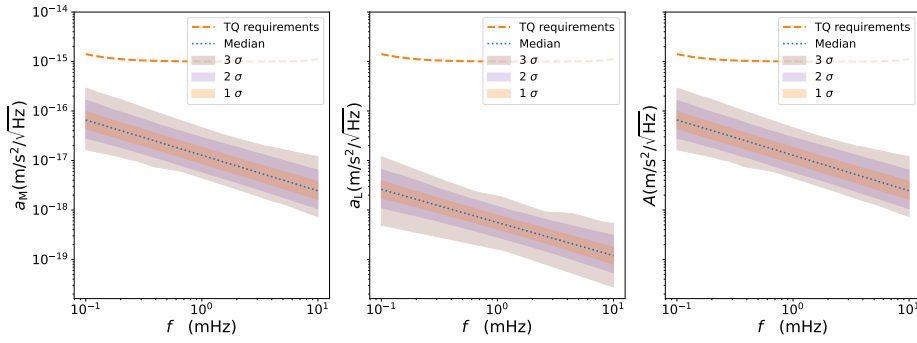


Fig. 21 The ASDs of a_m , a_L , and A for TQ [159]. The orange curve is the acceleration requirement of TQ.

As Tsyganenko model does not contain the magnetosheath region, a hybrid modeling approach that combines the Tsyganenko-Sitnov (TS05) [82] model with the Romashets-Vandas (RV) model [161, 162] to improve accuracy in simulating the magnetic field along TQ's orbit [163]. Based on the hybrid model, a careful study of the space magnetic acceleration noise in the regions such as magnetopause, magnetotail, magnetosheath, and transregion and solar wind is investigated. The results show that the transregion with abrupt magnetic field changes has the highest acceleration noise, the magnetosheath with strong turbulence has the middle acceleration noise, and the magnetotail with a more stable fluctuation has the lowest acceleration noise [163]. And the solar wind fluctuations can significantly increase the space magnetic field acceleration noise [163].

According to the ASDs of space magnetic field acceleration noise of TQ over 2 solar activity cycles, the ratio between the ASDs of space magnetic field acceleration noise and the acceleration requirement of TQ ($A/\sqrt{S_{a-TQ}}$) is calculated. And the cumulative distribution function (CDF) and reversed CDF $A/\sqrt{S_{a-TQ}}$ at the frequencies of 0.1, 1, and 14 mHz are obtained and shown in Figure 22. The results show that the

occurrence probability of space magnetic field acceleration exceeding the TQ's requirement by 10% at 0.1 mHz is 4.70%, that exceeding the TQ's requirement by 10% at 1 mHz and 14 mHz does not occur, and that the probability of exceeding the TQ's requirement by 2% at 1 mHz is 0.13%. It suggests that the TQ's space magnetic acceleration noise in the low frequency band ($\lesssim 1$ mHz) needs to be taken into account for TQ, and that in the high frequency band ($\gtrsim 1$ mHz) of the system are not important.

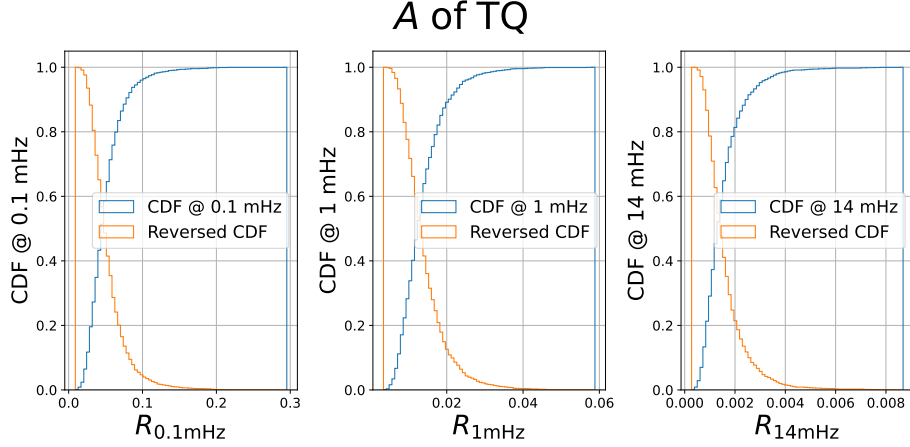


Fig. 22 The CDF and reversed CDF of \mathbf{A} for TQ at 0.1, 1, and 14 mHz [159].

According to LISA's orbit, the LISA satellites are fully immersed in the solar wind and are approximately 1 AU from the Sun. Thus, the space magnetic field around the orbit of LISA can be considered similar to that at the Sun-Earth L1 point. Here, the OMNI dataset, which is based on in-situ solar wind observations at L1, is used to obtain space magnetic field data over 25 years from 1998-01-01 to 2022-12-31 (more than 2 solar cycles). Using the space magnetic field data from OMNI, and Equations (39) and (40), the space magnetic acceleration noise \mathbf{a}_M and \mathbf{a}_L for LISA over these 9000+ days are calculated. And the ASDs of \mathbf{a}_M and \mathbf{a}_L within 9000+ days for LISA are calculated, and the results are shown in Figure 23. The left, middle, and right panels of Figure 23 are the ASDs of \mathbf{a}_M , \mathbf{a}_L , and \mathbf{A} for LISA, respectively. The shadows and curves in Figure 23 represent the same meaning as in Figure 21. The LISA's acceleration noise requirement curve in Figure 21 is as follow [7],

$$S_a^{1/2} \leq 3 \times 10^{-15} \frac{\text{ms}^{-2}}{\sqrt{\text{Hz}}} \cdot \sqrt{1 + \left(\frac{0.4\text{mHz}}{f}\right)^2} \cdot \sqrt{1 + \left(\frac{f}{8\text{mHz}}\right)^4} \quad (59)$$

The median of a_M , a_L , and A at 1 mHz for LISA are 9.686×10^{-18} , 6.560×10^{-18} and 1.208×10^{-17} m s², respectively. Similarly to TQ, the spectra indices of the ASDs of the space magnetic accelerations are color noise for LISA, and the amplitude of the space magnetic noise decreases with increasing frequency. This is because the magnetic

field in different regions of the heliosphere, such as the earth magnetosphere and the solar wind, follow the same self-similarity [164].

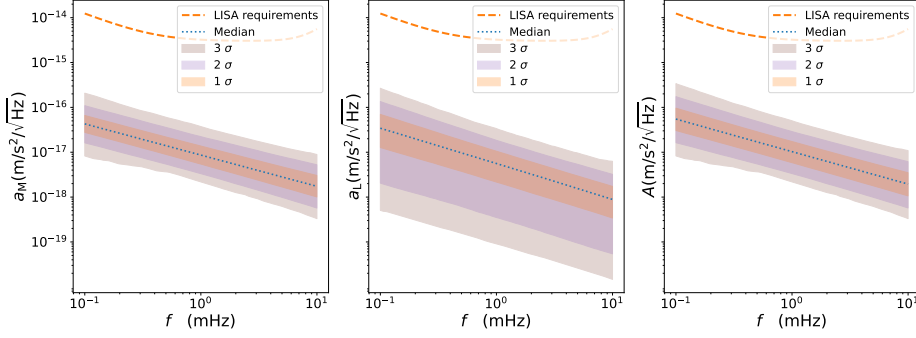


Fig. 23 The ASDs of a_m , a_L , and A for TQ [159]. The orange curve is the acceleration requirement of LISA.

Similarly the ratio between the ASDs of space magnetic field acceleration noise and the acceleration requirement of LISA ($A/\sqrt{S_{a-LISA}}$) is calculated [159]. And according to the ASDs of space magnetic field acceleration for LISA over 2 solar cycles, the CDFs and reversed CDFs $A/\sqrt{S_{a-LISA}}$ at 0.4, 1, and 8 mHz are calculated, and the results are shown in Figure 24. The occurrence probability of space magnetic field acceleration exceeding the LISA's requirement by 10% does not occur, that exceeding the LISA's requirement by 1% at 0.4 mHz and 1 mHz are 2.35% and 0.27%, respectively, and that the probability of exceeding the TQ requirement by 1% at 8 mHz does not occur. It suggests that the space magnetic environment of LISA is better than that of TQ.

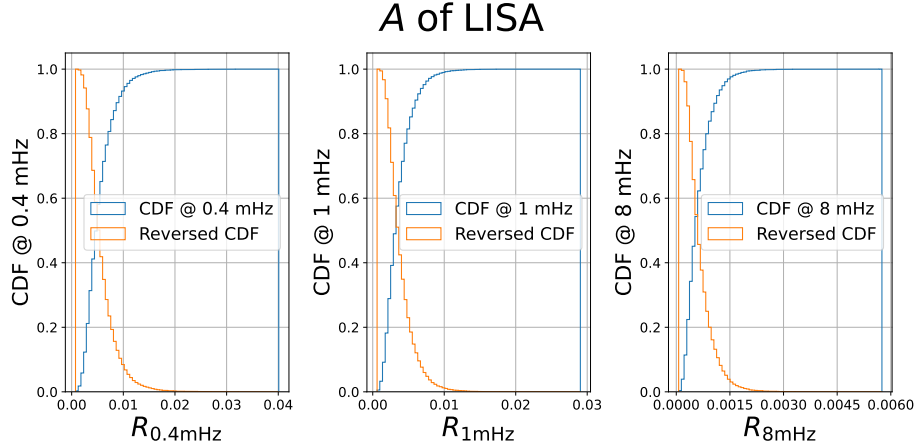


Fig. 24 The CDF and reversed CDF of A for LISA at 0.4, 1, and 8 mHz [159].

Based on the statistical study of space magnetic acceleration noise over 2 solar cycles for LISA and TQ, the design parameters of the TM can be provided. As shown in Figure 25, the left and right panels are χ_m - ξ_m design spaces for LISA and TQ, respectively. The results show that TQ has more stringent requirements of χ_m - ξ_m than that of LISA. This is due to the fact that the acceleration noise requirement of TQ are more stringent than that of LISA, and that the magnetic field in the Earth's magnetosphere is stronger than that in the solar wind. Even so, with the current technical, the space magnetic acceleration noise of TQ ($A/\sqrt{S_{a-TQ}} \lesssim 10\%$) is lower than the total magnetic acceleration noise budget ($A/\sqrt{S_{a-TQ}} \leq 24\%$). Considering that the launch time of GW detectors at about 2035 is still a decade away, the acceleration noise due to the space magnetic field can be expected reduced to much less than 10% of the total acceleration noise budget in 2035 for both LISA and TQ.

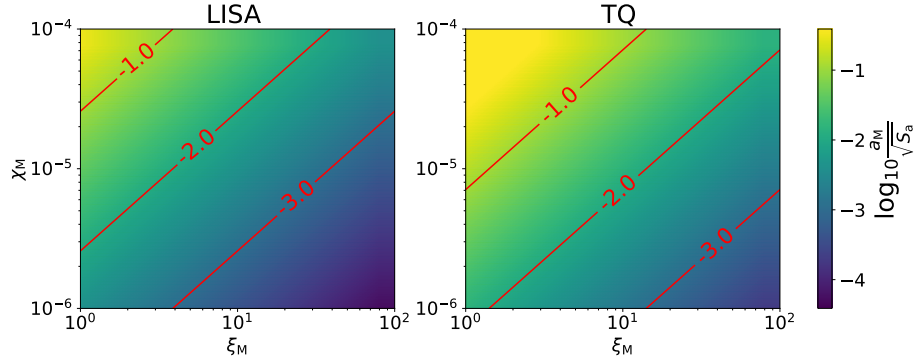


Fig. 25 The left and right panels are the space of χ_m - ξ_m at 1 mHz for LISA and TQ, respectively. $a_m/\sqrt{S_a}$ is represented as the color-bar. The contours lines of -1, -2, and -3 are the contours of $a_m/\sqrt{S_a} = 10^{-1}$, 10^{-1} , and 10^{-1} , respectively [159].

5 Discussion

For laser propagation noise, studies on both heliocentric and geocentric GW detection suggest that LPN do not exceed the respective displacement noise requirements. The study of LPN for heliocentric GW detection is based on in-situ observations, while the LPN for geocentric one is derived from MHD simulations. The advantage of using in-situ observation of n_e lies in its high reliability. But the limitation is the lack of spatial resolution. The theories that derive the spatial distribution of n_e along the laser link from in-situ data require validation through observations or numerical simulations.

Comparing with local observations, LPN studies based on MHD simulations can obtain the spatial distribution along the laser link. However, the discrepancy between MHD simulations and real observations makes the distribution of n_e obtained by MHD are only approximate. Additionally, MHD simulations require enormous computational resources, making it infeasible to simulate LPN evolution over an entire solar cycle

with current computational capabilities. A compromise is to study LPN noise under different space weather parameters and find the linear correlation between the space weather parameters and LPN, then estimate of LPN throughout the solar cycle. This method introduces errors. Furthermore, the temporal resolution of MHD simulations for LPN studies is 60 s, much larger than 1 s, meaning the frequency ($\gtrsim 0.01$ Hz) do not cover the high-frequency band of space-borne GW detection. Current estimations assume that n_e follows the same spectra index in the high-frequency range, the in-situ observation around the space-borne GW detectors can further validate the spectra index in the high-frequency range. Regarding spatial resolution, since GW detection satellites travel at speeds of the order of 10 km/s, the finest spatial resolution is required to be about 10 km ($10 \text{ km s}^{-1}/1 \text{ Hz}$). However, the spatial resolution of the existing MHD simulations is still 2 orders of magnitude short of the demand. Future research needs higher temporal and spatial resolution MHD simulations to improve the LPN studies.

Due to the influence of magnetic fields, anisotropy is one of the fundamental differences between plasma and fluid [165]. Until now, in studies of the effects of space plasma and magnetic fields on space-borne GW detection, the anisotropy is neglected, the effects caused by anisotropy are worth further investigation. The impact of anisotropy needs to be considered in future work for heliocentric and geocentric GW detection. Both the dual-frequency scheme and the time delay interferometry scheme can suppress LPN. The dual-frequency scheme increases the complexity of the GW detection system, while the TDI scheme does not require additional hardware, making it more cost-effective [166]. But the TDI is not as effective in suppressing the noise at high frequency band as it is at low frequency band. The final choice between these two schemes requires further discussion.

For acceleration noise caused by space magnetic fields, current results indicate that both heliocentric and geocentric orbit GW detectors meet their respective acceleration noise requirements. The acceleration noise performance of heliocentric GW detectors is better than that of geocentric ones. The difference arises from the different space environments around the orbits. Heliocentric GW detectors are fully immersed in the solar wind, whereas geocentric GW detectors are primarily within Earth's magnetosphere. Roughly, the solar wind is dominated by plasma dynamic pressure, while the Earth's magnetosphere is dominated by magnetic pressure [41]. Consequently, the magnetic field in the solar wind is weaker than that in the magnetosphere [167]. It results in TQ having a more stringent parameters (χ_m - ξ_m) design requirements compared to LISA. Additionally, the space magnetic acceleration noise analysis for geocentric GW detectors is based on empirical and MHD models, and further validation through observation-based studies is necessary.

6 Conclusion

Laser propagation effects in the space plasma and acceleration noise due to space magnetic fields are critical challenges in space-based GW detections. The optical path noise induced by laser propagation in space plasma is only about one order of magnitude below the displacement requirement of GW detectors, and it can fully consume the

noise budget during strong solar eruptions. The dual-frequency scheme can deduct the LPN. And TDI can suppress the LPN in low frequency band ($\lesssim 10$ mHz) effectively without adding a new laser beam with different frequency. Acceleration noise due to space magnetic fields is about 1–2 orders of magnitude below the acceleration requirement for GW detections. Note that the result depends on specific satellite parameters such as χ_m and ξ_m , the design of the TM's parameters space can be constrained based on space magnetic field acceleration noise analysis. Both LPN and acceleration noise studies are based on models and assumptions, such as the Kolmogorov spectrum of space electron number density n_e , Tsyanenko models, and MHD simulations of SWMF. Due to model limitations, some results, such as the occurrence rate of LPN over solar cycles, remain estimation. Current findings require further validation through space satellites observations, and more detailed studies on LPN and acceleration noise are needed.

Acknowledgements. S.W. is supported by the National Key R&D Program of China (No. 2020YFC2201200), NSFC (grant No. 12473060 and 122261131504).

Declarations

Conflict of interest. The author declares no conflict of interest.

References

- [1] Abbott, B.P., Abbott, R., Abbott, T.D., Abernathy, M.R., Acernese, F., Ackley, K., Adams, C., Adams, T., Addesso, P., Adhikari, R.X., al.: Observation of Gravitational Waves from a Binary Black Hole Merger. *Physical Review Letters* **116**(6), 061102 (2016) <https://doi.org/10.1103/PhysRevLett.116.061102> [arXiv:1602.03837](https://arxiv.org/abs/1602.03837) [gr-qc]
- [2] Abbott, B.P., Abbott, R., Abbott, T.D., Acernese, F., Ackley, K., Adams, C., Adams, T., Addesso, P., Adhikari, R.X., Adya, V.B., al.: GW170817: Observation of Gravitational Waves from a Binary Neutron Star Inspiral. *Physical Review Letters* **119**(16), 161101 (2017) <https://doi.org/10.1103/PhysRevLett.119.161101> [arXiv:1710.05832](https://arxiv.org/abs/1710.05832) [gr-qc]
- [3] Hu, L., Wu, X., Andreoni, I., Ashley, M.C.B., Cooke, J., Cui, X., Du, F., Dai, Z., Gu, B., Hu, Y., Lu, H., Li, X., Li, Z., Liang, E., Liu, L., Ma, B., Shang, Z., Sun, T., Suntzeff, N.B., Tao, C., Udden, S.A., Wang, L., Wang, X., Wen, H., Xiao, D., Su, J., Yang, J., Yang, S., Yuan, X., Zhou, H., Zhang, H., Zhou, J., Zhu, Z.: Optical observations of LIGO source GW 170817 by the Antarctic Survey Telescopes at Dome A, Antarctica. *Science Bulletin* **62**, 1433–1438 (2017) <https://doi.org/10.1016/j.scib.2017.10.006> [arXiv:1710.05462](https://arxiv.org/abs/1710.05462) [astro-ph.HE]
- [4] Nitz, A.H., Capano, C., Nielsen, A.B., Reyes, S., White, R., Brown, D.A., Krishnan, B.: 1-OGC: The First Open Gravitational-wave Catalog of Binary

- [5] Abbott, B.P., Abbott, R., Abbott, T.D., Abraham, S., Acernese, F., Ackley, K., Adams, C., Adhikari, R.X., Adya, V.B., Affeldt, C., Agathos, M., Agatsuma, K., Aggarwal, N., Aguiar, O.D., Aiello, L., Ain, A., Ajith, P., Allen, G., Allocca, A., Aloy, M.A., Altin, P.A., Amato, A., Ananyeva, A., Anderson, S.B., Anderson, W.G., Angelova, S.V., Antier, S., Appert, S., Arai, K., Araya, M.C., Areeda, J.S., Arène, M., Arnaud, N., Arun, K.G., Ascenzi, S., Ashton, G., Aston, S.M., Astone, P., Aubin, F., Aufmuth, P., AultONeal, K., Austin, C., Avendano, V., Avila-Alvarez, A., Babak, S., Bacon, P., Badaracco, F., Bader, M.K.M., Bae, S., Baker, P.T., Baldaccini, F., Ballardin, G., Ballmer, S.W., Banagiri, S., Barayoga, J.C., Barclay, S.E., Barish, B.C., Barker, D., Barkett, K., Barnum, S., Barone, F., Barr, B., Barsotti, L., Barsuglia, M., Barta, D., Bartlett, J., Bartos, I., Bassiri, R., Basti, A., Bawaj, M., Bayley, J.C., Bazzan, M., Bécsy, B., Bejger, M., Belahcene, I., Bell, A.S., Beniwal, D., Berger, B.K., Bergmann, G., Bernuzzi, S., Bero, J.J., Berry, C.P.L., Bersanetti, D., Bertolini, A., Betzwieser, J., Bhandare, R., Bidler, J., Bilenko, I.A., Bilgili, S.A., Billingsley, G., Birch, J., Birney, R., Birnholtz, O., Biscans, S., Biscoveanu, S., Bisht, A., Bitossi, M., Bizouard, M.A., Blackburn, J.K., Blackman, J., Blair, C.D., Blair, D.G., Blair, R.M., Bloemen, S., Bode, N., Boer, M., Boetzel, Y., Bogaert, G., Bondu, F., Bonilla, E., Bonnand, R., Booker, P., Boom, B.A., Booth, C.D., Bork, R., Boschi, V., Bose, S., Bossie, K., Bossilkov, V., Bosveld, J., Bouffanais, Y., Bozzi, A., Bradaschia, C., Brady, P.R., Bramley, A., Branchesi, M., Brau, J.E., Briant, T., Briggs, J.H., Brighenti, F., Brillet, A., Brinkmann, M., Brisson, V., Brockill, P., Brooks, A.F., Brown, D.D., Brunett, S., Buikema, A., Bulik, T., Bulten, H.J., Buonanno, A., Buskulic, D., Bustamante Rosell, M.J., Buy, C., Byer, R.L., Cabero, M., Cadenati, L., Cagnoli, G., Cahillane, C., Calderón Bustillo, J., Callister, T.A., Calloni, E., Camp, J.B., Campbell, W.A., Canepa, M., Cannon, K.C., Cao, H., Cao, J., Capocasa, E., Carbognani, F., Caride, S., Carney, M.F., Carullo, G., Casanueva Diaz, J., Casentini, C., Caudill, S., Cavaglià, M., Cavalier, F., Cavalieri, R., Cella, G., Cerdá-Durán, P., Cerretani, G., Cesarini, E., Chaibi, O., Chakravarti, K., Chamberlin, S.J., Chan, M., Chao, S., Charlton, P., Chase, E.A., Chassande-Mottin, E., Chatterjee, D., Chaturvedi, M., Chatziioannou, K., Cheeseboro, B.D., Chen, H.Y., Chen, X., Chen, Y., Cheng, H.-P., Cheong, C.K., Chia, H.Y., Chincarini, A., Chiummo, A., Cho, G., Cho, H.S., Cho, M., Christensen, N., Chu, Q., Chua, S., Chung, K.W.: GWTC-1: A Gravitational-Wave Transient Catalog of Compact Binary Mergers Observed by LIGO and Virgo during the First and Second Observing Runs. *Physical Review X* **9**(3), 031040 (2019) <https://doi.org/10.1103/PhysRevX.9.031040> [arXiv:1811.12907](https://arxiv.org/abs/1811.12907) [astro-ph.HE]
- [6] Bailes, M., Berger, B.K., Brady, P.R., Branchesi, M., Danzmann, K., Evans, M., Holley-Bockelmann, K., Iyer, B.R., Kajita, T., Katsanevas, S., Kramer, M., Lazzarini, A., Lehner, L., Losurdo, G., Lück, H., McClelland, D.E., McLaughlin, M.A., Punturo, M., Ransom, S., Raychaudhury, S., Reitze, D.H., Ricci, F.,

- Rowan, S., Saito, Y., Sanders, G.H., Sathyaprakash, B.S., Schutz, B.F., Sesana, A., Shinkai, H., Siemens, X., Shoemaker, D.H., Thorpe, J., van den Brand, J.F.J., Vitale, S.: Gravitational-wave physics and astronomy in the 2020s and 2030s. *Nature Reviews Physics* **3**(5), 344–366 (2021) <https://doi.org/10.1038/s42254-021-00303-8>
- [7] Amaro-Seoane, P., Audley, H., Babak, S., Baker, J., Barausse, E., Bender, P., Berti, E., Binetruy, P., Born, M., Bortoluzzi, D., Camp, J., Caprini, C., Cardoso, V., Colpi, M., Conklin, J., Cornish, N., Cutler, C., Danzmann, K., Dolesi, R., Ferraioli, L., Ferroni, V., Fitzsimons, E., Gair, J., Gesa Bote, L., Giardini, D., Gibert, F., Grimaldi, C., Hallin, H., Heinzel, G., Hertog, T., Hewitson, M., Holley-Bockelmann, K., Hollington, D., Hueller, M., Inchauspe, H., Jetzer, P., Karnesis, N., Killow, C., Klein, A., Klipstein, B., Korsakova, N., Larson, S.L., Livas, J., Lloro, I., Man, N., Mance, D., Martino, J., Mateos, I., McKenzie, K., McWilliams, S.T., Miller, C., Mueller, G., Nardini, G., Nelemans, G., Nofrarias, M., Petiteau, A., Pivato, P., Plagnol, E., Porter, E., Reiche, J., Robertson, D., Robertson, N., Rossi, E., Russano, G., Schutz, B., Sesana, A., Shoemaker, D., Slutsky, J., Sopuerta, C.F., Sumner, T., Tamanini, N., Thorpe, I., Troebs, M., Vallisneri, M., Vecchio, A., Vetrugno, D., Vitale, S., Volonteri, M., Wanner, G., Ward, H., Wass, P., Weber, W., Ziemer, J., Zweifel, P.: Laser Interferometer Space Antenna. arXiv e-prints (2017) [arXiv:1702.00786](https://arxiv.org/abs/1702.00786) [astro-ph.IM]
- [8] Kawamura, S., Ando, M., Seto, N., Sato, S., Nakamura, T., Tsubono, K., Kanda, N., Tanaka, T., Yokoyama, J., Funaki, I., Numata, K., Ioka, K., Takashima, T., Agatsuma, K., Akutsu, T., Aoyanagi, K.-s., Arai, K., Araya, A., Asada, H., Aso, Y., Chen, D., Chiba, T., Ebisuzaki, T., Ejiri, Y., Enoki, M., Eriguchi, Y., Fujimoto, M.-K., Fujita, R., Fukushima, M., Futamase, T., Harada, T., Hashimoto, T., Hayama, K., Hikida, W., Himemoto, Y., Hirabayashi, H., Hiramatsu, T., Hong, F.-L., Horisawa, H., Hosokawa, M., Ichiki, K., Ikegami, T., Inoue, K.T., Ishidoshiro, K., Ishihara, H., Ishikawa, T., Ishizaki, H., Ito, H., Itoh, Y., Izumi, K., Kawano, I., Kawashima, N., Kawazoe, F., Kishimoto, N., Kiuchi, K., Kobayashi, S., Kohri, K., Koizumi, H., Kojima, Y., Kokeyama, K., Kokuyama, W., Kotake, K., Kozai, Y., Kunitori, H., Kuninaka, H., Kuroda, K., Kuroyanagi, S., Maeda, K.-i., Matsuhara, H., Matsumoto, N., Michimura, Y., Miyakawa, O., Miyamoto, U., Miyoki, S., Morimoto, M.Y., Morisawa, T., Moriwaki, S., Mukohyama, S., Musha, M., Nagano, S., Naito, I., Nakamura, K., Nakano, H., Nakao, K., Nakasuka, S., Nakayama, Y., Nakazawa, K., Nishida, E., Nishiyama, K., Nishizawa, A., Niwa, Y., Noumi, T., Obuchi, Y., Ohashi, M., Ohishi, N., Ohkawa, M., Okada, K., Okada, N., Oohara, K., Sago, N., Saijo, M., Saito, R., Sakagami, M., Sakai, S.-i., Sakata, S., Sasaki, M., Sato, T., Shibata, M., Shinkai, H., Shoda, A., Somiya, K., Sotani, H., Sugiyama, N., Suwa, Y., Suzuki, R., Tagoshi, H., Takahashi, F., Takahashi, K., Takahashi, K., Takahashi, R., Takahashi, R., Takahashi, T., Takahashi, H., Akiteru, T., Takano, T., Tanaka, N., Taniguchi, K., Taruya, A., Tashiro, H., Torii, Y., Toyoshima, M., Tsujikawa, S., Tsunesada, Y., Ueda, A., Ueda, K.-i., Utashima, M., Wakabayashi, Y., Yagi, K., Yamakawa, H., Yamamoto, K., Yamazaki, T., Yoo,

- C.-M., Yoshida, S., Yoshino, T., Sun, K.-X.: The Japanese space gravitational wave antenna: DECIGO. *Classical and Quantum Gravity* **28**(9), 094011 (2011) <https://doi.org/10.1088/0264-9381/28/9/094011>
- [9] Hu, W.-R., Wu, Y.-L.: The taiji program in space for gravitational wave physics and the nature of gravity. *National Science Review* **4**(5), 685–686 (2017) <https://doi.org/10.1093/nsr/nwx116> <https://academic.oup.com/nsr/article-pdf/4/5/685/31566708/nwx116.pdf>
- [10] Luo, J., Chen, L.-S., Duan, H.-Z., Gong, Y.-G., Hu, S., Ji, J., Liu, Q., Mei, J., Milyukov, V., Sazhin, M., Shao, C.-G., Toth, V.T., Tu, H.-B., Wang, Y., Wang, Y., Yeh, H.-C., Zhan, M.-S., Zhang, Y., Zharov, V., Zhou, Z.-B.: TianQin: a space-borne gravitational wave detector. *Classical and Quantum Gravity* **33**(3), 035010 (2016) <https://doi.org/10.1088/0264-9381/33/3/035010> [arXiv:1512.02076](https://arxiv.org/abs/1512.02076) [astro-ph.IM]
- [11] Luo, Z., Wang, Y., Wu, Y., Hu, W., Jin, G.: The Taiji program: A concise overview. *Progress of Theoretical and Experimental Physics* **2021**(5), 05–108 (2021) <https://doi.org/10.1093/ptep/ptaa083>
- [12] Mei, J., Bai, Y.-Z., Bao, J., Barausse, E., Cai, L., Canuto, E., Cao, B., Chen, W.-M., Chen, Y., Ding, Y.-W., Duan, H.-Z., Fan, H., Feng, W.-F., Fu, H., Gao, Q., Gao, T., Gong, Y., Gou, X., Gu, C.-Z., Gu, D.-F., He, Z.-Q., Hendry, M., Hong, W., Hu, X.-C., Hu, Y.-M., Hu, Y., Huang, S.-J., Huang, X.-Q., Jiang, Q., Jiang, Y.-Z., Jiang, Y., Jiang, Z., Jin, H.-M., Korol, V., Li, H.-Y., Li, M., Li, M., Li, P., Li, R., Li, Y., Li, Z., Li, Z., Li, Z.-X., Liang, Y.-R., Liang, Z.-C., Liao, F.-J., Liu, Q., Liu, S., Liu, Y.-C., Liu, L., Liu, P.-B., Liu, X., Liu, Y., Lu, X.-F., Lu, Y., Lu, Z.-H., Luo, Y., Luo, Z.-C., Milyukov, V., Ming, M., Pi, X., Qin, C., Qu, S.-B., Sesana, A., Shao, C., Shi, C., Su, W., Tan, D.-Y., Tan, Y., Tan, Z., Tu, L.-C., Wang, B., Wang, C.-R., Wang, F., Wang, G.-F., Wang, H., Wang, J., Wang, L., Wang, P., Wang, X., Wang, Y., Wang, Y.-F., Wei, R., Wu, S.-C., Xiao, C.-Y., Xu, X.-S., Xue, C., Yang, F.-C., Yang, L., Yang, M.-L., Yang, S.-Q., Ye, B., Yeh, H.-C., Yu, S., Zhai, D., Zhang, C., Zhang, H., Zhang, J.-d., Zhang, J., Zhang, L., Zhang, X., Zhang, X., Zhou, H., Zhou, M.-Y., Zhou, Z.-B., Zhu, D.-D., Zi, T.-G., Luo, J.: The TianQin project: Current progress on science and technology. *Progress of Theoretical and Experimental Physics* (2020) <https://doi.org/10.1093/ptep/ptaa114> <https://academic.oup.com/ptep/advance-article-pdf/doi/10.1093/ptep/ptaa114/34068872/ptaa114.pdf>. ptaa114
- [13] Colpi, M., Danzmann, K., Hewitson, M., Holley-Bockelmann, K., Jetzer, P., Nelemans, G., Petiteau, A., Shoemaker, D., Sopuerta, C., Stebbins, R., Tanvir, N., Ward, H., Weber, W.J., Thorpe, I., Dauriskikh, A., Deep, A., Fernández Núñez, I., García Marirrodiga, C., Gehler, M., Halain, J.-P., Jennrich, O., Lamers, U., Larrañaga, J., Lieser, M., Lützgendorf, N., Martens, W., Mondin, L., Piris Niño, A., Amaro-Seoane, P., Arca Sedda, M., Auclair, P., Babak, S., Baghi, Q., Baibhav, V., Baker, T., Bayle, J.-B., Berry, C., Berti, E., Boileau, G.,

- Bonetti, M., Brito, R., Buscicchio, R., Calcagni, G., Capelo, P.R., Caprini, C., Caputo, A., Castelli, E., Chen, H.-Y., Chen, X., Chua, A., Davies, G., Derdzinski, A., Domcke, V.F., Doneva, D., Dvorkin, I., María Ezquiaga, J., Gair, J., Haiman, Z., Harry, I., Hartwig, O., Hees, A., Heffernan, A., Husa, S., Izquierdo-Villalba, D., Karnesis, N., Klein, A., Korol, V., Korsakova, N., Kupfer, T., Laghi, D., Lamberts, A., Larson, S., Le Jeune, M., Lewicki, M., Littenberg, T., Madge, E., Mangiagli, A., Marsat, S., Vilchez, I.M., Maselli, A., Mathews, J., van de Meent, M., Muratore, M., Nardini, G., Pani, P., Peloso, M., Pieroni, M., Pound, A., Quelquejay-Leclere, H., Ricciardone, A., Rossi, E.M., Sartirana, A., Savalle, E., Sberna, L., Sesana, A., Shoemaker, D., Slutsky, J., Sotiriou, T., Spери, L., Staab, M., Steer, D., Tamanini, N., Tasinato, G., Torrado, J., Torres-Orjuela, A., Toubiana, A., Vallisneri, M., Vecchio, A., Volonteri, M., Yagi, K., Zwick, L.: LISA Definition Study Report. arXiv e-prints, 2402–07571 (2024) <https://doi.org/10.48550/arXiv.2402.07571> arXiv:2402.07571 [astro-ph.CO]
- [14] Smetana, A.: Background for gravitational wave signal at LISA from refractive index of solar wind plasma. *Monthly Notices of the Royal Astronomical Society* **499**(1), 77–81 (2020) <https://doi.org/10.1093/mnras/slaa155> arXiv:2008.11105 [astro-ph.IM]
- [15] Lu, L.-F., Su, W., Zhang, X., He, Z.-G., Duan, H.-Z., Jiang, Y.-Z., Yeh, H.-C.: Effects of the Space Plasma Density Oscillation on the Interspacecraft Laser Ranging for TianQin Gravitational Wave Observatory. *Journal of Geophysical Research (Space Physics)* **126**(2), 28579 (2021) <https://doi.org/10.1029/2020JA028579> arXiv:2103.08326 [physics.space-ph]
- [16] Su, W., Wang, Y., Zhou, C., Lu, L., Zhou, Z.-B., Li, T.M., Shi, T., Hu, X.-C., Zhou, M.-Y., Wang, M., Yeh, H.-C., Wang, H., Chen, P.F.: Analyses of Laser Propagation Noises for TianQin Gravitational Wave Observatory Based on the Global Magnetosphere MHD Simulations. *The Astrophysical Journal* **914**(2), 139 (2021) <https://doi.org/10.3847/1538-4357/abfc49> arXiv:2102.10574 [astro-ph.SR]
- [17] Jennrich, O., Luetzgendorf, N., Thorpe, J.I., Slutsky, J., Cutler, C.: Sensitivity limits of space-based interferometric gravitational wave observatories from the solar wind. *Physical Review D* **104**(6), 062003 (2021) <https://doi.org/10.1103/PhysRevD.104.062003> arXiv:2107.03138 [astro-ph.IM]
- [18] Schumaker, B.L.: Disturbance reduction requirements for LISA. *Classical and Quantum Gravity* **20**(10), 239–253 (2003) <https://doi.org/10.1088/0264-9381/20/10/327>
- [19] Stebbins, R.T., Bender, P.L., Hanson, J., Hoyle, C.D., Schumaker, B.L., Vitale, S.: Current error determinates for LISA spurious accelerations. *Classical and Quantum Gravity* **21**(5), 653–660 (2004) <https://doi.org/10.1088/0264-9381/21/5/039>

- [20] Su, W., Wang, Y., Zhou, Z.-B., Bai, Y.-Z., Guo, Y., Zhou, C., Lee, T., Wang, M., Zhou, M.-Y., Shi, T., Yin, H., Zhang, B.-T.: Analyses of residual accelerations for TianQin based on the global MHD simulation. *Classical and Quantum Gravity* **37**(18), 185017 (2020) <https://doi.org/10.1088/1361-6382/aba181> [arXiv:2004.00254](https://arxiv.org/abs/2004.00254) [astro-ph.IM]
- [21] Hanson, J., MacKeiser, G., Buchman, S., Byer, R., Lauben, D., DeBra, D., Williams, S., Gill, D., Shelef, B., Shelef, G.: ST-7 gravitational reference sensor: analysis of magnetic noise sources. *Classical and Quantum Gravity* **20**(10), 109–116 (2003) <https://doi.org/10.1088/0264-9381/20/10/313>
- [22] Charbonneau, P.: Dynamo Models of the Solar Cycle. *Living Reviews in Solar Physics* **7**(1), 3 (2010) <https://doi.org/10.12942/lrsp-2010-3>
- [23] Zhang, J., Li, L., Song, Q.: Interaction between a Fast Rotating Sunspot and Ephemeral Regions as the Origin of the Major Solar Event on 2006 December 13. *The Astrophysical Journal Letters* **662**(1), 35–38 (2007) <https://doi.org/10.1086/519280> [arXiv:0705.0607](https://arxiv.org/abs/0705.0607) [astro-ph]
- [24] Lin, J., Murphy, N.A., Shen, C., Raymond, J.C., Reeves, K.K., Zhong, J., Wu, N., Li, Y.: Review on Current Sheets in CME Development: Theories and Observations. *Space Science Reviews* **194**(1-4), 237–302 (2015) <https://doi.org/10.1007/s11214-015-0209-0>
- [25] Li, G.: Particle acceleration and transport in the inner heliosphere. *Science China Earth Sciences* **60**(8), 1440–1465 (2017) <https://doi.org/10.1007/s11430-017-9083-y>
- [26] Guo, Y., Guo, J., Ni, Y., Xia, C., Zhong, Z., Ding, M., Chen, P., Keppens, R.: Magnetic flux rope models and data-driven magnetohydrodynamic simulations of solar eruptions. *Reviews of Modern Plasma Physics* **8**(1), 29 (2024) <https://doi.org/10.1007/s41614-024-00167-2>
- [27] Zhou, M., Berchem, J., Walker, R.J., El-Alaoui, M., Goldstein, M.L., Lapenta, G., Deng, X., Li, J., Le Contel, O., Graham, D.B., Lavraud, B., Paterson, W.R., Giles, B.L., Burch, J.L., Torbert, R.B., Russell, C.T., Strangeway, R.J., Zhao, C., Ergun, R.E., Lindqvist, P.-A., Marklund, G.: Magnetospheric Multi-scale Observations of an Ion Diffusion Region With Large Guide Field at the Magnetopause: Current System, Electron Heating, and Plasma Waves. *Journal of Geophysical Research (Space Physics)* **123**(3), 1834–1852 (2018) <https://doi.org/10.1002/2017JA024517>
- [28] Zhou, M., Deng, X.H., Zhong, Z.H., Pang, Y., Tang, R.X., El-Alaoui, M., Walker, R.J., Russell, C.T., Lapenta, G., Strangeway, R.J., Torbert, R.B., Burch, J.L., Paterson, W.R., Giles, B.L., Khotyaintsev, Y.V., Ergun, R.E., Lindqvist, P.-A.: Observations of an Electron Diffusion Region in Symmetric Reconnection with Weak Guide Field. *The Astrophysical Journal* **870**(1), 34 (2019) <https://doi.org/10.3847/1538-4357/ab1111>

- [29] Li, W.-Y., Khotyaintsev, Y.V., Tang, B.-B., Graham, D.B., Norgren, C., Vaivads, A., André, M., Le, A., Egedal, J., Dokgo, K., Fujimoto, K., He, J.-S., Burch, J.L., Lindqvist, P.-A., Ergun, R.E., Torbert, R.B., Le Contel, O., Gershman, D.J., Giles, B.L., Lavraud, B., Fuselier, S., Plaschke, F., Russell, C.T., Guo, X.-C., Lu, Q.-M., Wang, C.: Upper-Hybrid Waves Driven by Meandering Electrons Around Magnetic Reconnection X Line. *Geophysical Research Letters* **48**(16), 93164 (2021) <https://doi.org/10.1029/2021GL093164>
- [30] Zhao, J.: Properties of Whistler Waves in Warm Electron Plasmas. *The Astrophysical Journal* **850**(1), 13 (2017) <https://doi.org/10.3847/1538-4357/aa906f>
- [31] Huang, S.Y., Zhang, J., Sahraoui, F., He, J.S., Yuan, Z.G., Andrés, N., Hadid, L.Z., Deng, X.H., Jiang, K., Yu, L., Xiong, Q.Y., Wei, Y.Y., Xu, S.B., Bale, S.D., Kasper, J.C.: Kinetic Scale Slow Solar Wind Turbulence in the Inner Heliosphere: Coexistence of Kinetic Alfvén Waves and Alfvén Ion Cyclotron Waves. *The Astrophysical Journal Letters* **897**(1), 3 (2020) <https://doi.org/10.3847/2041-8213/ab9abb> [arXiv:2006.04665](https://arxiv.org/abs/2006.04665) [physics.space-ph]
- [32] Huang, S.Y., Xu, S.B., Zhang, J., Sahraoui, F., Andrés, N., He, J.S., Yuan, Z.G., Deng, X.H., Jiang, K., Wei, Y.Y., Xiong, Q.Y., Wang, Z., Yu, L., Lin, R.T.: Anisotropy of Magnetic Field Spectra at Kinetic Scales of Solar Wind Turbulence as Revealed by the Parker Solar Probe in the Inner Heliosphere. *The Astrophysical Journal Letters* **929**(1), 6 (2022) <https://doi.org/10.3847/2041-8213/ac5f02> [arXiv:2203.10475](https://arxiv.org/abs/2203.10475) [astro-ph.SR]
- [33] He, J., Tu, C., Marsch, E., Bourouaine, S., Pei, Z.: Radial Evolution of the Wavevector Anisotropy of Solar Wind Turbulence between 0.3 and 1 AU. *The Astrophysical Journal* **773**(1), 72 (2013) <https://doi.org/10.1088/0004-637X/773/1/72> [arXiv:1302.0699](https://arxiv.org/abs/1302.0699) [astro-ph.SR]
- [34] Wu, H., Tu, C., Wang, X., He, J., Yang, L., Wang, L.: Isotropic Scaling Features Measured Locally in the Solar Wind Turbulence with Stationary Background Field. *The Astrophysical Journal* **892**(2), 138 (2020) <https://doi.org/10.3847/1538-4357/ab7b72> [arXiv:2011.10244](https://arxiv.org/abs/2011.10244) [physics.space-ph]
- [35] Su, W., Li, T.M., Cheng, X., Feng, L., Zhang, P.J., Chen, P.F., Ding, M.D., Chen, L.J., Guo, Y., Wang, Y., Li, D., Zhang, L.Y.: Quantifying the Magnetic Structure of a Coronal Shock Producing a Type II Radio Burst. *The Astrophysical Journal* **929**(2), 175 (2022) <https://doi.org/10.3847/1538-4357/ac5fac> [arXiv:2203.11042](https://arxiv.org/abs/2203.11042) [astro-ph.SR]
- [36] Trotta, D., Dimmock, A., Hietala, H., Blanco-Cano, X., Horbury, T.S., Vainio, R., Dresing, N., Jebaraj, I.C., Espinosa Lara, F., Gómez-Herrero, R., Rodríguez-Pacheco, J., Kartavykh, Y., Lario, D., Gieseler, J., Janvier, M., Maksimovic, M., Talebpour Sheshvan, N., Owen, C.J., Kilpua, E.K.J., Wimmer-Schweingruber,

- R.F.: An Overview of Solar Orbiter Observations of Interplanetary Shocks in Solar Cycle 25. *The Astrophysical Journal Supplement Series* **277**(1), 2 (2025) <https://doi.org/10.3847/1538-4365/ada4a7> arXiv:2410.24007 [astro-ph.SR]
- [37] Zhang, G., Burlaga, L.F.: Magnetic clouds, geomagnetic disturbances, and cosmic ray decreases. *Journal of Geophysical Research* **93**(A4), 2511–2518 (1988) <https://doi.org/10.1029/JA093iA04p02511>
- [38] Bothmer, V., Schwenn, R.: The structure and origin of magnetic clouds in the solar wind. *Annales Geophysicae* **16**(1), 1–24 (1998) <https://doi.org/10.1007/s00585-997-0001-x>
- [39] Feng, L., Inhester, B., Gan, W.Q.: Kelvin-Helmholtz Instability of a Coronal Streamer. *The Astrophysical Journal* **774**(2), 141 (2013) <https://doi.org/10.1088/0004-637X/774/2/141> arXiv:1307.5120 [astro-ph.SR]
- [40] Parker, E.N.: Dynamics of the Interplanetary Gas and Magnetic Fields. *The Astrophysical Journal* **128**, 664 (1958) <https://doi.org/10.1086/146579>
- [41] Parker, E.N.: Interaction of the Solar Wind with the Geomagnetic Field. *Physics of Fluids* **1**, 171–187 (1958) <https://doi.org/10.1063/1.1724339>
- [42] Gosling, J.T., Pizzo, V.J.: Formation and Evolution of Corotating Interaction Regions and their Three Dimensional Structure. *Space Science Reviews* **89**, 21–52 (1999) <https://doi.org/10.1023/A:1005291711900>
- [43] Allen, R.C., Ho, G.C., Mason, G.M., Li, G., Jian, L.K., Vines, S.K., Schwadron, N.A., Joyce, C.J., Bale, S.D., Bonnell, J.W., Case, A.W., Christian, E.R., Cohen, C.M.S., Desai, M.I., Filwett, R., Goetz, K., Harvey, P.R., Hill, M.E., Kasper, J.C., Korreck, K.E., Lario, D., Larson, D., Livi, R., MacDowall, R.J., Malaspina, D.M., McComas, D.J., McNutt, R., Mitchell, D.G., Paulson, K.W., Pulupa, M., Raouafi, N., Stevens, M.L., Whittlesey, P.L., Wiedenbeck, M.: Radial Evolution of a CIR: Observations From a Nearly Radially Aligned Event Between Parker Solar Probe and STEREO A. *Geophysical Research Letters* **48**(3), 91376 (2021) <https://doi.org/10.1029/2020GL091376>
- [44] Wijsen, N., Li, G., Ding, Z., Lario, D., Poedts, S., Filwett, R.J., Allen, R.C., Dayeh, M.A.: On the Seed Population of Solar Energetic Particles in the Inner Heliosphere. *Journal of Geophysical Research (Space Physics)* **128**(3), 2022–031203 (2023) <https://doi.org/10.1029/2022JA031203> arXiv:2304.09098 [physics.space-ph]
- [45] Lin, J., Forbes, T.G.: Effects of reconnection on the coronal mass ejection process. *Journal of Geophysical Research* **105**(A2), 2375–2392 (2000) <https://doi.org/10.1029/1999JA900477>
- [46] Song, Y.L., Zhang, M.: On the Relationship Between Sunspot Structure

- and Magnetic Field Changes Associated with Solar Flares. *The Astrophysical Journal* **826**(2), 173 (2016) <https://doi.org/10.3847/0004-637X/826/2/173> [arXiv:1605.01163](https://arxiv.org/abs/1605.01163) [astro-ph.SR]
- [47] Yang, S., Zhang, J.: Mini-filament Eruptions Triggering Confined Solar Flares Observed by ONSET and SDO. *The Astrophysical Journal Letters* **860**(2), 25 (2018) <https://doi.org/10.3847/2041-8213/aacaf9> [arXiv:1806.01763](https://arxiv.org/abs/1806.01763) [astro-ph.SR]
- [48] Chen, P.F.: Coronal Mass Ejections: Models and Their Observational Basis. *Living Reviews in Solar Physics* **8**(1), 1 (2011) <https://doi.org/10.12942/lrsp-2011-1>
- [49] Cheng, X., Guo, Y., Ding, M.: Origin and Structures of Solar Eruptions I: Magnetic Flux Rope. *Science China Earth Sciences* **60**, 1383–1407 (2017) <https://doi.org/10.1007/s11430-017-9074-6> [arXiv:1705.08198](https://arxiv.org/abs/1705.08198) [astro-ph.SR]
- [50] Tsurutani, B.T., Gonzalez, W.D., Tang, F., Akasofu, S.I., Smith, E.J.: Origin of interplanetary southward magnetic fields responsible for major magnetic storms near solar maximum (1978-1979). *Journal of Geophysical Research* **93**(A8), 8519–8531 (1988) <https://doi.org/10.1029/JA093iA08p08519>
- [51] Gonzalez, W.D., Joselyn, J.A., Kamide, Y., Kroehl, H.W., Rostoker, G., Tsurutani, B.T., Vasyliunas, V.M.: What is a geomagnetic storm? *Journal of Geophysical Research* **99**(A4), 5771–5792 (1994) <https://doi.org/10.1029/93JA02867>
- [52] Nagai, T., Fujimoto, M., Saito, Y., Machida, S., Terasawa, T., Nakamura, R., Yamamoto, T., Mukai, T., Nishida, A., Kokubun, S.: Structure and dynamics of magnetic reconnection for substorm onsets with Geotail observations. *Journal of Geophysical Research* **103**(A3), 4419–4440 (1998) <https://doi.org/10.1029/97JA02190>
- [53] Bittencourt, J.A.: *Fundamentals of Plasma Physics*. Springer, ??? (2004)
- [54] Hutchinson, I.H.: *Principles of Plasma Diagnostics*, (2002)
- [55] Parker, E.N.: The passage of energetic charged particles through interplanetary space. *Planetary and Space Science* **13**(1), 9–49 (1965) [https://doi.org/10.1016/0032-0633\(65\)90131-5](https://doi.org/10.1016/0032-0633(65)90131-5)
- [56] Potgieter, M.S.: Solar Modulation of Cosmic Rays. *Living Reviews in Solar Physics* **10**(1), 3 (2013) <https://doi.org/10.12942/lrsp-2013-3> [arXiv:1306.4421](https://arxiv.org/abs/1306.4421) [physics.space-ph]
- [57] Reames, D.V.: The Two Sources of Solar Energetic Particles. *Space Science Reviews* **175**(1-4), 53–92 (2013) <https://doi.org/10.1007/s11214-013-9958-9>

[arXiv:1306.3608](#) [astro-ph.SR]

- [58] Li, C., Firoz, K.A., Sun, L.P., Miroshnichenko, L.I.: Electron and Proton Acceleration during the First Ground Level Enhancement Event of Solar Cycle 24. The Astrophysical Journal **770**(1), 34 (2013) <https://doi.org/10.1088/0004-637X/770/1/34> [arXiv:1305.5606](#) [astro-ph.SR]
- [59] Sumner, T.J., Mueller, G., Conklin, J.W., Wass, P.J., Hollington, D.: Charge induced acceleration noise in the LISA gravitational reference sensor. Classical and Quantum Gravity **37**(4), 045010 (2020) <https://doi.org/10.1088/1361-6382/ab5f6e> [arXiv:1909.12608](#) [physics.ins-det]
- [60] Qiao, D., Jia, F., Li, X., Zhou, X.: A Review of Orbital Mechanics for Space-Based Gravitational Wave Observatories. Space: Science and Technology **3**, 0015 (2023) <https://doi.org/10.34133/space.0015>
- [61] Qiao, D., Zhou, X., Li, X.: Feasible domain analysis of heliocentric gravitational-wave detection configuration using semi-analytical uncertainty propagation. Advances in Space Research **72**(10), 4115–4131 (2023) <https://doi.org/10.1016/j.asr.2023.08.011>
- [62] Ogilvie, K.W., Chornay, D.J., Fritzenreiter, R.J., Hunsaker, F., Keller, J., Lobell, J., Miller, G., Scudder, J.D., Sittler, E.C. Jr., Torbert, R.B., Bodet, D., Needell, G., Lazarus, A.J., Steinberg, J.T., Tappan, J.H., Mavretic, A., Gergin, E.: SWE, A Comprehensive Plasma Instrument for the Wind Spacecraft. Space Science Reviews **71**(1-4), 55–77 (1995) <https://doi.org/10.1007/BF00751326>
- [63] Stone, E.C., Frandsen, A.M., Mewaldt, R.A., Christian, E.R., Margolies, D., Ormes, J.F., Snow, F.: The Advanced Composition Explorer. Space Science Reviews **86**, 1–22 (1998) <https://doi.org/10.1023/A:1005082526237>
- [64] King, J.H., Papitashvili, N.E.: Solar wind spatial scales in and comparisons of hourly Wind and ACE plasma and magnetic field data. Journal of Geophysical Research (Space Physics) **110**(A2), 02104 (2005) <https://doi.org/10.1029/2004JA010649>
- [65] Zhang, X., Luo, C., Jiao, L., Ye, B., Yuan, H., Cai, L., Gu, D., Mei, J., Luo, J.: Effect of earth-moon’s gravity on tianqin’s range acceleration noise. Phys. Rev. D **103**, 062001 (2021) <https://doi.org/10.1103/PhysRevD.103.062001>
- [66] Ye, B., Zhang, X., Ding, Y., Meng, Y.: Eclipse avoidance in tianqin orbit selection. Phys. Rev. D **103**, 042007 (2021) <https://doi.org/10.1103/PhysRevD.103.042007>
- [67] Jia, F., Li, X., Qiao, D., Zhou, X.: Semi-analytical configuration optimization of geocentric gravitational wave observatory. Acta Astronautica **202**, 522–534 (2023) <https://doi.org/10.1016/j.actaastro.2022.10.048>

- [68] Liu, Z.-Q., Lu, J.Y., Wang, C., Kabin, K., Zhao, J.S., Wang, M., Han, J.P., Wang, J.Y., Zhao, M.X.: A three-dimensional high Mach number asymmetric magnetopause model from global MHD simulation. *Journal of Geophysical Research (Space Physics)* **120**(7), 5645–5666 (2015) <https://doi.org/10.1002/2014JA020961>
- [69] Lu, J.Y., Zhou, Y., Ma, X., Wang, M., Kabin, K., Yuan, H.Z.: Earth’s Bow Shock: A New Three-Dimensional Asymmetric Model With Dipole Tilt Effects. *Journal of Geophysical Research (Space Physics)* **124**(7), 5396–5407 (2019) <https://doi.org/10.1029/2018JA026144>
- [70] Lu, J.Y., Wang, M., Kabin, K., Zhao, J.S., Liu, Z.-Q., Zhao, M.X., Li, G.: Pressure balance across the magnetopause: Global MHD results. *Planetary and Space Science* **106**, 108–115 (2015) <https://doi.org/10.1016/j.pss.2014.12.003>
- [71] Wang, M., Lu, J.Y., Kabin, K., Yuan, H.Z., Liu, Z.-Q., Zhao, J.S., Li, G.: The Influence of IMF B_y on the Bow Shock: Observation Result. *Journal of Geophysical Research (Space Physics)* **123**(3), 1915–1926 (2018) <https://doi.org/10.1002/2017JA024750>
- [72] Balogh, A., Carr, C.M., Acuña, M.H., Dunlop, M.W., Beek, T.J., Brown, P., Fornaçon, K.-H., Georgescu, E., Glassmeier, K.-H., Harris, J., Musmann, G., Oddy, T., Schwingenschuh, K.: The Cluster Magnetic Field Investigation: overview of in-flight performance and initial results. *Annales Geophysicae* **19**(10), 1207–1217 (2001) <https://doi.org/10.5194/angeo-19-1207-2001>
- [73] Rème, H., Aoustin, C., Bosqued, J.M., Dandouras, I., Lavraud, B., Sauvaud, J.A., Barthe, A., Bouyssou, J., Camus, T., Coeur-Joly, O., Cros, A., Cuvilo, J., Ducay, F., Garbarowitz, Y., Medale, J.L., Penou, E., Perrier, H., Romefort, D., Rouzaud, J., Vallat, C., Alcaydé, D., Jacquey, C., Mazelle, C., D’Uston, C., Möbius, E., Kistler, L.M., Crocker, K., Granoff, M., Mouikis, C., Popecki, M., Vosbury, M., Klecker, B., Hovestadt, D., Kucharek, H., Kuenneth, E., Paschmann, G., Scholer, M., Sckopke, N., Seidenschwang, E., Carlson, C.W., Curtis, D.W., Ingraham, C., Lin, R.P., McFadden, J.P., Parks, G.K., Phan, T., Formisano, V., Amata, E., Bavassano-Cattaneo, M.B., Baldetti, P., Bruno, R., Chionchio, G., di Lellis, A., Marcucci, M.F., Pallocchia, G., Korth, A., Daly, P.W., Graeve, B., Rosenbauer, H., Vasyliunas, V., McCarthy, M., Wilber, M., Eliasson, L., Lundin, R., Olsen, S., Shelley, E.G., Fuselier, S., Ghielmetti, A.G., Lennartsson, W., Escoubet, C.P., Balsiger, H., Friedel, R., Cao, J.-B., Kovrazhkin, R.A., Papamastorakis, I., Pellat, R., Scudder, J., Sonnerup, B.: First multispacecraft ion measurements in and near the Earth’s magnetosphere with the identical Cluster ion spectrometry (CIS) experiment. *Annales Geophysicae* **19**, 1303–1354 (2001) <https://doi.org/10.5194/angeo-19-1303-2001>
- [74] Angelopoulos, V.: The THEMIS Mission. *Space Science Reviews* **141**(1-4), 5–34 (2008) <https://doi.org/10.1007/s11214-008-9336-1>

- [75] Burch, J.L., Moore, T.E., Torbert, R.B., Giles, B.L.: Magnetospheric Multiscale Overview and Science Objectives. *Space Science Reviews* **199**(1-4), 5–21 (2016) <https://doi.org/10.1007/s11214-015-0164-9>
- [76] Tsyganenko, N.A.: A lifetime with models, or toils and thrills of number crunching. *Frontiers in Astronomy and Space Sciences* **9**, 934216 (2022) <https://doi.org/10.3389/fspas.2022.934216>
- [77] Tsyganenko, N.A.: A magnetospheric magnetic field model with a warped tail current sheet. *Planetary and Space Science* **37**(1), 5–20 (1989) [https://doi.org/10.1016/0032-0633\(89\)90066-4](https://doi.org/10.1016/0032-0633(89)90066-4)
- [78] Tsyganenko, N.A.: Modeling the Earth’s magnetospheric magnetic field confined within a realistic magnetopause. *Journal of Geophysical Research* **100**(A4), 5599–5612 (1995) <https://doi.org/10.1029/94JA03193>
- [79] Tsyganenko, N.A., Stern, D.P.: Modeling the global magnetic field of the large-scale Birkeland current systems. *Journal of Geophysical Research* **101**(A12), 27187–27198 (1996) <https://doi.org/10.1029/96JA02735>
- [80] Tsyganenko, N.A.: A model of the near magnetosphere with a dawn-dusk asymmetry 1. Mathematical structure. *Journal of Geophysical Research (Space Physics)* **107**(A8), 1179 (2002) <https://doi.org/10.1029/2001JA000219>
- [81] Tsyganenko, N.A.: A model of the near magnetosphere with a dawn-dusk asymmetry 2. Parameterization and fitting to observations. *Journal of Geophysical Research (Space Physics)* **107**(A8), 1176 (2002) <https://doi.org/10.1029/2001JA000220>
- [82] Tsyganenko, N.A., Sitnov, M.I.: Modeling the dynamics of the inner magnetosphere during strong geomagnetic storms. *Journal of Geophysical Research (Space Physics)* **110**(A3), 03208 (2005) <https://doi.org/10.1029/2004JA010798>
- [83] Ganushkina, N.Y., Liemohn, M.W., Dubyagin, S.: Current Systems in the Earth’s Magnetosphere. *Reviews of Geophysics* **56**(2), 309–332 (2018) <https://doi.org/10.1002/2017RG000590>
- [84] Yue, C., Bortnik, J., Zou, S., Nishimura, Y., Foster, J.C., Coppeans, T., Ma, Q., Zong, Q., Hull, A.J., Henderson, M., Reeves, G.D., Spence, H.E.: Episodic Occurrence of Field-Aligned Energetic Ions on the Dayside. *Geophysical Research Letters* **47**(2), 86384 (2020) <https://doi.org/10.1029/2019GL086384>
- [85] Watermann, J., Wintoft, P., Sanahuja, B., Saiz, E., Poedts, S., Palmroth, M., Milillo, A., Metallinou, F.-A., Jacobs, C., Ganushkina, N.Y., Daglis, I.A., Cid, C., Cerrato, Y., Balasis, G., Aylward, A.D., Aran, A.: Models of Solar Wind Structures and Their Interaction with the Earth’s Space Environment. *Space Science Reviews* **147**(3-4), 233–270 (2009) <https://doi.org/10.1007/>

- [86] Jackman, C.M., Arridge, C.S., André, N., Bagenal, F., Birn, J., Freeman, M.P., Jia, X., Kidder, A., Milan, S.E., Radioti, A., Slavin, J.A., Vogt, M.F., Volwerk, M., Walsh, A.P.: Large-Scale Structure and Dynamics of the Magnetotails of Mercury, Earth, Jupiter and Saturn. *Space Science Reviews* **182**(1-4), 85–154 (2014) <https://doi.org/10.1007/s11214-014-0060-8>
- [87] Daglis, I.A.: Ring Current Dynamics. *Space Science Reviews* **124**(1-4), 183–202 (2006) <https://doi.org/10.1007/s11214-006-9104-z>
- [88] Tang, B.B., Li, W.Y., Wang, C., Khotyaintsev, Y.V., Graham, D.B., Zhang, Q.H., Sun, T.R., Li, H., Wang, X.Y., Trattner, K.J., Giles, B.L., Lindqvist, P.A., Ergun, R.E., Burch, J.L.: Secondary magnetic reconnection at Earth’s flank magnetopause. *Frontiers in Astronomy and Space Sciences* **8**, 179 (2021) <https://doi.org/10.3389/fspas.2021.740560>
- [89] Su, W., Zhou, Z.-B., Wang, Y., Zhou, C., Chen, P.F., Hong, W., Peng, J.H., Yang, Y., Ni, Y.W.: Evaluating residual acceleration noise for the TianQin gravitational waves observatory with an empirical magnetic field model. *Physical Review D* **108**(10), 103030 (2023) <https://doi.org/10.1103/PhysRevD.108.103030> [arXiv:2310.10043](https://arxiv.org/abs/2310.10043) [astro-ph.IM]
- [90] Stone, J.M., Tomida, K., White, C.J., Felker, K.G.: The Athena++ Adaptive Mesh Refinement Framework: Design and Magnetohydrodynamic Solvers. *The Astrophysical Journal Supplement Series* **249**(1), 4 (2020) <https://doi.org/10.3847/1538-4365/ab929b> [arXiv:2005.06651](https://arxiv.org/abs/2005.06651) [astro-ph.IM]
- [91] Keppens, R., Popescu Braileanu, B., Zhou, Y., Ruan, W., Xia, C., Guo, Y., Claes, N., Bacchini, F.: MPI-AMRVAC 3.0: Updates to an open-source simulation framework. *Astronomy & Astrophysics* **673**, 66 (2023) <https://doi.org/10.1051/0004-6361/202245359> [arXiv:2303.03026](https://arxiv.org/abs/2303.03026) [astro-ph.IM]
- [92] Arber, T.D., Bennett, K., Brady, C.S., Lawrence-Douglas, A., Ramsay, M.G., Sircombe, N.J., Gillies, P., Evans, R.G., Schmitz, H., Bell, A.R., Ridgers, C.P.: Contemporary particle-in-cell approach to laser-plasma modelling. *Plasma Physics and Controlled Fusion* **57**(11), 113001 (2015) <https://doi.org/10.1088/0741-3335/57/11/113001>
- [93] Rempel, M.: Extension of the MURaM Radiative MHD Code for Coronal Simulations. *The Astrophysical Journal* **834**(1), 10 (2017) <https://doi.org/10.3847/1538-4357/834/1/10> [arXiv:1609.09818](https://arxiv.org/abs/1609.09818) [astro-ph.SR]
- [94] Zhang, Q., Cheng, X., Liu, R., Song, A., Li, X., Wang, Y.: Influence of magnetic reconnection on the eruptive catastrophes of coronal magnetic flux ropes. *Frontiers in Astronomy and Space Sciences* **9**, 434 (2023) <https://doi.org/10.3389/fspas.2022.1084678> [arXiv:2212.14602](https://arxiv.org/abs/2212.14602) [astro-ph.SR]

- [95] Tóth, G., Sokolov, I.V., Gombosi, T.I., Chesney, D.R., Clauer, C.R., de Zeeuw, D.L., Hansen, K.C., Kane, K.J., Manchester, W.B., Oehmke, R.C., Powell, K.G., Ridley, A.J., Roussev, I.I., Stout, Q.F., Volberg, O., Wolf, R.A., Sazykin, S., Chan, A., Yu, B., Kóta, J.: Space Weather Modeling Framework: A new tool for the space science community. *Journal of Geophysical Research (Space Physics)* **110**(A12), 12226 (2005) <https://doi.org/10.1029/2005JA011126>
- [96] Welling, D.T., Ridley, A.J.: Validation of SWMF magnetic field and plasma. *Space Weather* **8**(3), 03002 (2010) <https://doi.org/10.1029/2009SW000494>
- [97] Dimmock, A.P., Nykyri, K.: The statistical mapping of magnetosheath plasma properties based on THEMIS measurements in the magnetosheath interplanetary medium reference frame. *Journal of Geophysical Research (Space Physics)* **118**(8), 4963–4976 (2013) <https://doi.org/10.1002/jgra.50465>
- [98] Takahashi, N., Seki, K., Teramoto, M., Fok, M.-C., Zheng, Y., Matsuoka, A., Higashio, N., Shiokawa, K., Baishev, D., Yoshikawa, A., Nagatsuma, T.: Global Distribution of ULF Waves During Magnetic Storms: Comparison of Arase, Ground Observations, and BATSRUS + CRCM Simulation. *Geophysical Research Letters* **45**(18), 9390–9397 (2018) <https://doi.org/10.1029/2018GL078857>
- [99] Feng, X.: *Magnetohydrodynamic Modeling of the Solar Corona and Heliosphere. Atmosphere, Earth, Ocean & Space*. Springer, Singapore (2020). <https://doi.org/10.1007/978-981-13-9081-4>
- [100] Zhou, Y.-H., Ruan, W.-Z., Xia, C., Keppens, R.: Transition region adaptive conduction (TRAC) in multidimensional magnetohydrodynamic simulations. *Astronomy & Astrophysics* **648**, 29 (2021) <https://doi.org/10.1051/0004-6361/202040254> [arXiv:2102.07549](https://arxiv.org/abs/2102.07549) [astro-ph.SR]
- [101] Jiang, C., Feng, X., Liu, R., Yan, X., Hu, Q., Moore, R.L., Duan, A., Cui, J., Zuo, P., Wang, Y., Wei, F.: A fundamental mechanism of solar eruption initiation. *Nature Astronomy* **5**, 1126–1138 (2021) <https://doi.org/10.1038/s41550-021-01414-z> [arXiv:2107.08204](https://arxiv.org/abs/2107.08204) [astro-ph.SR]
- [102] Zhou, M.-Y., Hu, X.-C., Ye, B., Hu, S., Zhu, D.-D., Zhang, X., Su, W., Wang, Y.: Orbital effects on time delay interferometry for TianQin. *Physical Review D* **103**(10), 103026 (2021) <https://doi.org/10.1103/PhysRevD.103.103026> [arXiv:2102.10291](https://arxiv.org/abs/2102.10291) [astro-ph.IM]
- [103] Lu, L., Liu, Y., Duan, H., Jiang, Y., Yeh, H.-C.: Numerical simulations of the wavefront distortion of inter-spacecraft laser beams caused by solar wind and magnetospheric plasmas. *Plasma Science and Technology* **22**(11), 115301 (2020) <https://doi.org/10.1088/2058-6272/abab69>

- [104] Hao, Q., Fang, C., Cao, W., Chen, P.F.: Statistical Analysis of Filament Features Based on the H α Solar Images from 1988 to 2013 by Computer Automated Detection Method. The Astrophysical Journal Supplement Series **221**(2), 33 (2015) <https://doi.org/10.1088/0067-0049/221/2/33> arXiv:1511.04692 [astro-ph.SR]
- [105] Jing, Y.-D., Zheng, L., Yang, S., Zhang, X., Lu, L., Tang, B., Su, W.: Plasma noise in tianqin time-delay interferometry. Phys. Rev. D **106**, 082006 (2022) <https://doi.org/10.1103/PhysRevD.106.082006>
- [106] Liu, Y., Su, W., Zhang, X., Zhang, J., Zhou, S.: Solar Plasma Noise in TianQin Laser Propagation: An Extreme Case and Statistical Analysis. The Astrophysical Journal **975**(2), 291 (2024) <https://doi.org/10.3847/1538-4357/ad7bb7> arXiv:2410.09715 [astro-ph.SR]
- [107] Perez, J.C., Bourouaine, S., Chen, C.H.K., Raouafi, N.E.: Applicability of Taylor’s hypothesis during Parker Solar Probe perihelia. Astronomy & Astrophysics **650**, 22 (2021) <https://doi.org/10.1051/0004-6361/202039879> arXiv:2103.12022 [astro-ph.SR]
- [108] Xie, F., Tang, W., Ma, X., Peng, X., Yang, Z., Qiang, L.-E., Zhang, Y., Gao, C., Zhang, J., Wang, F.: Lomb-Scargle spectral analysis of plasma’s noise for space-based laser interferometric gravitational wave antennas. Advances in Space Research **74**(8), 4196–4209 (2024) <https://doi.org/10.1016/j.asr.2024.06.069>
- [109] Tapley, B.D., Bettadpur, S., Ries, J.C., Thompson, P.F., Watkins, M.M.: GRACE Measurements of Mass Variability in the Earth System. Science **305**(5683), 503–506 (2004) <https://doi.org/10.1126/science.1099192>
- [110] Yang, Y., Li, J., Xu, J., Tang, J., Guo, H., He, H.: Contribution of the Compass satellite navigation system to global PNT users. Chinese Science Bulletin **56**(26), 2813–2819 (2011) <https://doi.org/10.1007/s11434-011-4627-4>
- [111] Petroff, E., Hessels, J.W.T., Lorimer, D.R.: Fast radio bursts. The Astronomy and Astrophysics Review **27**(1), 4 (2019) <https://doi.org/10.1007/s00159-019-0116-6> arXiv:1904.07947 [astro-ph.HE]
- [112] Landerer, F.W., Flechtner, F.M., Save, H., Webb, F.H., Bandikova, T., Bertiger, W.I., Bettadpur, S.V., Byun, S.H., Dahle, C., Dobslaw, H., Fahnstock, E., Harvey, N., Kang, Z., Kruizinga, G.L.H., Loomis, B.D., McCullough, C., Murböck, M., Nagel, P., Paik, M., Pie, N., Poole, S., Strelak, D., Tamisiea, M.E., Wang, F., Watkins, M.M., Wen, H.-Y., Wiese, D.N., Yuan, D.-N.: Extending the Global Mass Change Data Record: GRACE Follow-On Instrument and Science Data Performance. Geophysical Research Letters **47**(12), 88306 (2020) <https://doi.org/10.1029/2020GL088306>
- [113] Armstrong, J.W., Estabrook, F.B., Tinto, M.: Time-Delay Interferometry for

- Space-based Gravitational Wave Searches. *The Astrophysical Journal* **527**(2), 814–826 (1999) <https://doi.org/10.1086/308110>
- [114] Estabrook, F.B., Tinto, M., Armstrong, J.W.: Time-delay analysis of LISA gravitational wave data: Elimination of spacecraft motion effects. *Physical Review D* **62**(4), 042002 (2000) <https://doi.org/10.1103/PhysRevD.62.042002>
 - [115] Tinto, M., Armstrong, J.W.: Cancellation of laser noise in an unequal-arm interferometer detector of gravitational radiation. *Physical Review D* **59**(10), 102003 (1999) <https://doi.org/10.1103/PhysRevD.59.102003>
 - [116] Tinto, M., Dhurandhar, S.V.: Time-Delay Interferometry. *Living Reviews in Relativity* **8**(1), 4 (2005) <https://doi.org/10.12942/lrr-2005-4>
 - [117] Tinto, M., Dhurandhar, S., Malakar, D.: Second-generation time-delay interferometry. *Physical Review D* **107**(8), 082001 (2023) <https://doi.org/10.1103/PhysRevD.107.082001> [arXiv:2212.05967](https://arxiv.org/abs/2212.05967) [gr-qc]
 - [118] Tinto, M., Dhurandhar, S.V.: Time-Delay Interferometry. *Living Reviews in Relativity* **17**(1), 6 (2014) <https://doi.org/10.12942/lrr-2014-6>
 - [119] Tinto, M., Dhurandhar, S.: Higher-order time-delay interferometry. *Physical Review D* **108**(8), 082003 (2023) <https://doi.org/10.1103/PhysRevD.108.082003> [arXiv:2307.07585](https://arxiv.org/abs/2307.07585) [gr-qc]
 - [120] Hu, X.-C., Li, X.-H., Wang, Y., Feng, W.-F., Zhou, M.-Y., Hu, Y.-M., Hu, S.-C., Mei, J.-W., Shao, C.-G.: Fundamentals of the orbit and response for TianQin. *Classical and Quantum Gravity* **35**(9), 095008 (2018) <https://doi.org/10.1088/1361-6382/aab52f> [arXiv:1803.03368](https://arxiv.org/abs/1803.03368) [gr-qc]
 - [121] Zhao, X.-L., Wang, P.-P., Shao, C.-G.: The evaluation for plasma noise in arbitrary time-delay interferometry combinations. *Classical and Quantum Gravity* **41**(10), 105002 (2024) <https://doi.org/10.1088/1361-6382/ad387c>
 - [122] Diaz-Aguiló, M., García-Berro, E., Lobo, A.: Theory and modelling of the magnetic field measurement in LISA PathFinder. *Classical and Quantum Gravity* **27**(3), 035005 (2010) <https://doi.org/10.1088/0264-9381/27/3/035005> [arXiv:0908.4564](https://arxiv.org/abs/0908.4564) [gr-qc]
 - [123] Yin, H., Tan, D.-Y., Hu, M., Wang, S., Bai, Y.-Z., Wu, S.-C., Zhou, Z.-B.: Measurements of Magnetic Properties of Kilogram-Level Test Masses for Gravitational-Wave Detection Using a Torsion Pendulum. *Physical Review Applied* **15**(1), 014008 (2021) <https://doi.org/10.1103/PhysRevApplied.15.014008>
 - [124] Lou, A., Yu, Y., Zhang, B., Liu, Y., Fu, Q., Zhang, J., Fu, H.-H., Wang, S., Zhou, Z.-B.: Theoretical calculations and experimental measurements on the

- two-component Au-Pt alloys with ultralow magnetic susceptibility. *Phys. Rev. Appl.* **19**, 034080 (2023) <https://doi.org/10.1103/PhysRevApplied.19.034080>
- [125] Diaz-Aguiló, M., García-Berro, E., Lobo, A.: Inflight magnetic characterization of the test masses onboard LISA Pathfinder. *Physical Review D* **85**(4), 042004 (2012) <https://doi.org/10.1103/PhysRevD.85.042004> [arXiv:1202.2733](https://arxiv.org/abs/1202.2733) [gr-qc]
- [126] Díaz-Aguiló, M.: Magnetic diagnostics algorithms for LISA Pathfinder: System Identification and data analysis. PhD thesis, Technical University of Catalonia, Spain (January 2011)
- [127] Sun, Z., Li, P., Li, Z., Yu, T., Feng, X., Li, L., Jin, P., Wang, L.: Analysis of the calculation method and evaluation of the magnetic acceleration noise of space inertial sensor. *Results in Physics* **53**, 106955 (2023) <https://doi.org/10.1016/j.rinp.2023.106955>
- [128] Armano, M., Audley, H., Baird, J., Binetruy, P., Born, M., Bortoluzzi, D., Castelli, E., Cavalleri, A., Cesarini, A., Cruise, A.M., Danzmann, K., de Deus Silva, M., Diepholz, I., Dixon, G., Dolesi, R., Ferraioli, L., Ferroni, V., Fitzsimons, E.D., Freschi, M., Gesa, L., Gibert, F., Giardini, D., Giusteri, R., Grimaldi, C., Grzymisch, J., Harrison, I., Hartig, M.-S., Heinzl, G., Hewitson, M., Hollington, D., Hoyland, D., Hueller, M., Inchauspé, H., Jennrich, O., Jetzer, P., Karnesis, N., Kaune, B., Korsakova, N., Killow, C.J., Lobo, J.A., Liu, L., López-Zaragoza, J.P., Maarschalkerweerd, R., Mance, D., Martín, V., Martin-Polo, L., Martino, J., Martin-Porqueras, F., Mateos, I., McNamara, P.W., Mendes, J., Mendes, L., Meshksar, N., Nofrarias, M., Paczkowski, S., Perreux-Lloyd, M., Petiteau, A., Pivato, P., Plagnol, E., Ramos-Castro, J., Reiche, J., Rivas, F., Robertson, D.I., Roma-Dollase, D., Russano, G., Slutsky, J., Sopuerta, C.F., Sumner, T., Telloni, D., Texier, D., Thorpe, J.I., Trenkel, C., Vetrugno, D., Vitale, S., Wanner, G., Ward, H., Wass, P.J., Wealthy, D., Weber, W.J., Wissel, L., Wittchen, A., Zweifel, P.: Spacecraft and interplanetary contributions to the magnetic environment on-board LISA Pathfinder. *Monthly Notices of the Royal Astronomical Society* **494**(2), 3014–3027 (2020) <https://doi.org/10.1093/mnras/staa830> <https://academic.oup.com/mnras/article-pdf/494/2/3014/33129159/staa830.pdf>
- [129] Antonucci, F., Armano, M., Audley, H., Auger, G., Benedetti, M., Binetruy, P., Bogenstahl, J., Bortoluzzi, D., Bosetti, P., Brandt, N., Caleno, M., Cañizares, P., Cavalleri, A., Cesa, M., Chmeissani, M., Conchillo, A., Congedo, G., Cristofolini, I., Cruise, M., Danzmann, K., De Marchi, F., Diaz-Aguilo, M., Diepholz, I., Dixon, G., Dolesi, R., Dunbar, N., Fauste, J., Ferraioli, L., Ferrone, V., Fichter, W., Fitzsimons, E., Freschi, M., García Marin, A., García Marirrodiga, C., Gerndt, R., Gesa, L., Gilbert, F., Giardini, D., Grimaldi, C., Grynagier, A., Guillaume, B., Guzmán, F., Harrison, I., Heinzl, G., Hernández, V., Hewitson, M., Hollington, D., Hough, J., Hoyland, D., Hueller, M., Huesler, J., Jennrich, O., Jetzer, P., Johlander, B., Karnesis, N., Killow, C., Llamas, X., Lloro, I., Lobo, A.,

- Maarschalkerweerd, R., Madden, S., Mance, D., Mateos, I., McNamara, P.W., Mendes, J., Mitchell, E., Monsky, A., Nicolini, D., Nicolodi, D., Nofrarias, M., Pedersen, F., Perreur-Lloyd, M., Plagnol, E., Prat, P., Racca, G.D., Ramos-Castro, J., Reiche, J., Romera Perez, J.A., Robertson, D., Rozemeijer, H., Sanjuan, J., Schleicher, A., Schulte, M., Shaul, D., Stagnaro, L., Strandmoe, S., Steier, F., Sumner, T.J., Taylor, A., Texier, D., Trenkel, C., Tu, H.-B., Vitale, S., Wanner, G., Ward, H., Waschke, S., Wass, P., Weber, W.J., Ziegler, T., Zweifel, P.: The LISA Pathfinder mission. *Classical and Quantum Gravity* **29**(12), 124014 (2012) <https://doi.org/10.1088/0264-9381/29/12/124014>
- [130] Armano, M., Audley, H., Baird, J., Binetruy, P., Born, M., Bortoluzzi, D., Castelli, E., Cavalleri, A., Cesarini, A., Cruise, A.M., Danzmann, K., de Deus Silva, M., Diepholz, I., Dixon, G., Dolesi, R., Ferraioli, L., Ferroni, V., Fitzsimons, E.D., Freschi, M., Gesa, L., Giardini, D., Gibert, F., Giusteri, R., Grimaldi, C., Grzymisch, J., Harrison, I., Hartig, M.-S., Heinzl, G., Hewitson, M., Hollington, D., Hoyland, D., Hueller, M., Inchauspé, H., Jennrich, O., Jetzer, P., Karnesis, N., Kaune, B., Korsakova, N., Killow, C.J., Liu, L., Lobo, J.A., López-Zaragoza, J.P., Maarschalkerweerd, R., Mance, D., Martín, V., Martin-Polo, L., Martin-Porqueras, F., Martino, J., McNamara, P.W., Mendes, J., Mendes, L., Meshksar, N., Nofrarias, M., Paczkowski, S., Perreur-Lloyd, M., Petiteau, A., Pivato, P., Plagnol, E., Ramos-Castro, J., Reiche, J., Rivas, F., Robertson, D.I., Russano, G., Sala, L., Serrano, D., Slutsky, J., Sopuerta, C.F., Sumner, T., Texier, D., Thorpe, J.I., Vetrugno, D., Vitale, S., Wanner, G., Ward, H., Wass, P.J., Weber, W.J., Wissel, L., Wittchen, A., Zweifel, P.: Magnetic-Induced Force Noise in LISA Pathfinder Free-Falling Test Masses. *Physical Review Letters* **134**(7), 071401 (2025) <https://doi.org/10.1103/PhysRevLett.134.071401> [arXiv:2407.04427](https://arxiv.org/abs/2407.04427) [astro-ph.IM]
- [131] Armano, M., Audley, H., Baird, J., Binetruy, P., Born, M., Bortoluzzi, D., Castelli, E., Cavalleri, A., Cesarini, A., Cruise, A.M., Danzmann, K., de Deus Silva, M., Diepholz, I., Dixon, G., Dolesi, R., Ferraioli, L., Ferroni, V., Fitzsimons, E.D., Freschi, M., Gesa, L., Giardini, D., Gibert, F., Giusteri, R., Grimaldi, C., Grzymisch, J., Harrison, I., Hartig, M.-S., Heinzl, G., Hewitson, M., Hollington, D., Hoyland, D., Hueller, M., Inchauspé, H., Jennrich, O., Jetzer, P., Karnesis, N., Kaune, B., Korsakova, N., Killow, C.J., Liu, L., Lobo, J.A., López-Zaragoza, J.P., Maarschalkerweerd, R., Mance, D., Martín, V., Martino, J., Martin-Polo, L., Martin-Porqueras, F., Meshksar, N., McNamara, P.W., Mendes, J., Mendes, L., Nofrarias, M., Paczkowski, S., Perreur-Lloyd, M., Petiteau, A., Pivato, P., Plagnol, E., Ramos-Castro, J., Reiche, J., Robertson, D.I., Rivas, F., Russano, G., Sala, L., Serrano, D., Slutsky, J., Sopuerta, C.F., Sumner, T., Texier, D., Thorpe, J.I., Vetrugno, D., Vitale, S., Wanner, G., Ward, H., Wass, P.J., Weber, W.J., Wissel, L., Wittchen, A., Zweifel, P.: Precision measurements of the magnetic parameters of LISA Pathfinder test masses. *Physical Review D* **111**(4), 042007 (2025) <https://doi.org/10.1103/PhysRevD.111.042007> [arXiv:2407.04431](https://arxiv.org/abs/2407.04431) [astro-ph.IM]

- [132] Qiao, M.-N., Liu, L.-H., Cai, B.-S., Zhang, Y.-T., Wang, Q.-L., Xu, J.-H., Liu, Q.: Measurement of remanent magnetic moment using a torsion pendulum with single frequency modulation method. *Chinese Physics B* **32**(5), 050702 (2023) <https://doi.org/10.1088/1674-1056/acae73>
- [133] Xu, J.-H., Liu, Q., Zhu, L.: Measuring the remanent magnetic moment of a kilogram-level test mass for TianQin. *Physical Review D* **110**(6), 062001 (2024) <https://doi.org/10.1103/PhysRevD.110.062001>
- [134] Ma, J.-T., Xiao, Y.-L., Zhang, B., Wang, S., Zhou, Z.-B., Fu, H.-H.: Ultralow magnetic susceptibility in pure and Fe(Bi)-doped Au-Pt alloys improved by structural strain regulation. *Journal of Physics Condensed Matter* **37**(4), 045801 (2025) <https://doi.org/10.1088/1361-648X/ad8ab8>
- [135] Yan, Y., Luo, D., Wu, W., Yu, Y., Huo, Y., Chen, Q., Lu, J., Song, W., Xiong, Z., Fu, Q., Liu, Y., Lu, Y., Hu, R., Zhang, B., Wang, S.: Effects of cold plastic deformation on microstructure and magnetic susceptibility of au-pt alloys. *Journal of Alloys and Compounds* **1007**, 176442 (2024) <https://doi.org/10.1016/j.jallcom.2024.176442>
- [136] Yu, Y., Lin, S., Yan, Y., Huo, Y., Zhang, B., Pan, D., Wang, S., Zhou, Z.-B.: Measuring remanent magnetic moment of test masses by a compound pendulum in a magnetic shielding room. *Review of Scientific Instruments* **96**(2), 024501 (2025) <https://doi.org/10.1063/5.0248904>
- [137] Cavalleri, A., Ciani, G., Dolesi, R., Heptonstall, A., Hueller, M., Nicolodi, D., Rowan, S., Tombolato, D., Vitale, S., Wass, P.J., Weber, W.J.: A new torsion pendulum for testing the limits of free-fall for LISA test masses. *Classical and Quantum Gravity* **26**(9), 094017 (2009) <https://doi.org/10.1088/0264-9381/26/9/094017>
- [138] Su, W., Cheng, X., Ding, M.D., Chen, P.F., Ning, Z.J., Ji, H.S.: Investigating the Conditions of the Formation of a Type II Radio Burst on 2014 January 8. *The Astrophysical Journal* **830**(2), 70 (2016) <https://doi.org/10.3847/0004-637X/830/2/70> [arXiv:1609.05633](https://arxiv.org/abs/1609.05633) [astro-ph.SR]
- [139] Armano, M., Audley, H., Baird, J., Bassan, M., Benella, S., Binetruy, P., Born, M., Bortoluzzi, D., Cavalleri, A., Cesarini, A., Cruise, A.M., Danzmann, K., de Deus Silva, M., Diepholz, I., Dixon, G., Dolesi, R., Fabi, M., Ferraioli, L., Ferroni, V., Finetti, N., Fitzsimons, E.D., Freschi, M., Gesa, L., Gibert, F., Giardini, D., Giusteri, R., Grimaldi, C., Grzymisch, J., Harrison, I., Heinzl, G., Hewitson, M., Hollington, D., Hoyland, D., Hueller, M., Inchauspé, H., Jennrich, O., Jetzer, P., Karnesis, N., Kaune, B., Korsakova, N., Killow, C.J., Laurenza, M., Lobo, J.A., Lloro, I., Liu, L., López-Zaragoza, J.P., Maarschalkerweerd, R., Mance, D., Martín, V., Martin-Polo, L., Martino, J., Martin-Porqueras, F., Mateos, I., McNamara, P.W., Mendes, J., Mendes, L., Nofrarias, M., Paczkowski, S., Perreux-Lloyd, M., Petiteau, A., Pivato, P., Plagnol, E., Ramos-Castro, J.,

- Reiche, J., Robertson, D.I., Rivas, F., Russano, G., Sabbatini, F., Slutsky, J., Sopuerta, C.F., Sumner, T., Telloni, D., Texier, D., Thorpe, J.I., Vetrugno, D., Vitale, S., Wanner, G., Ward, H., Wass, P., Weber, W.J., Wissel, L., Wittchen, A., Zambotti, A., Zenoni, C., Zweifel, P.: Characteristics and Energy Dependence of Recurrent Galactic Cosmic-Ray Flux Depressions and of a Forbush Decrease with LISA Pathfinder. *The Astrophysical Journal* **854**(2), 113 (2018) <https://doi.org/10.3847/1538-4357/aaa774> [arXiv:1802.09374](https://arxiv.org/abs/1802.09374) [physics.space-ph]
- [140] Armano, M., Audley, H., Baird, J., Binetruy, P., Born, M., Bortoluzzi, D., Castelli, E., Cavalleri, A., Cesarini, A., Cruise, A.M., Danzmann, K., de Deus Silva, M., Diepholz, I., Dixon, G., Dolesi, R., Ferraioli, L., Ferroni, V., Finetti, N., Fitzsimons, E.D., Freschi, M., Gesa, L., Gibert, F., Giardini, D., Giusteri, R., Grimani, C., Grzymisch, J., Harrison, I., Heinzl, G., Hewitson, M., Hollington, D., Hoyland, D., Hueller, M., Inchauspé, H., Jennrich, O., Jetzer, P., Karnesis, N., Kaune, B., Korsakova, N., Killow, C.J., Lobo, J.A., Lloro, I., Liu, L., Lopez-Zaragoza, J.P., Maarschalkerweerd, R., Mance, D., Meshksar, N., Martín, V., Martin-Polo, L., Martino, J., Martin-Porqueras, F., Mateos, I., McNamara, P.W., Mendes, J., Mendes, L., Nofrarias, M., Paczkowski, S., Perreur-Lloyd, M., Petiteau, A., Pivato, P., Plagnol, E., Ramos-Castro, J., Reiche, J., Robertson, D.I., Rivas, F., Russano, G., Slutsky, J., Sopuerta, C.F., Sumner, T., Texier, D., Thorpe, J.I., Vetrugno, D., Vitale, S., Wanner, G., Ward, H., Wass, P., Weber, W.J., Wissel, L., Wittchen, A., Zweifel, P.: Measuring the Galactic Cosmic Ray flux with the LISA Pathfinder radiation monitor. *Astroparticle Physics* **98**, 28–37 (2018) <https://doi.org/10.1016/j.astropartphys.2018.01.006> [arXiv:1711.07427](https://arxiv.org/abs/1711.07427) [astro-ph.IM]
- [141] Armano, M., Audley, H., Baird, J., Benella, S., Binetruy, P., Born, M., Bortoluzzi, D., Castelli, E., Cavalleri, A., Cesarini, A., Cruise, A.M., Danzmann, K., de Deus Silva, M., Diepholz, I., Dixon, G., Dolesi, R., Fabi, M., Ferraioli, L., Ferroni, V., Finetti, N., Fitzsimons, E.D., Freschi, M., Gesa, L., Gibert, F., Giardini, D., Giusteri, R., Grimani, C., Grzymisch, J., Harrison, I., Heinzl, G., Hewitson, M., Hollington, D., Hoyland, D., Hueller, M., Inchauspé, H., Jennrich, O., Jetzer, P., Karnesis, N., Kaune, B., Korsakova, N., Killow, C.J., Kudela, K., Laurenza, M., Lobo, J.A., Lloro, I., Liu, L., López-Zaragoza, J.P., Maarschalkerweerd, R., Mance, D., Meshksar, N., Martín, V., Martin-Polo, L., Martino, J., Martin-Porqueras, F., Mateos, I., McNamara, P.W., Mendes, J., Mendes, L., Nofrarias, M., Paczkowski, S., Perreur-Lloyd, M., Petiteau, A., Pivato, P., Plagnol, E., Ramos-Castro, J., Reiche, J., Robertson, D.I., Rivas, F., Russano, G., Slutsky, J., Sopuerta, C.F., Sumner, T., Telloni, D., Texier, D., Thorpe, J.I., Vetrugno, D., Villani, M., Vitale, S., Wanner, G., Ward, H., Wass, P., Weber, W.J., Wissel, L., Wittchen, A., Zweifel, P.: Forbush Decreases and ~ 2 Day GCR Flux Non-recurrent Variations Studied with LISA Pathfinder. *The Astrophysical Journal* **874**(2), 167 (2019) <https://doi.org/10.3847/1538-4357/ab0c99> [arXiv:1904.04694](https://arxiv.org/abs/1904.04694) [physics.space-ph]
- [142] Cesarini, A., Grimani, C., Benella, S., Fabi, M., Sabbatini, F., Villani, M.,

- Telloni, D.: Interplanetarymedium monitoring with LISA: Lessons from LISA Pathfinder. *Journal of Space Weather and Space Climate* **12**, 36 (2022) <https://doi.org/10.1051/swsc/2022031> arXiv:2209.12329 [astro-ph.IM]
- [143] Villani, M., Sabbatini, F., Cesarini, A., Fabi, M., Grimaldi, C.: Simulations and machine learning models for cosmic-ray short-term variations and test-mass charging on board LISA. *Experimental Astronomy* **58**(3), 15 (2024) <https://doi.org/10.1007/s10686-024-09962-8>
 - [144] Heber, B., Potgieter, M.S.: Cosmic Rays at High Heliolatitudes. *Space Science Reviews* **127**(1-4), 117–194 (2006) <https://doi.org/10.1007/s11214-006-9085-y>
 - [145] Chu, W., Qin, G.: The geomagnetic cutoff rigidities at high latitudes for different solar wind and geomagnetic conditions. *Annales Geophysicae* **34**(1), 45–53 (2016) <https://doi.org/10.5194/angeo-34-45-2016>
 - [146] Shen, Z., Yang, H., Zuo, P., Qin, G., Wei, F., Xu, X., Xie, Y.: Solar Modulation of Galactic Cosmic-Ray Protons Based on a Modified Force-field Approach. *The Astrophysical Journal* **921**(2), 109 (2021) <https://doi.org/10.3847/1538-4357/ac1fe8>
 - [147] Armano, M., Audley, H., Auger, G., Baird, J.T., Binetruy, P., Born, M., Bortoluzzi, D., Brandt, N., Bursi, A., Caleno, M., Cavalleri, A., Cesarini, A., Cruise, M., Danzmann, K., de Deus Silva, M., Diepholz, I., Dolesi, R., Dunbar, N., Ferraioli, L., Ferroni, V., Fitzsimons, E.D., Flatscher, R., Freschi, M., Gallejos, J., García Marirrodiga, C., Gerndt, R., Gesa, L., Gibert, F., Giardini, D., Giusteri, R., Grimaldi, C., Grzymisch, J., Harrison, I., Heinzl, G., Hewitson, M., Hollington, D., Hueller, M., Huesler, J., Inchauspé, H., Jennrich, O., Jetzer, P., Johlander, B., Karnesis, N., Kaune, B., Killow, C.J., Korsakova, N., Lloro, I., Liu, L., López-Zaragoza, J.P., Maarschalkerweerd, R., Madden, S., Mance, D., Martín, V., Martin-Polo, L., Martino, J., Martin-Porqueras, F., Mateos, I., McNamara, P.W., Mendes, J., Mendes, L., Moroni, A., Nofrarias, M., Paczkowski, S., Perreux-Lloyd, M., Petiteau, A., Pivato, P., Plagnol, E., Prat, P., Ragnit, U., Ramos-Castro, J., Reiche, J., Romera Perez, J.A., Robertson, D.I., Rozemeijer, H., Rivas, F., Russano, G., Sarra, P., Schleicher, A., Slutsky, J., Sopuerta, C., Sumner, T.J., Texier, D., Thorpe, J.I., Trenkel, C., Vetrugno, D., Vitale, S., Wanner, G., Ward, H., Wass, P.J., Wealthy, D., Weber, W.J., Wittchen, A., Zannoni, C., Ziegler, T., Zweifel, P., LISA Pathfinder Collaboration: Charge-Induced Force Noise on Free-Falling Test Masses: Results from LISA Pathfinder. *Physical Review Letters* **118**(17), 171101 (2017) <https://doi.org/10.1103/PhysRevLett.118.171101> arXiv:1702.04633 [astro-ph.IM]
 - [148] Armano, M., Audley, H., Baird, J., Binetruy, P., Born, M., Bortoluzzi, D., Castelli, E., Cavalleri, A., Cesarini, A., Cruise, A.M., Danzmann, K., de Deus Silva, M., Diepholz, I., Dixon, G., Dolesi, R., Ferraioli, L., Ferroni, V., Fitzsimons, E.D., Freschi, M., Gesa, L., Giardini, D., Gibert, F., Giusteri, R., Grimaldi,

- C., Grzymisch, J., Harrison, I., Heinzl, G., Hewitson, M., Hollington, D., Hoyland, D., Hueller, M., Inchauspé, H., Jennrich, O., Jetzer, P., Karnesis, N., Kaune, B., Korsakova, N., Killow, C.J., Liu, L., Lloro, I., Lobo, J.A., López-Zaragoza, J.P., Maarschalkerweerd, R., Mailland, F., Mance, D., Martín, V., Martin-Polo, L., Martin-Porqueras, F., Martino, J., Mateos, I., McNamara, P.W., Mendes, J., Mendes, L., Meshskar, N., Nofrarias, M., Paczkowski, S., Perreur-Lloyd, M., Petiteau, A., Pfeil, M., Pivato, P., Plagnol, E., Ramos-Castro, J., Reiche, J., Robertson, D.I., Rivas, F., Russano, G., Santoruvo, G., Sarra, P., Shaul, D., Slutsky, J., Sopuerta, C.F., Sumner, T., Texier, D., Thorpe, J.I., Trenkel, C., Vetrugno, D., Vitale, S., Wanner, G., Ward, H., Waschke, S., Wass, P.J., Weber, W.J., Wissel, L., Wittchen, A., Zweifel, P., LISA Pathfinder Collaboration: Precision charge control for isolated free-falling test masses: LISA pathfinder results. *Physical Review D* **98**(6), 062001 (2018) <https://doi.org/10.1103/PhysRevD.98.062001> [arXiv:1807.02435](https://arxiv.org/abs/1807.02435) [physics.ins-det]
- [149] Han, R., Cai, M., Yang, T., Xu, L., Xia, Q., Jia, X., Gao, D., Li, M., Zhang, L., Li, H., Han, J.: Study on Test-Mass Charging for Taiji Gravitational Wave Observatory. *Space Weather* **22**(1), 2023–003724 (2024) <https://doi.org/10.1029/2023SW003724>
- [150] Lei, C., Su, W., Hong, W., Li, H., Zhao, M., Chen, B., Chu, L., Li, Q., Bai, Y., Zhou, Z.: Simulation for the test mass charging rate in the Tianqin orbit. *Classical and Quantum Gravity* **41**(2), 025001 (2024) <https://doi.org/10.1088/1361-6382/ad105a>
- [151] Li, G., Jin, M., Ding, Z., Bruno, A., de Nolfo, G.A., Randol, B.M., Mays, L., Ryan, J., Lario, D.: Modeling the 2012 May 17 Solar Energetic Particle Event Using the AWSoM and iPATH Models. *The Astrophysical Journal* **919**(2), 146 (2021) <https://doi.org/10.3847/1538-4357/ac0db9>
- [152] Ding, Z., Wijsen, N., Li, G., Poedts, S.: Modeling the 2020 November 29 solar energetic particle event using EUHFORIA and iPATH models. *Astronomy & Astrophysics* **668**, 71 (2022) <https://doi.org/10.1051/0004-6361/202244732> [arXiv:2210.16967](https://arxiv.org/abs/2210.16967) [physics.space-ph]
- [153] Wang, Y., Qin, G.: The Crucial Role of Perpendicular Diffusion in the Longitude Distribution of ~ 10 MeV Solar Energetic Protons. *The Astrophysical Journal* **954**(1), 81 (2023) <https://doi.org/10.3847/1538-4357/ace35b>
- [154] Han, R., Cai, M., Yang, T., Xu, L., Xia, Q., Jia, X., Gao, D., Han, J.: Effect of solar proton events on test mass for gravitational wave detection in the 24th solar cycle. *Scientific Reports* **13**, 9932 (2023) <https://doi.org/10.1038/s41598-023-37005-3>
- [155] Apple, S.M., Kenyon, S.P., Barke, S., Clark, M.R., Davila, A.Y., Letson, B.C., Mueller, G., Olatunde, T.J., Sanjuan, J., Sauter, O.E., Siu, J., Sumner, T.J., Wass, P.J., Conklin, J.W.: Measurement of stray electric fields in a capacitive

- inertial sensor using contactless test-mass charge modulation. *Physical Review D* **106**(10), 101101 (2022) <https://doi.org/10.1103/PhysRevD.106.L101101>
- [156] Buchman, S., Al Saud, T.S.M., Alfauwaz, A., Byer, R.I., Klupar, P., Lipa, J., Lui, C.Y., Saraf, S., Wang, S., Worden, P.: Flight and ground demonstration of reproducibility and stability of photoelectric properties for passive charge management using LEDs. *Classical and Quantum Gravity* **40**(2), 025010 (2023) <https://doi.org/10.1088/1361-6382/aca8e8> arXiv:2208.13090 [physics.space-ph]
 - [157] Gu, W., Cheng, K., Hong, W., Zhang, J., Song, W., Mo, C., Huang, J., Song, W.: Test mass charge estimation for the space inertial sensor with extended Kalman filter. *Measurement Science and Technology* **35**(5), 055020 (2024) <https://doi.org/10.1088/1361-6501/ad28ae>
 - [158] Li, H., Wang, C., Kan, J.R.: Midday magnetopause shifts earthward of geosynchronous orbit during geomagnetic superstorms with $Dst \leq -300$ nT. *Journal of Geophysical Research (Space Physics)* **115**(A8), 08230 (2010) <https://doi.org/10.1029/2009JA014612>
 - [159] Peng, J.-H., Zhang, J.-X., Hong, W., Su, W., Ni, Y., Guo, J., Zheng, R.: Acceleration noise due to space magnetic field for heliocentric gravitational wave detector. *Scientific Reports* **15**(1), 23287 (2025) <https://doi.org/10.1038/s41598-025-04287-8> arXiv:2502.10142 [physics.space-ph]
 - [160] Liu, Y.: Disturbance modeling and analysis for the TianQin inertial sensor. PhD thesis, Huazhong University of Science and Technology, China (January 2024)
 - [161] Jelínek, K., Němeček, Z., Šafránková, J.: A new approach to magnetopause and bow shock modeling based on automated region identification. *Journal of Geophysical Research (Space Physics)* **117**(A5), 05208 (2012) <https://doi.org/10.1029/2011JA017252>
 - [162] Romashets, E.P., Vandas, M.: Analytic Modeling of Magnetic Field in the Magnetosheath and Outer Magnetosphere. *Journal of Geophysical Research (Space Physics)* **124**(4), 2697–2710 (2019) <https://doi.org/10.1029/2018JA026006>
 - [163] Low, K.H., Wen, Q., Wang, Z.: Magnetic field dynamics and noise analysis for space-based GW detector in far-earth orbits: A hybrid modeling approach. *Acta Astronautica* **224**, 99–111 (2024) <https://doi.org/10.1016/j.actaastro.2024.08.003>
 - [164] Sánchez, R., Newman, D.: A Primer on Complex Systems vol. 943, (2018). <https://doi.org/10.1007/978-94-024-1229-1>
 - [165] Wu, H., Tu, C., He, J., Wang, X., Yang, L.: Energy transfer of the solar wind turbulence based on Parker solar probe and other spacecraft observations. *Physics of Plasmas* **30**(2), 020501 (2023) <https://doi.org/10.1063/5.0121140>

- [166] Tinto, M., Dhurandhar, S.V.: Time-delay interferometry. *Living Reviews in Relativity* **24**(1), 1 (2021) <https://doi.org/10.1007/s41114-020-00029-6> [arXiv:gr-qc/0409034](#) [gr-qc]
- [167] Toffoletto, F., Sazykin, S., Spiro, R., Wolf, R.: Inner magnetospheric modeling with the Rice Convection Model. *Space Science Reviews* **107**(1), 175–196 (2003) <https://doi.org/10.1023/A:1025532008047>